

DISS. ETH NO. 15075

**UPPER MANTLE S-VELOCITIES AND CRUSTAL  
THICKNESS IN THE EURASIA-AFRICA PLATE  
BOUNDARY REGION DERIVED FROM REGIONAL  
SEISMOGRAMS**

A dissertation submitted to the  
**SWISS FEDERAL INSTITUTE OF TECHNOLOGY ZURICH**

for the degree of  
**Doctor of Natural Sciences**

presented by  
**Federica Marone**

Dipl. Natw. ETH  
born April 30, 1975  
citizen of Bellinzona (TI)

accepted on the recommendation of

Prof. Dr. Domenico Giardini, examiner  
Dr. Suzan van der Lee, co-examiner  
PD. Dr. Wolfgang Friederich, co-examiner

2003



# Contents

---

<b>Abstract</b>	<b>v</b>
<b>Zusammenfassung</b>	<b>ix</b>
<b>1 Introduction</b>	<b>1</b>
<b>2 MIDSEA Project</b>	<b>5</b>
2.1 Station instrumentation and installation . . . . .	6
2.2 Data processing and quality . . . . .	10
2.3 Improved data coverage for crust and upper mantle studies . . . . .	12
<b>3 Joint inversion of local, regional and teleseismic data for crustal thickness in the Eurasia-Africa plate boundary region</b>	<b>15</b>
3.1 Summary . . . . .	15
3.2 Introduction . . . . .	16
3.2.1 Tectonic background . . . . .	17
3.2.2 Previous studies . . . . .	18
3.3 Data . . . . .	19
3.3.1 Constraints on crustal thickness . . . . .	19
3.3.2 Surface waves . . . . .	20
3.4 Method . . . . .	22
3.5 Uncertainties estimation . . . . .	23
3.6 Results and discussion . . . . .	30
3.6.1 Mediterranean Sea . . . . .	30
3.6.2 Eastern Atlantic Ocean . . . . .	32
3.6.3 Northern Africa . . . . .	33

3.6.4	European continent . . . . .	34
3.7	Isostatic compensation . . . . .	35
3.8	Conclusions . . . . .	38
<b>4</b>	<b>3D upper mantle <i>S</i>-velocity model for the Eurasia-Africa plate boundary region</b>	<b>39</b>
4.1	Summary . . . . .	39
4.2	Introduction . . . . .	40
4.2.1	Tectonic background . . . . .	41
4.2.2	Previous studies . . . . .	42
4.3	Method . . . . .	43
4.3.1	Waveform modeling . . . . .	44
4.3.2	Point constraints on crustal thickness . . . . .	45
4.3.3	3D inversion . . . . .	45
4.4	Data . . . . .	47
4.5	Resolution . . . . .	52
4.5.1	Choice of the final model . . . . .	57
4.6	Results . . . . .	58
4.6.1	Mediterranean Sea . . . . .	63
4.6.2	Northern Africa . . . . .	66
4.6.3	Eastern Atlantic Ocean . . . . .	66
4.6.4	Europe . . . . .	67
4.6.5	Iberian peninsula . . . . .	69
4.7	Discussion . . . . .	70
4.7.1	Spreading ridges and old basins . . . . .	70
4.7.2	Slab fragments in the western Mediterranean . . . . .	71
4.7.3	Transition zone . . . . .	72
4.8	Conclusions . . . . .	73
<b>5</b>	<b>Love and Rayleigh wave incompatibility</b>	<b>75</b>
5.1	1D path average velocity models . . . . .	75
5.1.1	Influence of methodology choices . . . . .	76
5.1.2	Influence of uncertainties in source parameters and unmodeled physical processes . . . . .	79
5.1.3	Anisotropy . . . . .	80
5.2	3D upper mantle velocity models . . . . .	80
5.3	Significant modes . . . . .	83
5.4	Significant linear constraints . . . . .	85
5.5	Surface wave refraction at sharp vertical boundaries . . . . .	88
5.5.1	Path deviations . . . . .	90
5.5.2	Phase velocities . . . . .	93

---

5.6	Conclusions and outlook . . . . .	95
<b>6</b>	<b>Conclusions</b>	<b>97</b>
<b>Appendices</b>		
<b>A</b>	<b>Point constraints references</b>	<b>101</b>
A.1	Receiver function studies . . . . .	101
A.2	Gravity studies . . . . .	102
A.3	Reflection and refraction seismic studies . . . . .	102
<b>B</b>	<b>Additional resolution tests</b>	<b>107</b>
	<b>Bibliography</b>	<b>113</b>
	<b>Curriculum Vitae</b>	<b>125</b>



# Abstract

---

The Mediterranean region is characterized by the tectonic plate boundary between the Eurasian and African plates, extending from the Azores triple junction to Turkey and the easternmost Mediterranean Sea. This plate boundary region shows unique characteristics compared to other suture zones around the world. In particular, due to the presence of several semi-independent microcontinents between the two major plates, to the irregular shape of the converging landmasses and to different converging patterns (velocity and direction) through time, the resulting tectonics and geodynamics dominating this region are highly complicated and strong lateral variations in the past and present ongoing processes are observed.

We used new seismic data to map the Moho discontinuity and to image the smooth *S*-velocity structure of the upper mantle of the Africa-Eurasia suture zone with a resolution complementary to existing studies. The used data have been recorded at 25 broad band seismic stations (MIDSEA project) temporarily deployed along the plate boundary region and at permanent seismic station networks. Following the Partitioned Waveform Inversion method, we interactively fitted the waveforms of *S*- and Rayleigh wave trains of more than 1100 seismograms. The linear constraints on upper mantle *S*-velocity and Moho depth provided by the waveform fits have been combined with independent estimates of Moho depth taken from published reflection and refraction surveys, gravity studies and receiver function analysis in a linear damped least-squares inversion for *S*-velocity and crustal thickness. This joint inversion of an unprecedented amount of data has yielded a Moho map and a 3D model for upper mantle *S*-velocities.

Strong lateral variations in the Moho topography have been observed beneath the Mediterranean Sea confirming the complex evolution of this plate boundary region. In the west, the Moho discontinuity has been found at 15-20 km depth, suggesting extended and, at least in some locations, oceanic crust. In the east the crust is on average 25-30 km thick and is interpreted either as Mesozoic oceanic or thinned Precambrian continental crust

covered by thick sedimentary deposits. Standard continental crust (30 to 35 km) is observed along the eastern part of the northern African coast, while to the west a rapid change from a relatively deep Moho (down to 42 km) below the Atlas Mountain Range to the thin crust of the southwestern Mediterranean Sea has been found. The crust beneath the eastern North Atlantic Ocean can be up to 5 km thicker compared to standard oceanic crust (6 km). Serpentinization of the sub-Moho mantle at the Mid-Atlantic ridge could contribute to the imaging of apparently anomalous deep Moho in this region. In Europe, the presence of crustal roots ( $> 45$  km) beneath the major mountain belts has been confirmed, while thin crust ( $< 25$  km) has been found beneath extensional basins.

The 3D upper mantle  $S$ -velocity structure shows strong correlation between the imaged heterogeneities and the tectonics and geology along the plate boundary. The upper mantle along the Eurasia-Africa suture zone is characterized by high-velocity material representing subducted oceanic lithosphere. This signature can be followed to as deep as 300-600 km, depending on the region and/or resolution. A high velocity body, possibly representing a fragment of subducted lithosphere, has been imaged beneath eastern Spain between 250 and 500 km depth. Not only convergence has been recorded in the upper mantle, but also extension has its own signature beneath the Mediterranean. This is particularly clear for the Algero-Provençal and Tyrrhenian Basins, where a shallow asthenospheric layer is observed. The lithosphere-asthenosphere system of the western Mediterranean clearly differentiates itself from the structure of the older eastern Atlantic Ocean as well as from the structure of a young (4 to 20 Ma old) ocean. These observations support the idea that, rather than a young ocean, the western Mediterranean could be a strongly stretched continent, partly affected by spreading, formed at the back of a slab. The structure characterizing the eastern Mediterranean region points to a continuation of the northern African continental lithosphere beneath the sea. Major structural differences in the eastern Atlantic Ocean are imaged between the Mid-Atlantic ridge and the older oceanic basins: the North Atlantic lithosphere is characterized by lower velocities beneath the spreading ridge than under the old ocean basins. Despite strong differences observed in the crustal structure between the Mid-Atlantic ridge and the Azores, no significant differences are observed in the upper mantle  $S$ -velocity structure.

Although only information provided by  $S$ - and Rayleigh waves has been used to derive the presented Moho depth map and upper mantle velocity model, Love waveforms have also been analysed. Discrepancy between 1D path average velocity models obtained from Love and Rayleigh waves travelling through the same region have been observed. The uppermost mantle velocity structure retrieved from Rayleigh data is consistently slower (up to 4%) than velocities obtained from Love wave data. Comparing the 1D average  $S$ -velocity models obtained from Love and Rayleigh waveforms with the global anisotropic model PREM (Dziewonski & Anderson, 1981), we observe a strong analogy. This suggests that the observed incompatibility between the velocity models obtained with the two types of data, at least in part, is due to radial anisotropy in the Mediterranean upper mantle. However, comparison of the results of separate 3D inversions of linear constraints ob-



tained from Love and Rayleigh data suggests that the constraints obtained by the analysis of Love waves might be more inconsistent among each other compared to the constraints in the Rayleigh dataset. Inspection of surface wave sensitivity indicates that such inconsistencies could arise from trade-offs between crustal and upper mantle velocities as well as Moho depth and uppermost mantle velocities, which have been observed to be larger for Love than Rayleigh waves. Bias of the retrieved velocity models due to path deviations with respect to the great circle is instead minimal and falls within the uncertainties for both Love and Rayleigh waves.



# Zusammenfassung

---

Das Mittelmeergebiet ist durch die Grenze zwischen der Eurasischen- und der Afrikanischen-Platte charakterisiert, welche vom Azoren-Tripel-Punkt bis hin zur Türkei verläuft. Diese Region von Plattengrenzen zeigt einzigartige Charakteristika, verglichen mit anderen Suturen. Einerseits ist das auf die zahlreichen semiunabhängigen Mikrokontinente zwischen den Hauptplatten und die unregelmässige Form der konvergierenden Landmassen zurückzuführen. Andererseits weist die Grenze zeitlich sehr unterschiedliche Konvergenzeigenschaften (in Geschwindigkeit und Richtung) auf. Die daraus resultierende Tektonik und Geodynamik ist entsprechend sehr kompliziert und durch stark lateral variierende Prozesse sowohl in der Vergangenheit wie auch in der Gegenwart gekennzeichnet.

Wir haben in unseren Untersuchungen neue seismische Daten verwendet, um die Moho-Diskontinuität zu kartieren und die *S*-Wellengeschwindigkeitsstruktur des oberen Mantels in der Afrikanisch-Eurasischen Suturenzone zu rekonstruieren und zwar mit einer anderen Studienkomplementären Auflösung. Die Daten wurden mit Hilfe von 25 Breitband-Seismometern, welche entlang der Plattengrenze temporär installiert wurden (MIDSEA-Projekt) aufgezeichnet. Zusätzlich sind Daten von festinstallierten Geräten verwendet worden. Anschliessend haben wir mit der sogenannten Partitioned Waveform Inversion Methode die *S*- und Rayleigh-Wellenzüge von mehr als 1100 Seismogrammen interaktiv gefittet. Die so erhaltenen linearen Beziehungen zwischen der *S*-Wellengeschwindigkeit im oberen Mantel und der Moho-Tiefe sind mit unabhängigen Schätzungen der Moho-Tiefe kombiniert worden, wobei letztere aus publizierten Reflexions- und Refraktionsuntersuchungen, Gravimetriestudien und Receiver Function Analysen entnommen wurden. Anschliessend hat man mit Hilfe der kombinierten Daten eine lineare gedämpfte Inversion (least square) für die *S*-Wellengeschwindigkeit und die Krustendicke durchgeführt. Diese gemeinsame Inversion einer grossen Menge an Daten führte zu einer Moho-Karte und einem 3D Modell der *S*-Wellengeschwindigkeiten im oberen Mantel.

Wir haben starke laterale Variationen der Moho-Topographie im Mittelmeer festgestellt, was die komplexe Entwicklungsgeschichte der Plattengrenzen in dieser Gebiet bestätigt. Im Westen konnte die Moho-Diskontinuität in einer Tiefe von 15-20 km festgestellt werden, was auf eine gedehnte und, zumindest an einigen Orten auf eine ozeanische Kruste hindeutet. Im Osten dann, ist die Kruste durchschnittlich 25-30 km mächtig und kann entweder als mesozoisch-ozeanische oder verdünnte präkambrisch-kontinentale Kruste mit einer dicken Sedimentschicht interpretiert werden. Normale kontinentale Kruste (30 bis 35 km) kann man im östlichen Teil der nordafrikanischen Küste finden. Dagegen beobachtet man im Westen einen raschen Wechsel von einer relativ tiefen Moho (bis zu 42 km) unter der Atlasgebirgskette zu einer dünnen Kruste im südwestlichen Mittelmeer. Unterhalb des östlichen Nordatlantiks ist die Kruste bis zu 5 km dicker verglichen mit einer normalen ozeanischen Kruste (6 km). Diese ungewöhnlich tiefe Moho könnte man auf eine Serpentinisierung im Sub-Moho Bereich in der Region des Mittelatlantischen-Rückens zurückführen. Schliesslich konnten wir mit unserem Modell die Krustenwurzeln mit einer Dicke von mehr als 45 km unterhalb der grösseren Gebirgszüge in Europa nachweisen. Ebenso haben wir unter Extensionsbecken eine dünne Kruste von weniger als 25 km Mächtigkeit gefunden.

Die 3D *S*-Wellengeschwindigkeitsstruktur des oberen Mantels zeigt eine deutliche Korrelation zwischen den abgebildeten Heterogenitäten, der Tektonik und der Geologie entlang der Plattengrenze. In der Eurasisch-Afrikanischen Suturezone weist der obere Mantel eine Hochgeschwindigkeitszone auf, die mit subduzierter ozeanischer Lithosphäre erklärt werden kann. Die Zone ist bis in eine Tiefe von 300-600 km (in Abhängigkeit vom Ort und der Auflösung) ersichtlich. Eine weitere Zone hoher Geschwindigkeit konnte unterhalb Ostspanien, in einer Tiefe von 250 bis 500 km aufgelöst werden. Möglicherweise stellt dieser Körper ein Fragment subduzierter Lithosphäre dar. In der Mittelmeerregion wurden jedoch nicht nur Konvergenz-, sondern auch Extensionsgebiete im oberen Mantel festgestellt. Deutlich sichtbar ist dies insbesondere im Algero-Provençal und im tyrrhenischen Becken, wo oberflächennahe Asthenosphärenschichten zu sehen sind. Das Lithosphären-Asthenosphären-System im westlichen Mittelmeer unterscheidet sich nicht nur sehr deutlich vom älteren östlichen Atlantik, sondern auch von der Struktur eines jüngeren (4 bis 20 Ma alten) Ozeans. Es handelt sich sehr wahrscheinlich um einen gedehnten Kontinent (teilweise durch Spreading gekennzeichnet), welcher auf der Rückseite einer subduzierenden Platte entstanden ist. Im östlichen Mittelmeer deuten die Strukturen auf eine Fortsetzung der nördlichen afrikanischen kontinentalen Lithosphäre hin. Die grössten strukturellen Unterschiede konnten im östlichen Atlantik, zwischen dem Mittelatlantischen-Rücken und den älteren atlantischen Becken gefunden werden: unterhalb des Rückens dominieren tiefer Geschwindigkeiten als unter den ozeanischen Becken. Obschon die Krustenstruktur zwischen dem Mittelatlantischen Rücken und den Azoren starke Unterschiede aufweist, können selbige in der *S*-Wellengeschwindigkeitsstruktur des oberen Mantels nicht gefunden werden.

Ein Vergleich der durchschnittlichen 1D-Geschwindigkeitsmodelle von Love- und Ray-

leighwellen, welche durch die selben Regionen gelaufen sind, zeigt eine deutlich geringere Geschwindigkeit (rund 4%) der Rayleighwellen auf. Vergleicht man jedoch die aus den Wellenformen von Love- und Rayleighwellen gewonnen durchschnittlichen S-Wellengeschwindigkeiten mit jenen aus dem globalen anisotropischen Modell PREM (Dziewonski & Anderson, 1981), so stellt man eine gute Übereinstimmung fest. Daraus lässt sich schliessen, dass der Unterschied zwischen den Geschwindigkeitsmodellen aus den beiden Datensätzen (Love und Rayleigh) zumindest teilweise auf radiale Anisotropie im oberen Mantel zurückzuführen ist. Betrachtet man jedoch die Resultate der getrennten 3D-Inversion von Love- und Rayleighdaten, so scheinen die Parameter aus der Analyse der Lovewellen inkonsistenter zueinander zu sein, als jene aus den Rayleighwellen. Eine Untersuchung von Oberflächenwellen-Sensitivitäten deutet darauf hin, dass diese Inkonsistenz auf Kompromisse zwischen den Krusten- und oberen Mantelgeschwindigkeiten wie auch auf jene zwischen der Moho-Tiefe und den Geschwindigkeiten im obersten Teil des Mantels (welche für Lovewellen höher sind als für Rayleigh) zurückzuführen sind. Systematische Fehler der Geschwindigkeitsmodelle auf Grund von Abweichungen in den Laufpfaden vom Grosskreis sind dagegen klein und fallen in die Unsicherheiten von Love- und Rayleighwellen.



# Introduction

---

The Mediterranean region is characterized by the tectonic plate boundary between the Eurasian and African plates, extending from the Azores triple junction to Turkey and the easternmost Mediterranean Sea (Fig. 1.1). This plate boundary region shows unique characteristics compared to other suture zones around the world. Uncommonly, it does not manifest itself as a relatively focused zone, but surface deformation, seismicity and earthquake focal mechanisms indicate a wide, diffuse and/or branched plate boundary. Moreover, due to the presence of several semi-independent microcontinents between the two major plates, the suture zone has changed location, shape and character throughout geological time (Dercourt et al., 1986). In addition, due to the irregular shape of the converging landmasses and to different converging patterns (velocity and direction) through time, the resulting tectonics and geodynamics dominating this region are highly complicated and strong lateral variations in the past and present ongoing processes are observed. Despite of slow convergence acting as the primary tectonic process in the region, different types of deformation affect and affected different parts of the suture zone. The plate boundary is not characterized by a single, continuous subduction zone, but several arcs with different orientations were active in different periods. Moreover, strike-slip and extension are also important tectonic processes influencing the region, e.g. along the western part of the plate boundary (Azores-Gibraltar fracture zone) and in back-arc basins, respectively. Unique of the Mediterranean region is also the small scale of complexity: typical lengths of the tectonic provinces span  $1^{\circ}$ - $5^{\circ}$ .

A deeper understanding of the interaction between the Eurasian and African plates would not only shed light on regional tectonics and geodynamics within the Mediterranean but

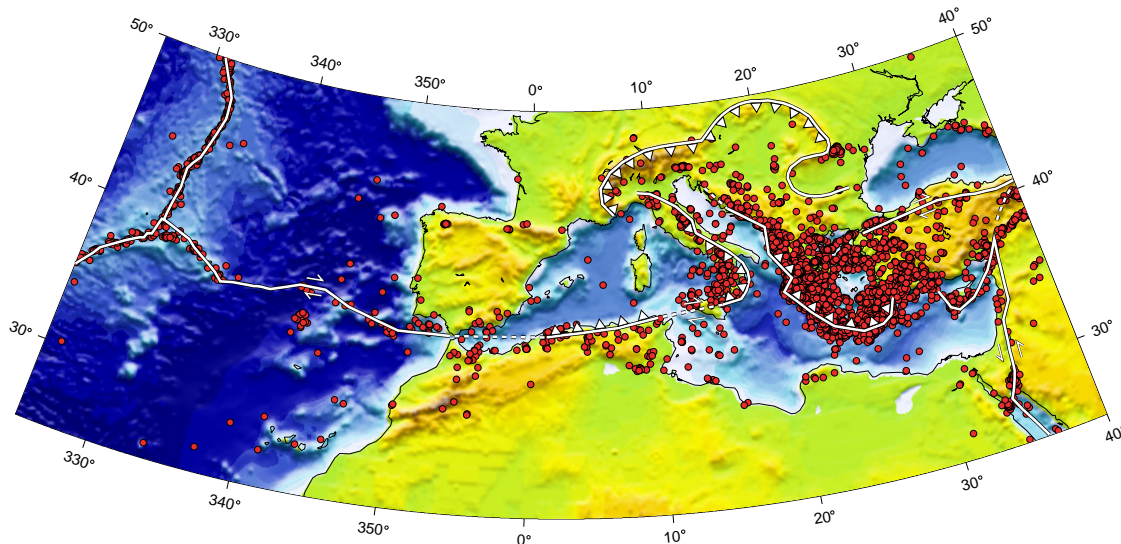


**Figure 1.1:** Topographic map of the Eurasia-Africa plate boundary region with approximate plate boundary location and seismicity. Curves with sawtooth pattern indicate the present location of the convergent boundary, with sawteeth pointing in the direction of subduction or underthrusting. Arrows represent strike-slip. Red dots are epicenters of events occurred between 1964 and 1998 (Engdahl et al., 1998).

also help the understanding of slow, long term plate convergence. Moreover, the uniqueness of the tectonic scales and complexity of plate boundary deformation and microplates motion and accretion observed in the Mediterranean region can hold answers to fundamental questions in geophysics and geodynamics, which may not be found in other, less complex, plate boundary regions. Fundamental for a deeper understanding of the evolution, deformation and dynamics of such a complex region, is the detailed knowledge of its crustal and upper mantle structure. A 3D velocity model displays the expression of the tectonic phenomena and the related deep processes in the distribution of shear velocity anomalies and gives the opportunity to answer questions about the nature of the Mediterranean basins, the style of past subduction, the configuration of subducted lithosphere and differences in oceanic and continental lithosphere-asthenosphere systems. Of particular importance is the comparison of the Mediterranean with the Atlantic part of the model. Such comparison will highlight the variety of tectonic processes modeling different parts of the suture zone.

A detailed crustal and upper mantle structure also provides a tool for removing wave propagation effects from seismograms, so reducing the uncertainties in earthquake location and focal mechanisms determination, in particular in highly heterogeneous regions,



---

as for instance along a plate boundary. Moreover a detailed crustal model, which assures accurate crustal corrections, is essential to prevent mapping crustal features in upper mantle tomographic images and so biasing the modeled structure, since most datasets used in mantle seismic tomography are sensitive to crustal structure, but cannot resolve details within the crust.

Our goal is to develop a crustal thickness map and upper mantle  $S$ -velocity model for the Eurasia-Africa plate boundary region with unprecedented resolution. High resolution upper mantle images can be obtained by waveform fitting methods, such as the Partitioned Waveform Inversion (PWI) technique (Nolet, 1990). In this method full wave trains of regional seismograms from ray paths traversing the region of interest are modeled. Most energy in these wave trains has travelled through the upper mantle and makes PWI a very efficient technique to obtain high-resolution images of the upper mantle velocity structure.

However, a major requirement to achieve this goal is a more homogeneous data coverage of the Mediterranean region. Therefore, during the international MIDSEA project (Mantle Investigation of the Deep Suture between Eurasia and Africa) (Van der Lee et al., 2001) we deployed 25 broad band 3 component seismic stations along the plate boundary region. This temporary network, as well as the data processing, are described in Chapter 2.

In the two following chapters the results of the tomographic inversion are presented. Chapter 3 is devoted in particular to the description of the obtained Moho depth map. Strong lateral variations in the Moho topography have been observed, confirming the complex evolution the Mediterranean region. This new Moho depth model has also been used to assess Airy isostatic compensation in the Eurasia-Africa plate boundary region. The upper mantle  $S$ -velocity structure beneath the Mediterranean region and the eastern Atlantic Ocean is discussed in Chapter 4. Interesting features are highlighted and interpreted based on the results of resolution tests. For example, a new striking and resolved feature of our  $S$ -velocity model is a high velocity anomaly imaged beneath eastern Spain between 250 and 500 km depth, which we interpret as a fragment of subducted lithosphere detached in an early stage of the subduction process in the western Mediterranean. Moreover, the diversity of the lithosphere-asthenosphere structure imaged beneath the basins in the Mediterranean and Atlantic region strongly points to the variety of tectonic processes modeling the different parts of the suture zone.

Although only information provided by  $S$ - and Rayleigh waves has been used to derive the presented Moho depth map and upper mantle velocity model, Love waveforms have also been analysed. Chapter 5 describes several tests performed to understand the different ability of Rayleigh and Love waves to determine Earth structure.

Additional work done during my PhD, but not presented in this thesis, has been published as: M. van der Meijde, F. Marone, D. Giardini, S. van der Lee, 2003. Seismic

evidence for water deep in Earth's upper mantle, *Science*, **300**, 1556-1558.

## MIDSEA Project

---

A major requirement of achieving a Moho depth map and an upper mantle *S*-velocity model for the Eurasia-Africa plate boundary region with unprecedented resolution, is a more homogeneous data coverage of the studied area. The main aim of the international MIDSEA (Mantle Investigation of the Deep Suture between Eurasia and Africa) project (Van der Lee et al., 2001) was to complement and extend the existing data coverage by installing 25 broad band 3 component seismic stations (Fig. 2.1). This project was a joint venture mainly between the Federal Institute of Technology (ETH, Switzerland), Géosciences Azur (CNRS/UNSA, France), the National Institute of Geophysics and Volcanology (INGV, Italy), and the Department of Terrestrial Magnetism of the Carnegie Institution of Washington (DTM, USA). The other MIDSEA partners were the National Observatory of Athens (NOA, Greece), the University of Zagreb (Croatia), the Ebre Observatory (Spain), the Institute of Catalan Studies (Spain), the Lanzarote Cabildo (Spain), the San Fernando Naval Observatory (ROA, Spain), the U. Complutense Madrid (Spain), the Institute of Meteorology (Portugal), the Research Center for Astronomy, Astrophysics and Geophysics (CRAAG, Algeria) and the Libyan Center for Remote Sensing and Space Sciences (LCRSSS, Libya).

In 1998, when the idea of the MIDSEA project was conceived, more than 60 broad band seismic stations, belonging mainly to the Global Seismographic Network (GSN), MedNet, GEOFON and to individual national networks, were already in operation in the Mediterranean region. From then onwards the number of permanent broad band stations installed in the Mediterranean region as well as mobile broad band stations deployed for limited periods of time has steadily increased. However, data availability for some of the permanent and temporary stations is variable and the geographical coverage far from

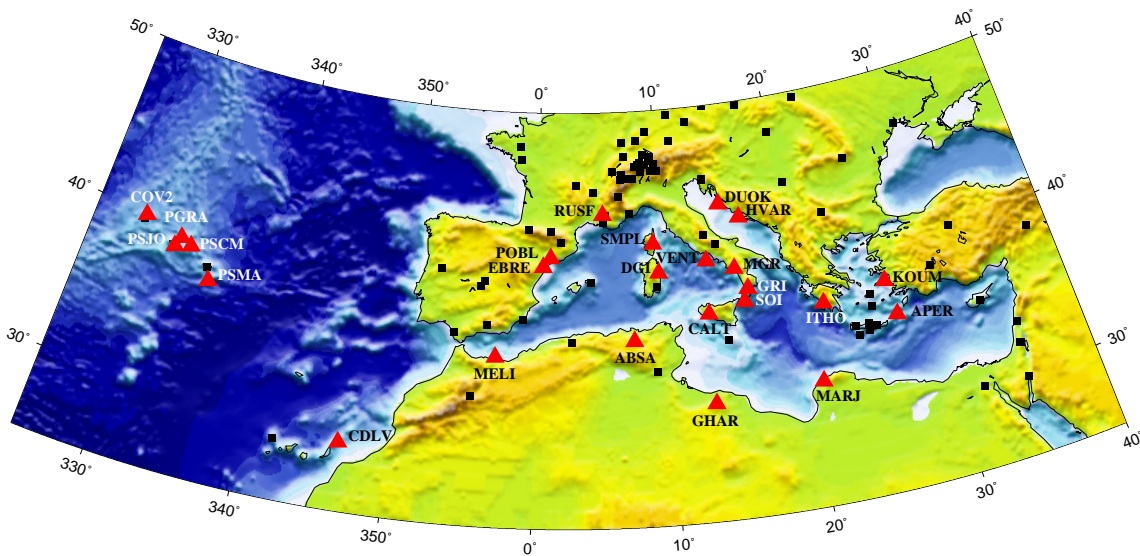


**Figure 2.1:** Configuration of the MIDSEA stations (red triangles) and other seismic stations (black squares) in the Eurasia-Africa plate boundary region.

uniform. The black squares in Fig. 2.1 represent broad band seismic stations, which delivered useful data to study the 3D crustal and upper mantle structure in the Mediterranean region. While station coverage for Spain and Central Europe is sufficiently dense, for regions such as the Azores archipelago, northern Africa and large areas of the Mediterranean Sea the station density is not high enough to achieve the required data coverage. The MIDSEA network (Tab. 2.1 and red triangles in Fig. 2.1) was designed in such a way to increase the station density, especially in the southern and western part of the target region, reduce the heterogeneities in and complement the existing station coverage. Target locations for our new 3 component broad band seismic stations were regions on both sides of the plate boundary that were far from existing stations. Therefore, most of the MIDSEA stations were installed on islands as well as along the northern Africa coast.

## 2.1 Station instrumentation and installation

Each MIDSEA station has been in operation for 1 up to 2 years in the period from June 1999 through May 2002. Twenty-two of the 25 stations were equipped with broad band STS2 sensors, the remaining 3 with CMG3T sensors. The data acquisition systems used are MARS88, RefTek, Titan, Quanterra and Orion (Fig. 2.2). The correct time on the recorded signals was guaranteed by GPS synchronization. Most stations were installed in existing sites, where other instruments, such as short period seismometers, were operated. Site characteristics throughout the MIDSEA network were quite heterogeneous and varied

**Table 2.1:** Location and instrumentation of the MIDSEA stations.

Code	Location	Latitude	Longitude	Altitude (m)	Sensor	Digitizer
CDLV	Spain	29.163	-13.444	37	STS2	MARS88
EBRE	Spain	40.823	0.494	36	STS2	MARS88
MELI	Spain	35.290	-2.939	40	STS2	Q380
POBL	Spain	41.379	1.085	550	STS2	Orion
DUOK	Croatia	44.113	14.932	115	STS2	MARS88
HVAR	Croatia	43.178	16.449	250	STS2	MARS88
APER	Greece	35.550	27.174	250	STS2	MARS88
ITHO	Greece	37.179	21.925	400	STS2	MARS88
KOUM	Greece	37.704	26.838	340	STS2	MARS88
GHAR	Libya	32.122	13.089	650	STS2	Q680
MARJ	Libya	32.523	20.878	650	STS2	MARS88
CALT	Italy	37.579	13.216	955	STS2	RefTek
DGI	Italy	40.318	9.607	343	STS2	Titan
GRI	Italy	38.822	16.420	525	STS2	Titan
MGR	Italy	40.138	15.553	297	CMG3T	Titan
SOI	Italy	38.073	16.055	300	CMG3T	Titan
VENT	Italy	40.795	13.422	110	CMG3T	RefTek
ABSA	Algeria	36.277	7.473	1025	STS2	MARS88
RUSF	France	43.943	5.486	520	STS2	Titan
SMPL	France	42.094	9.285	405	STS2	Titan
COV2	Portugal	39.677	-31.113	194	STS2	RefTek
PGRA	Portugal	39.029	-27.981	245	STS2	RefTek
PSCM	Portugal	38.701	-27.117	400	STS2	RefTek
PSJO	Portugal	38.422	-28.303	258	STS2	RefTek
PSMA	Portugal	36.996	-25.131	249	STS2	RefTek

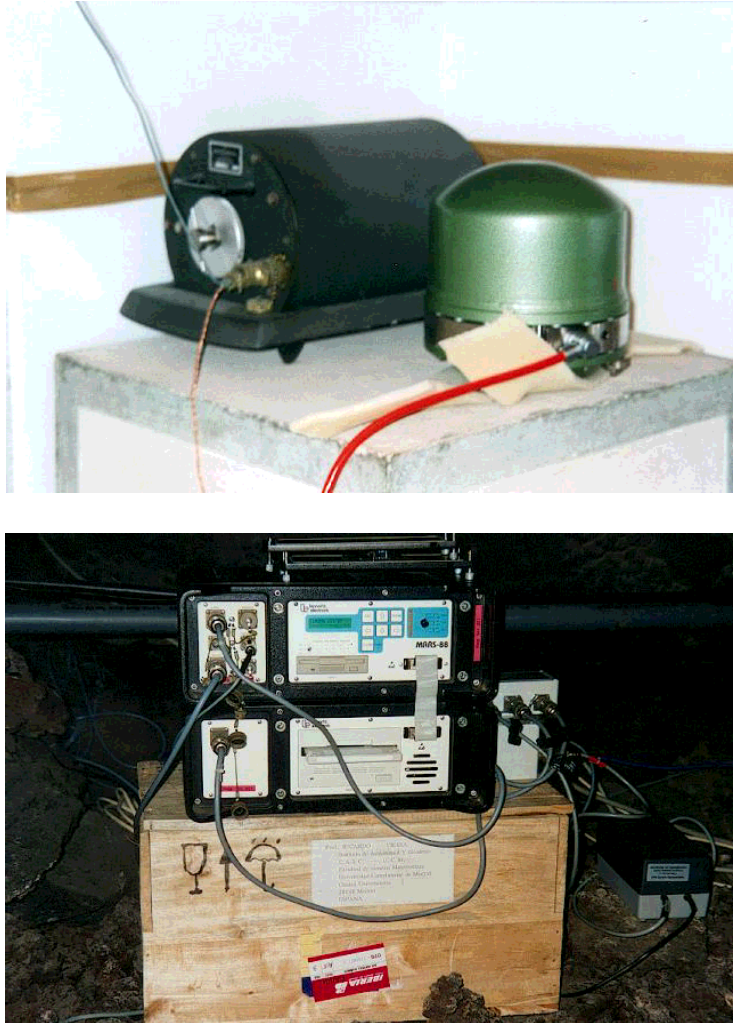


**Figure 2.2:** STS2 seismometer (green igloo) installed on a pier of concrete on the top and a MARS88 acquisition system on the bottom.

from a lava tunnel (CDLV) through a vault (EBRE) to just a normal room in a secluded building (e.g. DUOK) or even in an apposite hut (e.g. APER). When available, the sensor was installed on a pier of concrete, which has a good coupling with the bedrock. In particular broad band seismometers are extremely sensitive to temperature variations and air convection. We achieved thermal shielding and reduced the effects of air currents by wrapping the seismometers with cotton wool or rubber foam and with a radiation reflecting rescue sheet. Air circulation was also limited by covering everything with a styrofoam box (Fig. 2.3).



**Figure 2.3:** Installation procedure: STS2 seismometer (top left), wrapped with cotton wool (top right) and a radiation reflecting rescue sheet (bottom left), everything covered with a styrofoam box (bottom right).

## 2.2 Data processing and quality

The data recorded by the stations was locally stored on 650 Mb optical disks, regularly collected by local station managers and shipped to one of the four data processing centers: the Federal Institute of Technology (ETH, Switzerland), Géosciences Azur (CNRS/UNSA, France), the National Institute of Geophysics and Volcanology (INGV, Italy), and the Department of Terrestrial Magnetism of the Carnegie Institution of Washington (DTM, USA). The Institute of Catalan Studies (Spain) and the San Fernando Naval Observatory (ROA, Spain) were locally processing the data recorded at stations POBL and MELI, respectively.

The data has been recorded continuously with a sampling rate of 31.25 Hz. At the ETH, we were in charge of processing the data acquired with MARS88 systems. Approximately one month of data in MARS88 format for one station was stored on one optical disk. After arriving, the data was downloaded to a hard disk and manually checked for signal interruptions (e.g. long power failure, GPS malfunctioning) or distortions (e.g. seismometer tilting). The continuous data in MARS88 format was backed up on 2.3 Gb optical disks and on 4.0 Gb DAT tapes. Single days data files for each station were then created, converted to GSE2 format and archived on 4.0 Gb DAT tapes. Finally, events have been extracted from the continuous data, converted to GSE2 and stored on CDs. The criteria for the events selection took into account the variety of studies planned by the MIDSEA partners. The event database is therefore containing records of local (e.g. for local seismicity studies), regional (e.g. for crustal and mantle structure studies and moment tensor determination) and teleseismic earthquakes (e.g. for discontinuities characterization and body wave tomography). Even noise recordings are being analysed for example to gain information on sites characteristics. The complete event database will be soon available to the scientific community through the ORFEUS (<http://orfeus.knmi.nl>) and IRIS (<http://www.iris.washington.edu>) data centers.

Despite the temporary character of the MIDSEA network, some of the station sites have proven to be excellent locations for the operation of new permanent stations. For example, station CALT (Sicily) has recently been converted to a permanent MedNet station, and two of the MIDSEA stations in northern Africa (GHAR and MELI) are now part of the GEOFON network. Simple noise analysis shows that noise levels at seismic frequencies are close to the low-noise model of Peterson (1993) for some of the sites that will continue to operate narrower band sensors in the future (Algeria, Croatia, Greece, Lanzarote). The Greek and Croatian island sites show a very low microseismic noise level, whereas at the same frequencies the noise level is significantly higher for the Atlantic island sites. As usual, long period noise is higher on the horizontal than on the vertical components. For some sites increased cultural noise above 5 Hz is observed during the day.



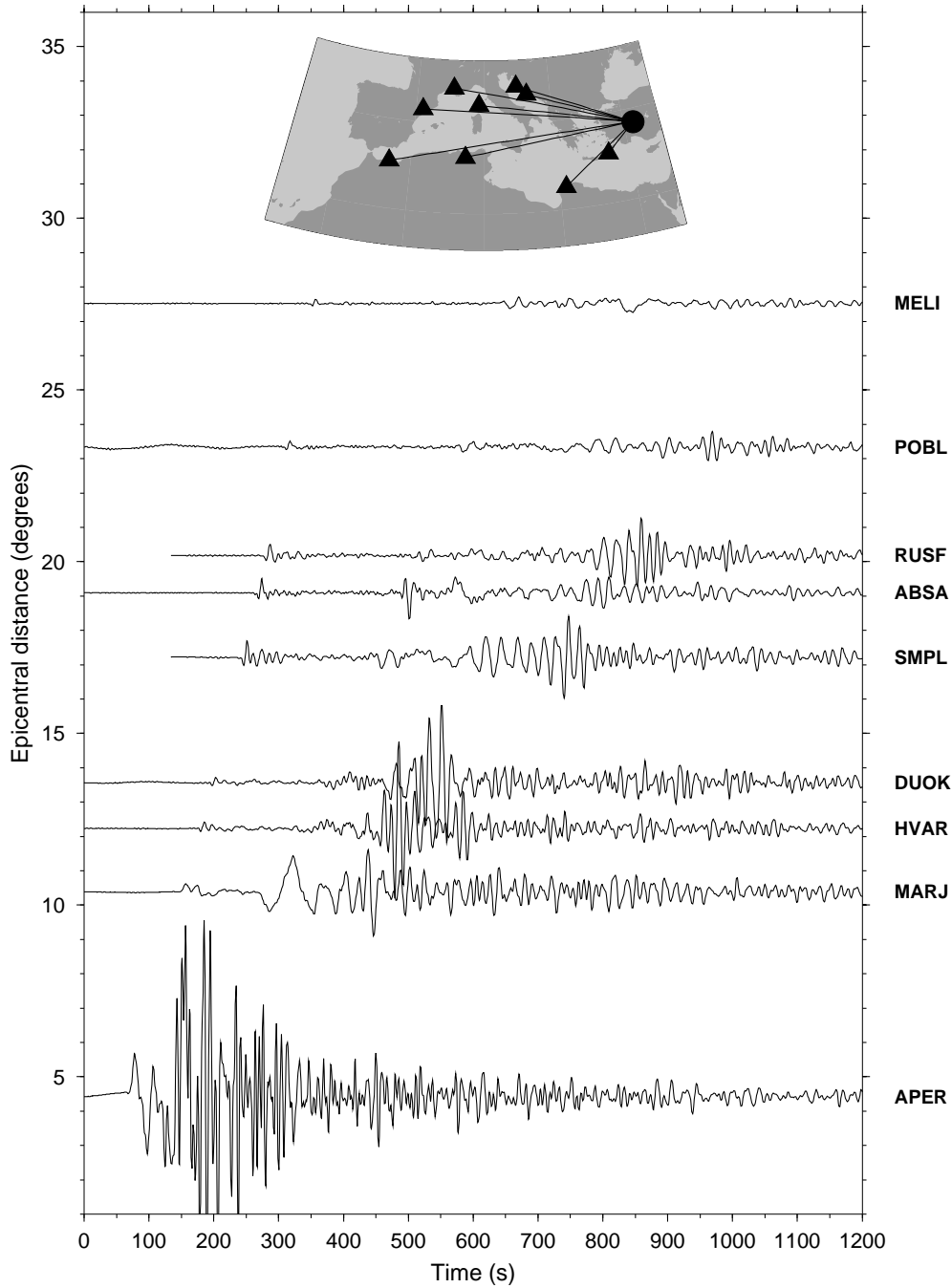


**Figure 2.4:** Vertical component seismograms section for the regional event on December 15, 2000,  $m_w$  6.2, in Turkey.

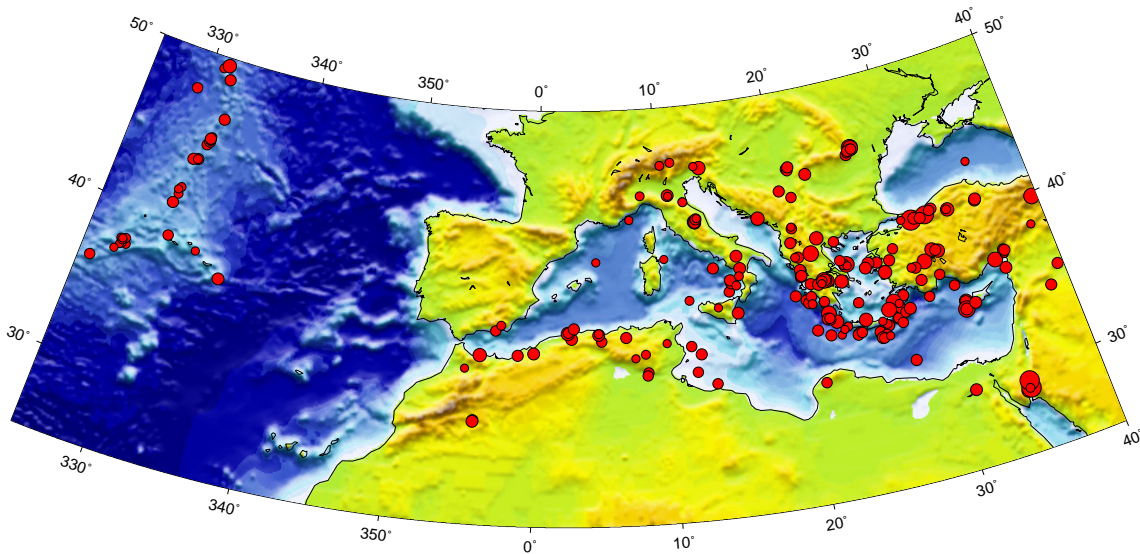


**Figure 2.5:** Distribution of all earthquakes used in this study. The circles are scaled with magnitude.

### 2.3 Improved data coverage for crust and upper mantle studies

For the study of the crustal and upper mantle structure along the Eurasia-Africa plate boundary we are particularly interested in regional events. Significant regional earthquakes recorded by the MIDSEA stations include the 1999 Izmit-Duzce series, the 1999 Athens earthquake, an intermediate depth event beneath Crete (2002) and a couple of events in southwestern Turkey (2000 and 2002). An example of seismograms of a large regional earthquake recorded by MIDSEA stations is illustrated in Fig. 2.4. All events and paths used in this study are shown in Figs. 2.5 and 2.6. Thanks to the higher station density in the Mediterranean region achieved by the MIDSEA project, average epicentral distances have been reduced. The analysis of short wave paths to study the crustal and upper mantle structure in the complex Mediterranean region was essential to avoid phases distorted by unmodeled scattered energy. Owing to the denser station distribution, also smaller earthquakes in low seismicity regions could be recorded with a signal-to-noise ratio sufficient for data analysis, significantly improving the existing paths coverage.

An at least equally important determinant for the resolution power of surface wave tomography in the Mediterranean region were recent programs focused on the systematic determination of source mechanisms of small/medium size regional earthquakes, which would however not be studied by international agencies. Particularly complete and reliable is the collection of moment tensor solutions determined at the ETHZ (Braunmiller et al., 2002) and available online (<http://seismo.ethz.ch/info/mt.html>). Up to 58% of the seismograms

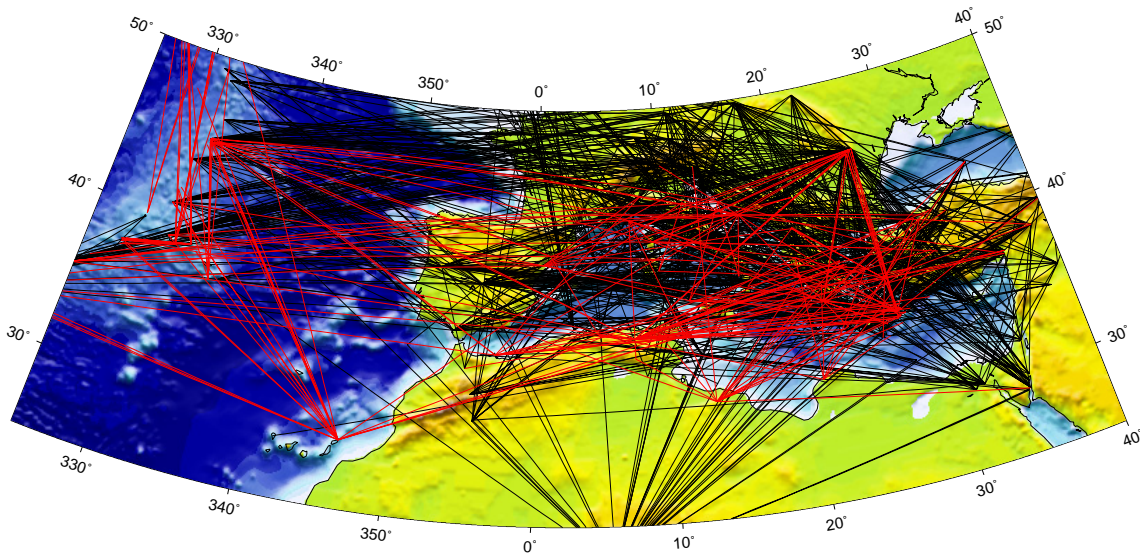


**Figure 2.6:** Path coverage achieved in this study: in red paths for seismograms recorded at MIDSEA stations, in black the other paths.

recorded by MIDSEA stations and used in this study could be analysed thanks to recent catalogues of source mechanisms for small/medium regional earthquakes (among others Braunmiller et al., 2002). The combination of the MIDSEA stations together with systematic regional source mechanism determination significantly contributed to complement and extend the existing data coverage especially in the western Mediterranean Basin, in northern Algeria, in Italy, in the central Mediterranean Sea, in the Atlantic Ocean and along the Mid-Atlantic ridge (Fig. 2.6).



# Joint inversion of local, regional and teleseismic data for crustal thickness in the Eurasia-Africa plate boundary region

---

## 3.1 Summary

A new map for the Moho discontinuity (EAM02) in the Eurasia-Africa plate boundary region is presented. Reliable results have also been obtained for the southern and eastern Mediterranean Basin, the northern African coasts and the eastern Atlantic Ocean, regions only occasionally considered in studies on the Mediterranean region. The Moho topography model is derived from two independent sets of constraints. Information contained in the fundamental and higher mode Rayleigh waves obtained from waveform modeling is used to constrain the Moho depth between estimates of crustal thickness taken from published reflection and refraction surveys, gravity studies and receiver function analysis. Strong lateral variations in the Moho topography have been observed in the Mediterranean Sea confirming the complex evolution of this plate boundary region. In the west, the Moho discontinuity has been found at 15-20 km depth, suggesting extended and, at

---

\*This chapter has been accepted for publication in *Geophys. J. Int.* as: F. Marone, M. van der Meijde, S. van der Lee, D. Giardini, Joint inversion of local, regional and teleseismic data for crustal thickness in the Eurasia-Africa plate boundary region.

least in some locations, oceanic crust, while in the east the crust is on average 25-30 km thick. There it is interpreted either as Mesozoic oceanic or thinned Precambrian continental crust covered by thick sedimentary deposits. Standard continental crust (30 to 35 km) is observed along the eastern part of the northern African coast, while to the west a rapid change from a relatively deep Moho (down to 42 km) below the Atlas Mountain Range to the thin crust of the southwestern Mediterranean Sea has been found. The crust beneath the eastern North Atlantic Ocean can be up to 5 km thicker compared to standard oceanic crust (6 km). The crust has been interpreted to be heterogeneous as a consequence of irregular magma supply at the Mid-Atlantic ridge. In addition, serpentinization of the sub-Moho mantle could contribute to the imaging of apparently anomalous thick oceanic crust. In Europe, the presence of crustal roots ( $> 45$  km) beneath the major mountain belts has been confirmed, while thin crust ( $< 25$  km) has been found beneath extensional basins. Comparing the obtained Moho topography and Moho depth computed assuming isostatic compensation at 60 km depth shows that most of the Mediterranean and eastern Atlantic region appears in isostatic equilibrium. The large positive residuals observed for the eastern Mediterranean are likely due to overestimating crustal thickness, owing to the thick sediment deposits present.

## 3.2 Introduction

The Eurasia-Africa plate boundary region (Fig. 3.1), extending from the Azores triple junction in the Atlantic Ocean to Turkey and the easternmost Mediterranean Sea, is a tectonically complex area.

A better knowledge of the crustal structure in a region so complex as the Mediterranean is important to better understand the past and present tectonic and geodynamic evolution. A detailed crustal model will also improve the accuracy of locating local and regional earthquakes. Moreover, since most datasets used in mantle seismic tomography are sensitive to crustal structure, but cannot resolve details within the crust, accurate crustal corrections are essential to prevent mapping crustal features in upper mantle tomographic images and so biasing the modeled structure.

Since a major requirement of achieving a more detailed Moho depth map is more homogeneous data coverage of the Mediterranean region, a temporary network consisting of 25 broad band three-component seismic stations has been installed in the Eurasia-Africa plate boundary area during the international MIDSEA (Mantle Investigation of the Deep Suture between Eurasia and Africa) project (Van der Lee et al., 2001). Careful placing of the single seismic stations complements the data coverage provided by existing networks and stations in the region. Consequently, most MIDSEA stations are located on islands as well as in northern Africa.

This study presents a new map for the Moho in the Eurasia-Africa plate boundary region. We combine new surface wave data recorded by the MIDSEA network with new information from recent refraction/reflection profiles (e.g. Doser et al., 1997; Bohnhoff

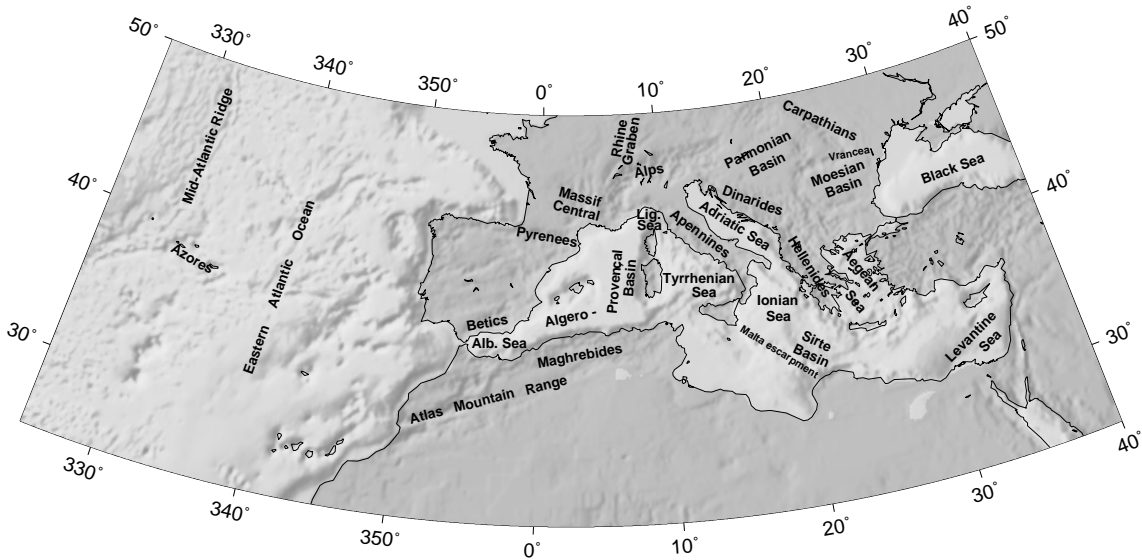


**Figure 3.1:** Topographic map of the Eurasia-Africa plate boundary region.

et al., 2001), receiver function analyses (e.g. Sandvol et al., 1998; Van der Meijde et al., 2003b) and gravity studies (e.g. Mickus & Jallouli, 1999). We present the first map for the Moho depth covering the whole Mediterranean with reliable results for the southern and eastern Mediterranean Basin, the northern African coasts and Atlantic Ocean. This Moho map has been used to assess first-order Airy isostatic compensation in the Mediterranean region.

### 3.2.1 Tectonic background

The Mediterranean Basin is mainly dominated by slow convergence between Africa and Eurasia, accommodated by subduction of Mesozoic oceanic lithosphere, e.g. along the Hellenic and the Calabrian arc, and by the formation of curved Paleo- and Neogene orogenies such as the Alps, Carpathians, Betics and Rif, Calabria and Apennines, Hellenides and Dinarides and Maghrebides. Although convergence acts as the primary plate tectonic process in this region, back-arc basins such as the Algero-Provençal, Tyrrhenian and Aegean Basins have also been formed during episodes of relatively fast extension related to slab retreat. Moreover, the Azores archipelago is characterized by transtensional deformation, while in the eastern Atlantic Ocean the major ongoing process is strike-slip faulting. The complex tectonic evolution of the plate boundary region, described in detail in Dercourt et al. (1986), Dewey et al. (1989), De Jonge et al. (1994) and Wortel & Spakman (2000), yields a complex 3D crustal structure with large and small-scale features and a strongly perturbed crust-mantle boundary.

### 3.2.2 Previous studies

The Mohorovičić (Moho) discontinuity has been the target of several crustal studies published for parts of the Mediterranean region. Detailed local studies exist for parts of Italy (Egger, 1992), Spain (Banda et al., 1981a,b) and Greece (Makris, 1985). The results of these local studies have been used to compile regional models for the Mediterranean region. In 1987, Meissner et al. (1987) presented a Moho map for the Mediterranean area from Spain to Greece but not covering the southern and eastern part of the Mediterranean Sea. Although their map is constrained by a large amount of seismic data, it still shows large regions whose Moho depth is based only on interpolation. At the same time Geiss (1987) published a similar work but with additional seismological data for northern Africa, especially Morocco, Egypt and Israel. However, the uncertainties on Moho depth in the eastern and southern parts of his map are as large as 10 km. More recently, Du et al. (1998) compiled a 3D regionalized model of the European crust and upper mantle velocity structure including the southern Mediterranean region and northern Africa, but using a regional averaged model for these areas.

One of the first surface-wave dispersion studies, presenting regionalization of the crust for parts of the Mediterranean region, has been published by Calcagnile & Panza (1990). The recent regional crustal model of Pasyanos & Walter (2002), also derived from surface-wave dispersion results, covers a broader region than the studies above. However, the average scale of the mapped features, especially in the Mediterranean region, is not comparable to the size of the structures observed there, owing to data characteristics and the long-path seismograms used.

The Mediterranean is also described in global models for the earth crust by Mooney et al. (1998) and Bassin et al. (2000). The first compilation is specified on a coarse grid of  $5^\circ \times 5^\circ$ . Bassin et al. (2000) updated the previous model with more current global sediment and crustal thickness data. This refined version is defined on a  $2^\circ \times 2^\circ$  grid. However, for the oceanic region and the Mediterranean Sea the model is poorly constrained by data, owing to the lack of refraction and reflection studies in these regions. Even this finer grid still gives too coarse and rough a view of the crust in so complex a region as the Mediterranean, where small-scale structures are expected.

All the aforementioned studies have some drawbacks. Local investigations are too limited compared to the scale of the Mediterranean area. Conversely, regional models suffer from inhomogeneous data coverage, causing large regions to be constrained only by interpolated values for the Moho depth. Furthermore, the algorithm used to interpolate between point measurements of regional compilations is based only on a mathematical approach (mainly linear interpolation). Regional crustal models derived from surface wave dispersion measurements suffer from the averaging out of small-scale features characteristic to the Mediterranean region. Nor are global compilations accurate enough in describing the spatial variation in the Moho topography there.

Detailed Moho depth maps for the eastern Atlantic Ocean hardly exist. The available



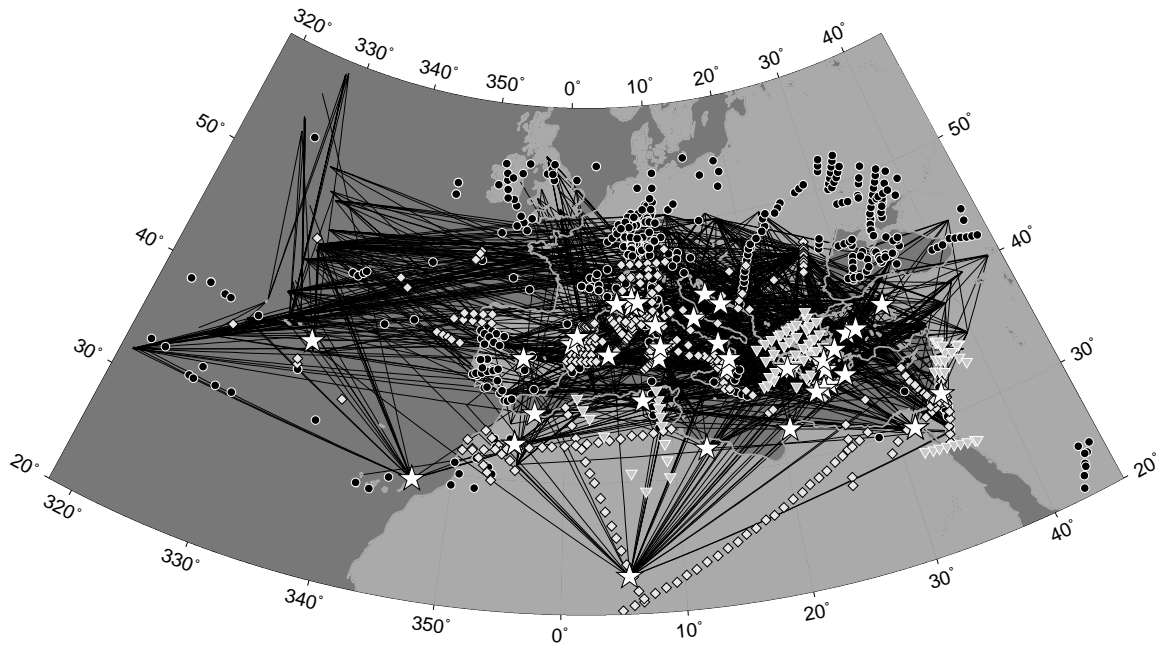


**Figure 3.2:** Geographical distribution of constraints used in the 3D inversion: wave paths (solid lines) that produced linear constraints through waveform fitting and locations with previous observations of the crustal thickness (white stars: receiver function studies, black circles: dataset of Mooney et al. (2002), grey diamonds: refraction and reflection profiles, grey inverted triangles: gravity studies)(see the Appendix A for a complete list of references).

studies are either reflection and refraction profiles for selected locations (e.g. Potts et al., 1986; Pinheiro et al., 1992) or global crustal thickness compilations (e.g. Mooney et al., 1998) based mainly on average crustal models and only poorly constrained by data.

### 3.3 Data

Our Moho map for the Mediterranean region is derived from two independent sets of constraints (Fig. 3.2). The primary dataset includes estimates of crustal thickness taken from published reflection and refraction surveys, gravity studies and receiver function analysis. Information contained in the surface waves is used to constrain the Moho depth between these point measurements.

#### 3.3.1 Constraints on crustal thickness

About half the estimates of the crustal thickness included here come from the compilation of Mooney et al. (2002), and the rest from individual publications. The list of references,

**Table 3.1:** Locations of broad band stations, number of receiver functions used and resulting values for Moho depth.

Code	Latitude	Longitude	N	Moho (km)
DGI	40.318	9.607	19	34
GRI	38.822	16.420	16	43
MGR	40.138	15.553	9	23
SOI	38.073	16.055	24	35
SAOF	43.986	7.553	29	21
RUSF	43.943	5.486	13	33
SMPL	42.094	9.285	32	35

subdivided into different types of data used, can be found in the Appendix A. Crustal thickness beneath a few stations belonging to the temporary MIDSEA and to the permanent TGRS network has been estimated from receiver function analysis following Van der Meijde et al. (2003b). These estimates have also been included in this study and are listed in Tab. 3.1. In addition, since only few Moho depth estimates exist for the eastern Atlantic region and surface wave information is limited owing to a limited number of crossing paths (Fig. 3.2), we force the Moho depth to stay close to 10 km (standard oceanic crust) where the water is deeper than 2000 m and the surface waves do not require otherwise. Uncertainties related to the individual point measurements differ depending on the method used to determine the crustal thickness estimate. Under the assumption of a flat Moho (e.g. Van der Meijde et al., 2003b), crustal thickness data obtained with receiver function analysis have an error around  $\pm 1-2$  km. Uncertainties related to the results of refraction and/or reflection seismology vary depending on the data quality. Moho depth estimates obtained from refraction seismics can have an uncertainty as small as 1.5 km (Bohnhoff et al., 2001). In general, the results of gravity studies have larger errors.

### 3.3.2 Surface waves

For interpolation between the point estimates of the crustal thickness, information contained in broad band  $S$ - and surface waves is used. Seismograms from regional earthquakes recorded at broad band seismic stations in the Mediterranean region (Europe, northern Africa, Middle East countries and islands in the Atlantic Ocean) belonging to different European networks (Swiss National Network, IRIS/IDA, IRIS/USGS, MedNet, Un. Trieste, Géoscope, RéNaSS, TGRS, GEOFON, GRSN, GRF, Un. Stuttgart, GII, Un. Barcelona, Un. Madrid, Inst. Andaluz, Czech National Seismological Network (CZ), NARS, GI\_Budapest, Blacknest) are studied. It is impossible to obtain homogeneous data

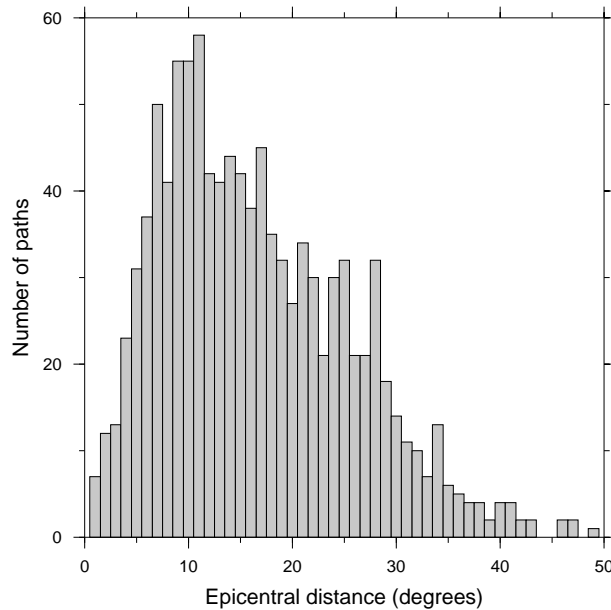


**Figure 3.3:** Distribution of the epicentral distance of wave paths used for waveform fitting.

coverage, given the uneven distribution of seismic stations and events in the Mediterranean region. Moreover, because of its extremely complex crust and upper mantle structure, we needed to use shorter paths than in previous studies (e.g. Zielhuis & Nolet, 1994) to avoid phases distorted by scattered energy. Therefore, we temporarily installed 25 broad band three-component seismic stations during the MIDSEA project (Van der Lee et al., 2001) in regions poorly covered, like the north African coasts and Mediterranean islands. Using the seismograms from these new stations provided us with more and shorter paths than used in previous studies.

We analysed the  $S$ - and surface waves (for a frequency window between 6 mHz and 60-100 mHz) from 235 regional events recorded on 1136 vertical and radial seismograms with a good signal-to-noise ratio. We considered earthquakes with a magnitude between 4.4 and 7.6. The distribution of the epicentral distance is shown in Fig. 3.3. The median path length is  $15^\circ$  and the paths are shorter than  $30^\circ$ , except for the events located in the Atlantic Ocean.

Synthetic seismograms have been calculated using the hypocenter location and origin time provided by the NEIC Preliminary Determination of Epicenters for recent events. For older earthquakes, the source parameters used come from Engdahl et al. (1998). The moment tensor solutions were taken when available from the online Harvard catalogue (e.g. Dziewonski et al., 1994). For smaller regional events we used the solutions computed by Braunmiller et al. (2002). In a few cases we adopted the results from the online MedNet catalogue or those of Thio et al. (1999).

### 3.4 Method

To interpolate between point measurements of Moho depth, we use the Partitioned Waveform Inversion (PWI) method. The results are the map of the Moho discontinuity (EAM02) presented here, together with a 3D upper mantle  $S$ -velocity model for the region discussed separately (Marone et al., 2003a). This joint inversion for Moho depth and  $S$ -velocity structure mutually reduces biases of assumptions for one of these on the results for the other.

The PWI was introduced and applied to a 2D case by Nolet (1990). Originally, only perturbations in the  $S$ -velocity structure were considered, while the effect of variations in Moho depth was included in later calculations by Das & Nolet (1995) using partial derivatives derived by Woodhouse & Wong (1986). For a detailed description of the method in 3D, see Van der Lee & Nolet (1997).

In the first part of PWI, linear constraints on the average  $S$ -velocity structure and Moho depth along each path are determined by non-linear waveform fitting of wave trains composed of fundamental and higher mode surface waves. Particularly sensitive to crustal structure is the high frequency part of the fundamental mode surface wave. To use high frequency waveforms not biased by scattered energy, we have included as many short-path seismograms as possible. The non-linear nature of the waveform fitting procedure requires the use of 1D starting models close to the average  $S$ -velocity structure along each path. For continental paths, we chose models derived from *iasp91* (Kennett & Engdahl, 1991) with different crustal thicknesses, while for paths crossing comparable amount of sea and land, we introduced a water layer (2 km or 4 km thick for waves travelling through the Mediterranean region or the Atlantic Ocean, respectively) to simulate the mixed character of the crossed region.

In the second part of the PWI, constraints obtained from the waveform fitting and independent point estimates of the Moho depth are jointly inverted for  $S$ -velocity and crustal thickness. The linear constraints obtained for the Mediterranean region from individual seismogram fits are characterized by a crust thinner than the 35 km of *iasp91* and show lower  $S$ -velocities in the uppermost mantle. Consequently, a reference model for the 3D inversion similar to *iasp91* has been chosen, but with a crustal thickness modified to 30 km and lower  $S$ -velocities in the uppermost 200 km. As demonstrated in Marone et al. (2003a), however the obtained solution is stable and is independent of the adopted starting model. The  $S$ -velocity is parameterized as coefficients of a Cartesian grid of nodes, while for the Moho depth a triangular grid of nodes is adopted on a spherical shell at the Moho depth of the background model (Van der Lee & Nolet, 1997). The distance between the nodes of the triangular grid is compatible with the inter-knot spacing in the Cartesian grid and is 97 km on average. Since the inversion problem is mixed determined, it has been solved using a damped least-squares inversion method. The value of the damping parameter ( $\lambda = 1$ ) has been chosen to balance variance reduction and model norm. Moreover, given the characteristics of the surface waves, it has been required that the solution

is smooth. Since the distance between the grid nodes in the vertical direction is 60 km, the resolution for the crustal velocity structure is limited. Therefore, the  $S$ -velocity model obtained for the uppermost part of the model represents only an average for the crustal and sub-Moho velocities and will not be interpreted. It has been inverted for it to absorb the effects of crustal velocity structure on the waveform data. The effects of Moho depth on waveforms are much larger than those of distributed velocities within and immediately below the crust. For more details on the 3D inversion see Marone et al. (2003a).

A different weight is assigned to each independent point constraint according to its estimated uncertainty (see section 3.3.1). The point constraints resulting from refraction and/or reflection profiling and some of the receiver function analyses are more strongly weighted since their estimated error is smaller than that of other crustal thickness estimates. To choose the relative weights of the point constraints and the Rayleigh wave fits, we opted for a balance between smoothed Moho topography and exact match between point constraints and resulting crustal thickness values. For the chosen model, most point constraints are met by the Moho map within their double standard deviation (Fig. 3.4), while the Moho topography remains smooth. The discrepancies falling outside the double standard deviation interval are related to point measurements in regions where a strong gradient in the Moho topography can be expected (e.g. Calabrian and Hellenic arcs). The obtained Moho depth model has been forced to be smooth. If the weight of the point constraints is increased and they are forced to be matched within their single standard deviation, the obtained model shows strong gradients and small size anomalies.

Fig. 3.4(f) shows how the values observed in EAM02 (Fig. 3.5) deviate from the artificially imposed point constraints in the Atlantic Ocean (see section 3.3.1). The distribution of the differences is shifted towards negative values and the maximum is observed at -5 km. This indicates that the surface waves travelling through the eastern Atlantic region require on average a 5 km thicker crust than the imposed standard oceanic crust of 6 km.

### 3.5 Uncertainties estimation

Uncertainties in the obtained Moho depth values arise from different sources. First, the resolving power of a seismogram for the average earth structure along its path is controlled by the Fresnel zone. If natural trade-offs between model parameters (e.g. crustal velocity and Moho depth) are not reduced by introducing additional constraints, the obtained velocity and crustal structure along every single path as well as the final 3D image can be blurred. Errors in the source parameters and excitation factors, as well as in modeling assumptions (neglect of scattering, multipathing and mode-coupling) and in the approximations made in the non-linear waveform fitting method also limit the resolving power of the data. Das & Nolet (1995) showed that for synthetic and real data with a very good signal-to-noise ratio, the Moho can be resolved within a kilometer, if frequencies as high as 0.125 Hz are fitted. Due to the complexity of the Mediterranean region and limited signal-to-noise ratio (mainly waveforms of moderate earthquakes have been used), in this

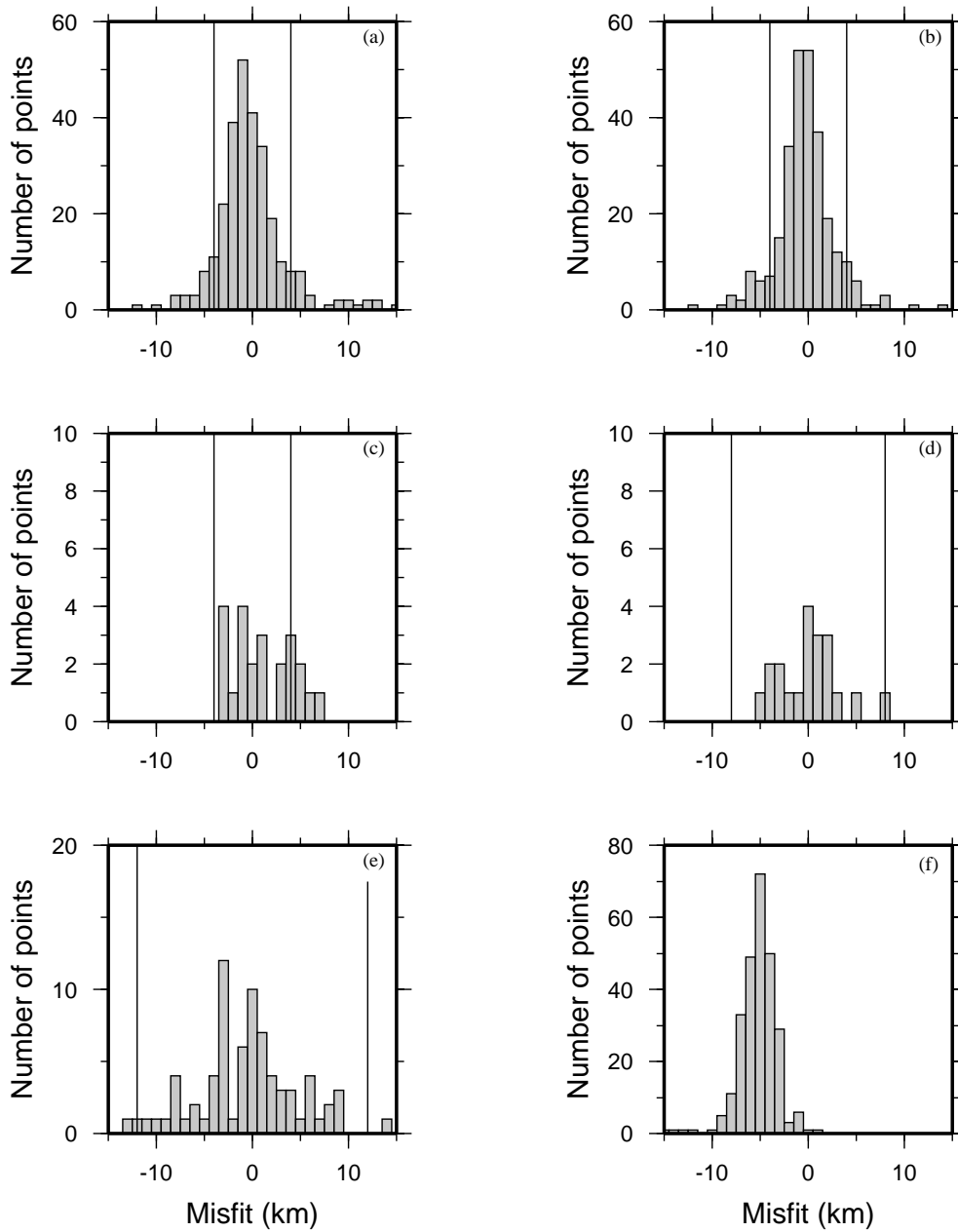


**Figure 3.4:** Distribution of the deviation of the previous crustal thickness observations from the values observed in EAM02 (Fig. 3.5). The 95% confidence interval is represented by the two vertical lines. ((a) Dataset of Mooney et al. (2002), (b) Refraction and reflection profiles, (c) Receiver function study of Van der Meijde et al. (2003b), (d) Other receiver function studies, (e) Gravity studies and (f) A priori constraints on the crustal thickness in the Atlantic Ocean).

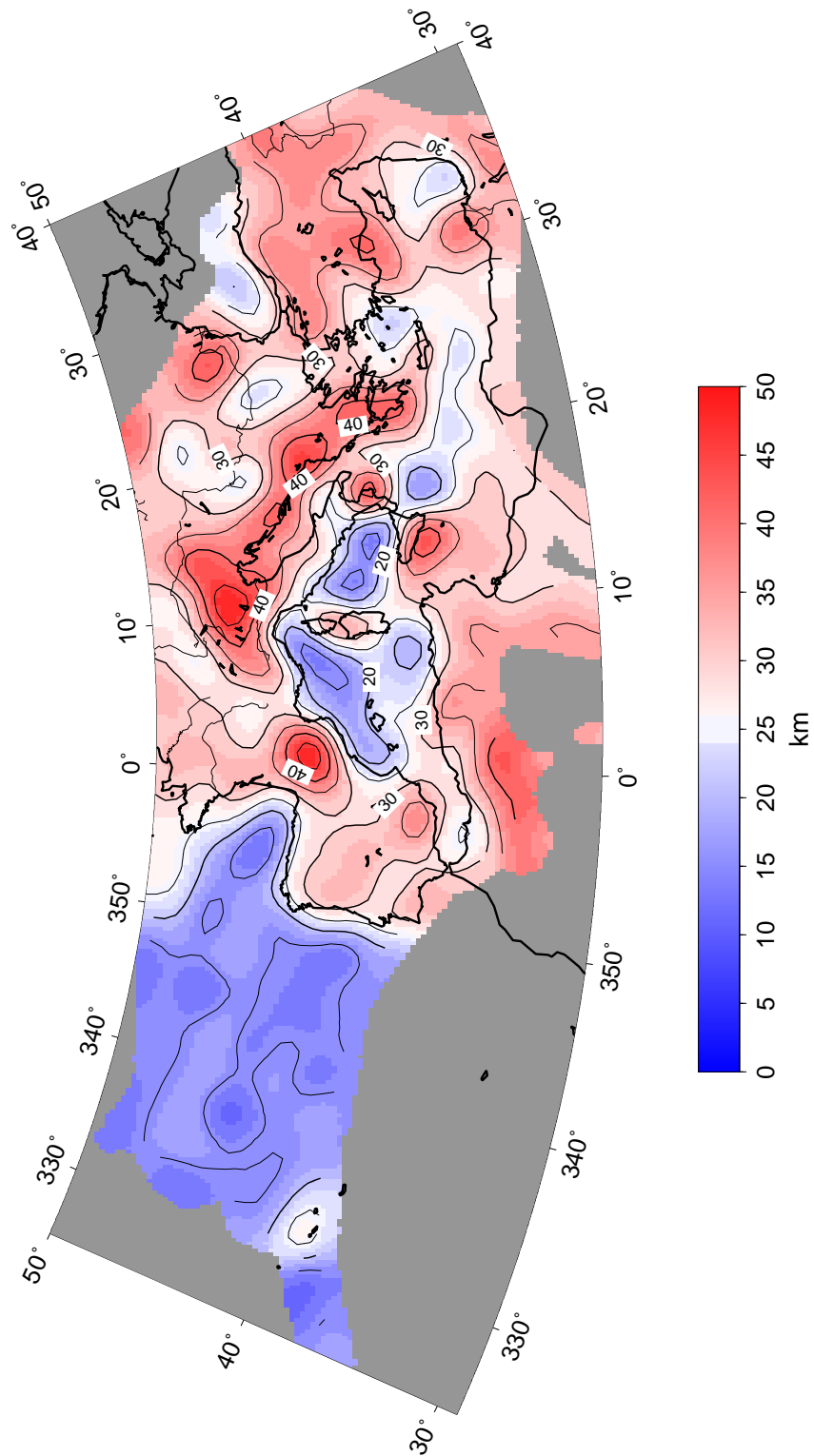


**Figure 3.5:** Map of Moho depth (EAM02) obtained in the 3D inversion.

study it was hardly possible to fit frequencies higher than 0.08 Hz. The expected uncertainty related to the average crustal thickness along each path is therefore higher than the ideal case shown in Das & Nolet (1995).

In the joint 3D inversion of linear constraints provided by the waveform fitting and additional point constraints, further uncertainties are involved: errors in previous estimates of crustal thickness and the variable resolving power of surface waves due to inhomogeneous great circle ray path coverage and the modes different sensitivity to different parts of the crust and upper mantle. In addition, the smoothness constraint is also responsible for averaging the Moho topography towards a mean value which leads to underestimating the small-scale Moho topography perturbations. Owing to different error sources and the barely quantifiable propagation of uncertainties in the inversion, a formal error estimate is impossible for the Moho depth values obtained here. Nevertheless, assessing the anomaly size and amplitude that can be recovered in the 3D inversion as well as the spatially variable resolving power of the data is important for interpreting and using EAM02. For this reason resolution tests with synthetic anomalies have been performed.

In Figs. 3.6 and 3.7 two examples are shown: one with large anomalies ( $5^\circ$ ) and one with small ( $3^\circ$ ). As expected, large features are better resolved than small ones. The shape of Moho topography perturbations with an average size of 500 km are well resolved throughout the studied region. The anomaly amplitude is almost completely recovered in central-southern Europe, the central-western Mediterranean Sea and the Atlantic Ocean. In the remaining areas it is partly underestimated (Fig. 3.6). For features as small as  $\sim 300$  km, the best resolving power is achieved for central-western Europe and the Mediterranean Basin: the region with the best path coverage and most point estimates of crustal thickness. In these regions we recovered 83% of the amplitude of the Moho perturbation, for other areas the anomaly amplitudes are underestimated. Although the surface wave path coverage is optimal in eastern Europe, small-scale features of the synthetic input model are not well recovered (Fig. 3.7) owing to few point measurements of the Moho depth and insufficient high frequency fundamental mode surface waves generated by Romania's intermediate to deep earthquakes.

To have an idea of the resolving power for gross-scale features, we performed an additional resolution test with a realistic input structure: 10 km, 20 km and 35 km Moho depth beneath the Atlantic Ocean, the Mediterranean Sea and Europe, respectively (Fig. 3.8). For regions with good path coverage and enough point constraints, the resolution is very good and the amplitude anomaly completely recovered (e.g. in the western Mediterranean). If the number of point constraints for crustal thickness is limited, we observed underestimation of the Moho topography perturbations up to 4 km for regions constrained only by surface wave data.

Since a trade-off between crustal velocity and thickness exists, insufficient control of the crustal  $S$ -velocity structure could be wrongly mapped into the Moho topography. An inversion attempt, with additional independent constraints on upper crustal  $S$ -velocities according to the sediment information from Laske & Masters (1997), shows that in re-



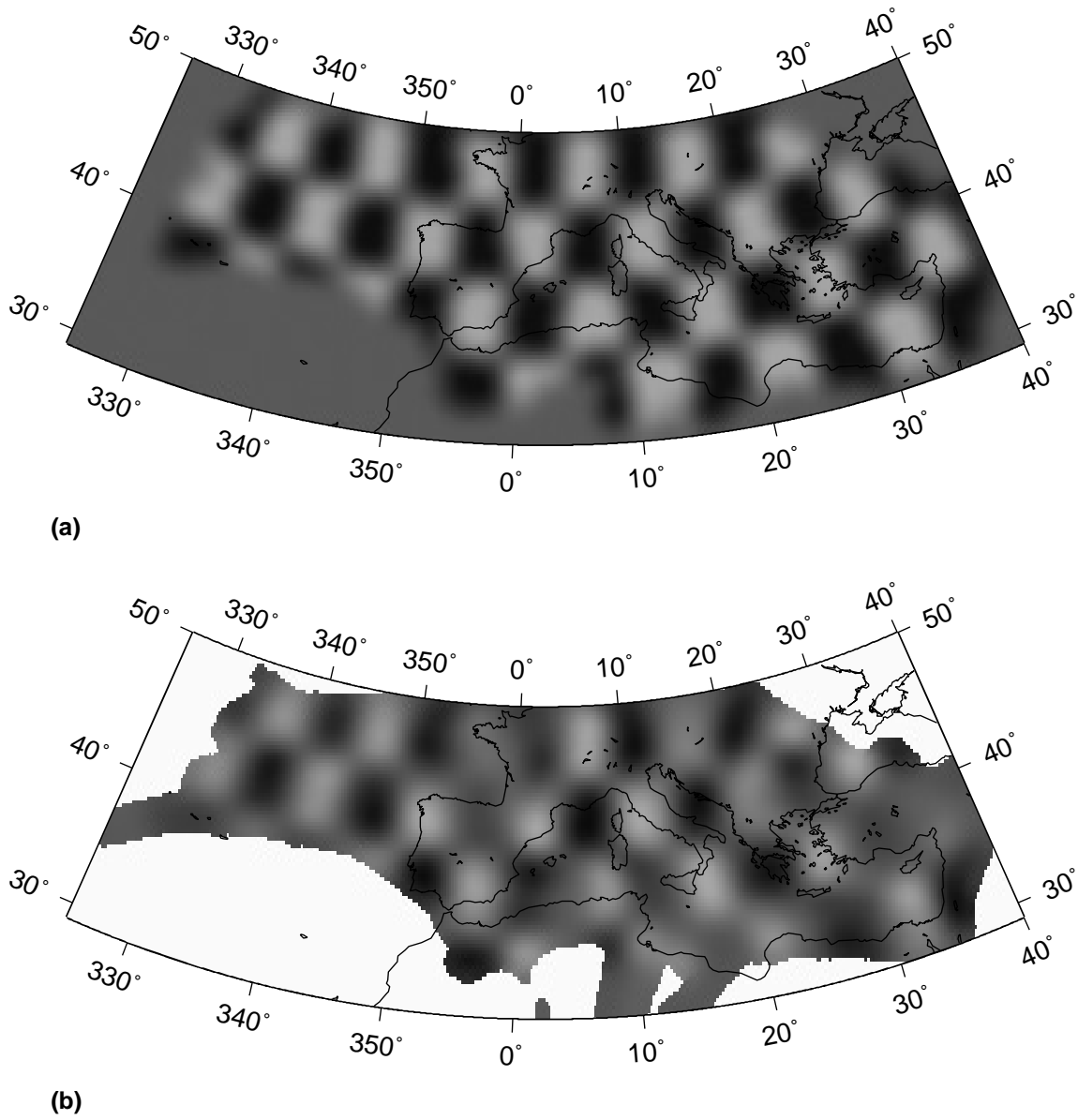


**Figure 3.6:** Checkerboard resolution test with  $5^\circ$  anomaly size: (a) Input model, (b) Retrieved structure.

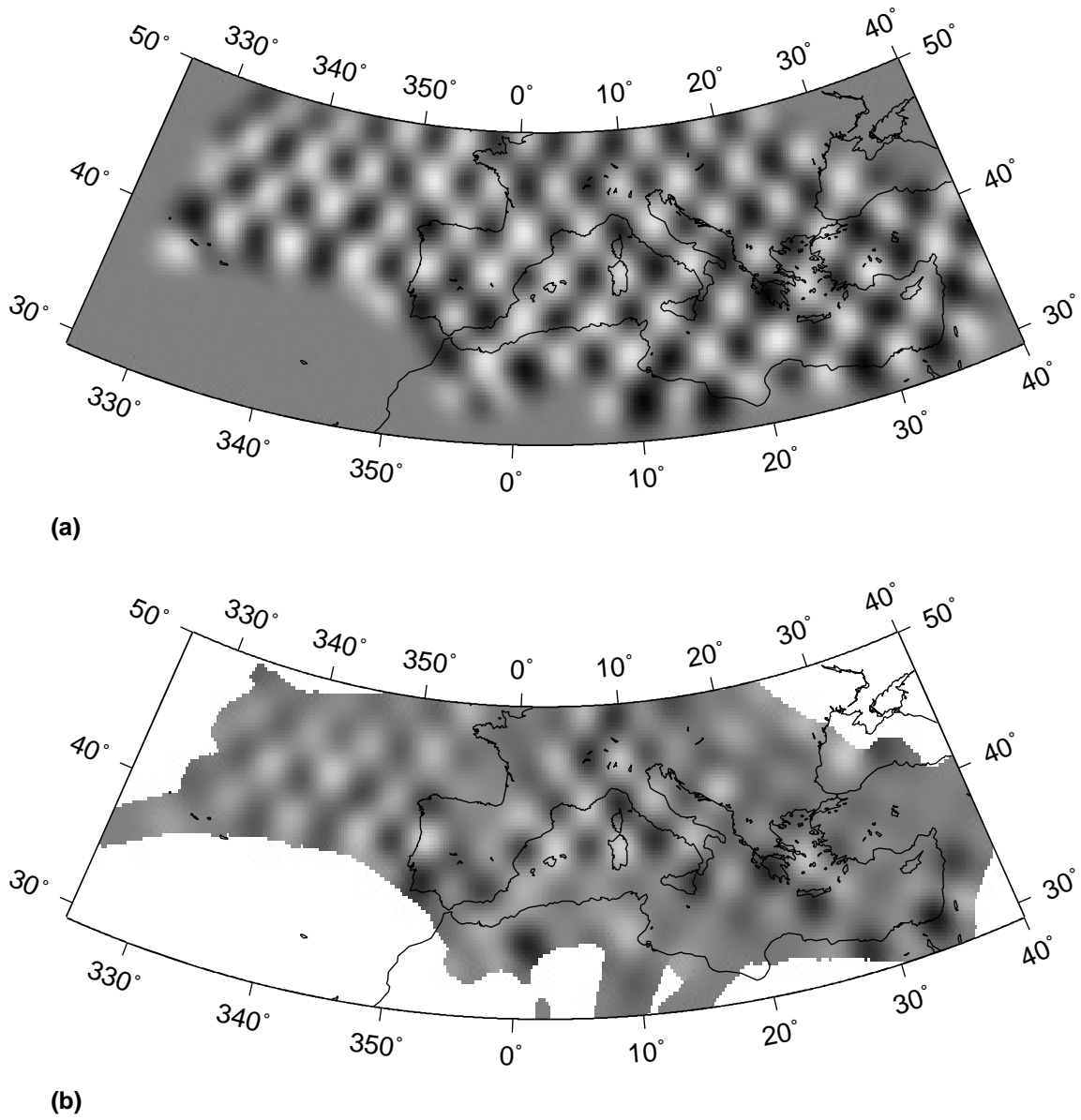


**Figure 3.7:** Checkerboard resolution test with  $3^\circ$  anomaly size: (a) Input model, (b) Retrieved structure.

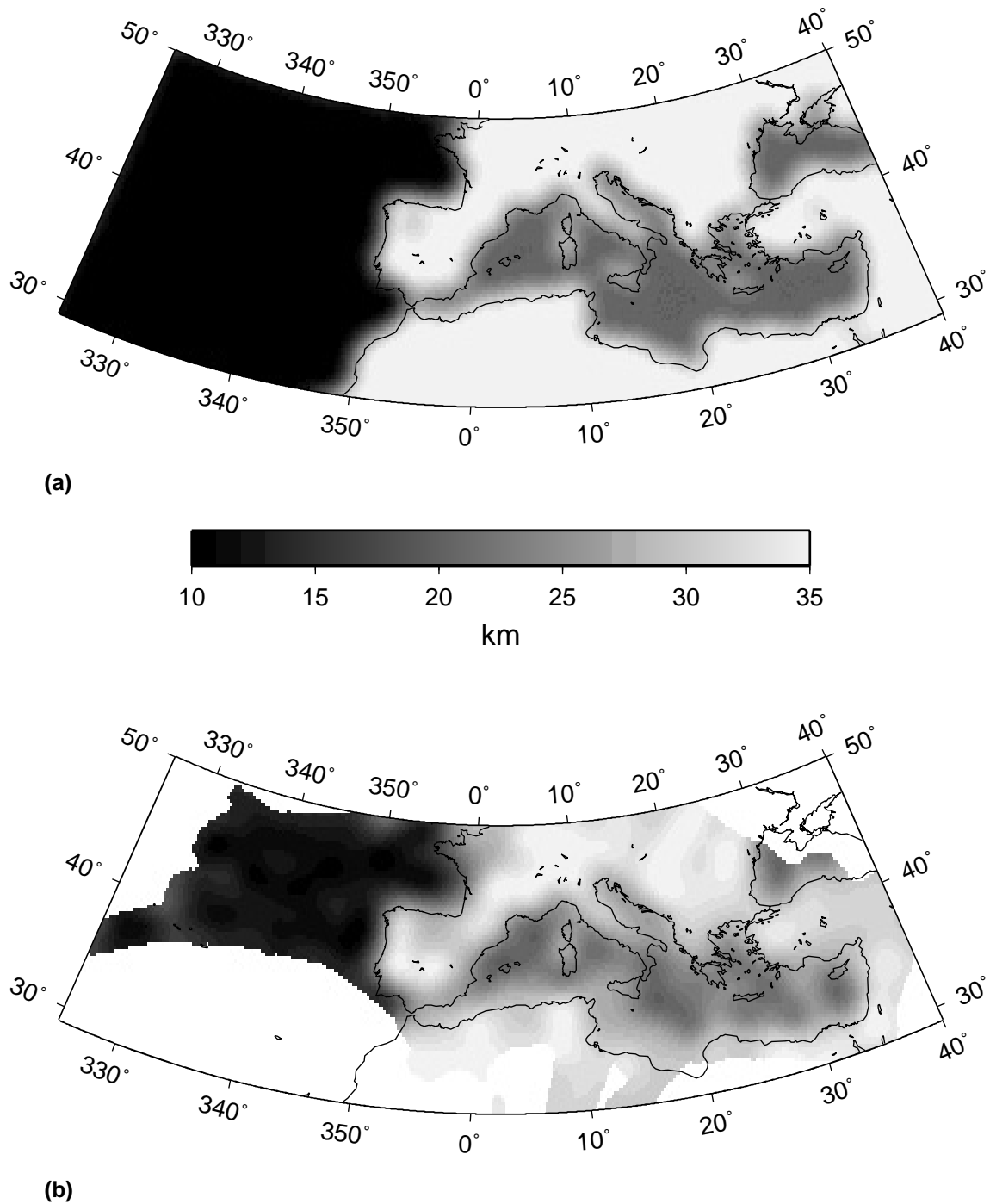


**Figure 3.8:** Resolution test with realistic input structure (10 km, 20 km and 35 km Moho depth beneath the Atlantic Ocean, the Mediterranean Sea and Europe respectively): (a) Input model, (b) Retrieved structure.

gions with an anomalously low average crustal velocity due to thick sedimentary deposits (up to 15 km), crustal thickness can be overestimated by up to 8 km. In areas with a standard upper crust, variations in the Moho depth related to whether or not sediments are included fall within the uncertainties. Therefore, and because of incomplete and imprecise sediment thickness and velocity information, we decided not to correct for this effect. No constraints on crustal velocity have been included in the joint 3D inversion. However, overestimating crustal thickness due to particularly thick sedimentary layers in the Mediterranean region is expected only in limited areas (eastern Mediterranean and Adriatic Sea). For the remaining region the sedimentary coverage is not thick enough to bias the results significantly.

## 3.6 Results and discussion

The obtained Moho map for the Eurasia-Africa plate boundary region (EAM02) is shown in Fig. 3.5. Depth to the Moho in the area varies from less than 15 km beneath the Atlantic Ocean and in the Algero-Provençal Basin to over 43 km beneath the Alps. The spatially averaged value for the crust-mantle boundary depth is 28 km.

Compared to the existing Moho map for the region by Meissner et al. (1987), we extended the results to the southern Mediterranean Basin, northern Africa and the Atlantic Ocean.

### 3.6.1 Mediterranean Sea

The Mediterranean Sea shows a strongly heterogeneous character. In the western part, beneath the Ligurian Sea and the Algero-Provençal Basin, a shallow Moho ( $< 20$  km) has been imaged. The observed thin and on average fast crust, together with the low  $S$ -velocities observed in the uppermost mantle (Marone et al., 2003a) and the high heat flow measured (Burrus & Foucher, 1986), all support the idea of oceanic crust present among the predominantly extended continental crust, at least in limited locations (e.g. offshore Provence). The region's imaged thin crust could be the result of extensional processes at the back of the retreating NW dipping subducting oceanic lithospheric slab between  $\sim 30 - 22$  Ma (Faccenna et al., 2001). Oceanic crust could have been emplaced during the simultaneous  $25-30^\circ$  counterclockwise drifting of the Sardinia-Corsica block (Burrus, 1984).

The westernmost part of the Mediterranean Basin or Alboran Sea, squeezed in between the Betics in the north, the Rif in the east and the Atlas Mountain Range in the south, has been locally affected by extensional processes since the Early Miocene (e.g. Platt & Vissers, 1989; Seber et al., 1996), even though deformation of the overall region is dominated by the converging and colliding African and Eurasian continents. While the Moho discontinuity beneath the mountain belts in southern Spain and northern Africa is found at a depth of 35 to over 40 km, the Alboran Sea has a much shallower Moho at 25 km. According to resolution tests (Fig. 3.7), a feature as small as the Alboran Sea can be re-

solved by our dataset. However, the Moho depths obtained for this region are possibly damped towards a mean value: in reality the crust-mantle boundary is deeper beneath the arcuate mountain belt and shallower in the center beneath the Alboran Sea than shown in Fig. 3.5.

The central Mediterranean Basin can be divided into two regions following the bathymetry (Fig. 3.1), the Moho topography (Fig. 3.5) and the uppermost mantle *S*-velocity structure (Marone et al., 2003a). North of the Malta escarpment, where the deep basins are, a shallow Moho is observed. Beneath the Ionian Basin the crust-mantle discontinuity is shallower than 20 km, while eastward (below the Sirte Basin) it is found at 23 km. These results support the interpretation of the deep central Mediterranean basins as relicts of Mesozoic oceanic crust covered by 6-8 km thick sedimentary layers (De Voogd et al., 1992). To the south, offshore Libya, the Moho is present at 30 km depth. This suggests that the region could be an extension of the northern African margin beneath the Mediterranean Sea, an idea supported by its shallow bathymetry. Such a division of the central Mediterranean Sea into two parts is also observed in the upper mantle structure, with a fast northern part, possibly representing oceanic lithosphere, while average velocities are present to the south (Marone et al., 2003a).

The eastern Mediterranean shows the Moho at a depth of 30 km on average. A shallowing of the crust-mantle boundary (23 km) has been mapped beneath the Levantine Sea, while a deepening ( $> 35$  km) is observed at the Nile's mouth, where sediments transported by the river have accumulated. Reflection and refraction seismic profiling, gravimetric and magnetic studies have been performed in the region. However, the origin of this part of the Mediterranean Sea as well as the nature of its crust are still debated. For the easternmost Mediterranean Basin (Levantine Sea) particularly, two end-member hypotheses exist. The first one suggests that the crust, of oceanic nature, formed during Mesozoic periods of rifting (eg. Makris et al., 1983; Dercourt et al., 1986; Ben-Avraham et al., 2002). The second hypothesis postulates that a Precambrian continental basement with terranes of accreted Precambrian oceanic crust underlies the entire eastern Mediterranean (Hirsch et al., 1994). The original continental crust could have thinned through a change of its physical properties due to the accumulation of an up to 14-km-thick pile of mainly Triassic and Jurassic sedimentary rocks as mapped in the region (Makris et al., 1983; Hirsch et al., 1994; Knipper & Sharaskin, 1994). In spite of differences in the mechanism of crust formation and of crustal nature (continental or oceanic), both theories agree on the presence of thin crust covered by a thick sedimentary pile. Even if resolution in this part of the studied region is limited by inhomogeneous data coverage, our results support the existence of thin crust, especially in the Levantine Basin, where a shallower Moho is observed compared to surrounding regions. Moreover, during the waveform fitting of the single seismograms in the first part of the PWI, the linear constraints obtained for this region indicate anomalously low velocities in the crust, consistent with a thick sedimentary layer.

### 3.6.2 Eastern Atlantic Ocean

The eastern Atlantic Ocean, the region between the Mid-Atlantic Ridge and western Europe, is characterized by a relatively homogeneous structure, with the Moho at a depth of 15 km (with an average 4-4.5 km water layer, a crustal thickness of 10.5-11 km). Our results show a crust at least 4 km thicker than values obtained from seismic refraction and reflection profiles (e.g. Fowler & Keen, 1979; Whitmarsh et al., 1982; Ginzburg et al., 1985), and a difference of about 2.5 km compared to results from rare element inversions of melt distribution in the mantle source region (White et al., 1992). The Moho is deepening to 27 km underneath the Azores archipelago. The origin of the thicker crust here could be an increased melt production due to the interaction of the spreading ridge and a possible mantle plume (White et al., 1992).

As can be seen in Fig. 3.1, the seafloor of the eastern Atlantic Ocean shows a perturbed relief. These heterogeneities could have formed at the Mid-Atlantic Ridge after magmatic and amagmatic periods, which alternate over a short temporal scale ( $\sim 100$  ka) and are characteristic of low spreading ridges (Rommevaux et al., 1994; Canales et al., 2000). Canales et al. (2000) also pointed out the extremely variable thickness of the crust formed at such slow spreading ridges: they measured  $\geq 2.2$  km thickness variations over horizontal distances of  $\sim 5$  km. During periods of high magma supply, a crust thicker than standard oceanic crust could have been created. The study of rocks dredged along slow spreading ocean ridges suggests lateral variability of the structure of the oceanic crust along the ridge, as a consequence of non-uniform flow of melt out of the mantle and punctual ocean ridge magmatism (Dick, 1989). Complex crustal thickness variability results also from 3D numerical models of convection within the partially molten mantle beneath the ridge axis (Rabinowicz & Briais, 2002). Moreover, underplated bodies and fragments of subcontinental lithospheric mantle residing shallowly in the oceanic mantle have been imaged with wide-angle seismic reflection techniques (Jacob et al., 1995) and postulated from  $^{187}\text{Os}/^{188}\text{Os}$  ratio measured in basalts (Shirey et al., 1987; Widom & Shirey, 1996). Together with such fragments, crustal pieces could also have detached from continental edges during the opening of the North Atlantic Basin and now lie within younger oceanic crust. Along with a mantle plume, these fragments of continental crust can explain the thicker crust observed in the Azores archipelago.

The serpentinization of the sub-Moho mantle at the Mid-Atlantic ridge could also contribute to the imaging of the anomalously thick oceanic crust in our model for the eastern Atlantic Ocean. It is likely that open fissures characteristic of slow spreading ridges and non-constructive areas of ridge axes provide a path for seawater circulation which easily penetrates the upper mantle lying at shallow levels (e.g. Hébert et al., 1990; Blackman et al., 1998). Serpentinization of mantle rocks strongly decreases their density from  $3.2 \text{ g/cm}^3$  for mantle rocks to a density of  $2.5 \text{ g/cm}^3$  for pure serpentine (e.g. Miller & Christensen, 1995; Blackman et al., 1998; Früh-Green et al., 2001), as well as their  $S$ -velocity. In fact, the shear-wave velocity of serpentinized mantle rocks is close to crustal

*S*-velocities. Thus, rock serpentization in the uppermost mantle could create a low *S*-velocity layer just beneath the Moho, reducing the velocity contrast at the crust-mantle discontinuity and creating a stronger velocity gradient between the serpentized sub-Moho mantle and the unaltered lithospheric mantle. Possibly this velocity discontinuity has been imaged and interpreted as the Moho, thus causing us to overestimate the oceanic crustal thickness. Modeling single waveforms of *S*- and surface waves travelling through the eastern Atlantic Ocean supports this interpretation. In fact, if a Moho at 10 km depth is chosen *a priori*, the surface waves require a 10-15 km thick sub-Moho layer characterized by *S*-velocities as low as 4.15 km/s. Moreover, a 1D path-average velocity model characterized by a 5 km thick sub-Moho layer with extremely low *S*-velocities ( $\sim 3.3$  km/s) is also consistent with the observed waveforms. *S*-velocities as low as 3.3 km/s would suggest a degree of serpentization as high as 50% (Christensen, 1966). Serpentized uppermost oceanic mantle seems to be required in subduction zones, where dehydration could provide enough energy for unbending the slab (e.g. Seno & Yamanaka, 1996; Peacock, 2001). Dehydration embrittlement could be the cause of intermediate depth earthquakes occurring at mid-plate depths in the subducting slab. However, where serpentization is taking place is still a matter of debate: Peacock (2001) suggests that serpentization may occur in the trench-outer rise region, where faulting may promote infiltration of seawater several tens of kilometers into the oceanic lithosphere. In contrast Seno & Yamanaka (1996) propose that the hydration of the uppermost oceanic mantle could occur when the oceanic plate passes over plumes or superplumes. Here we show evidence that in the eastern Atlantic Ocean the sub-Moho mantle could be partially serpentized so that hydration could partly occur at the Mid-Atlantic ridge. Synthetic resolution tests preclude that the wave path coverage has contaminated the imaged structure of the Atlantic region with continental characteristics (Fig. 3.2).

### 3.6.3 Northern Africa

After installation of broad band seismic stations along the northern African coast during the MIDSEA project (Van der Lee et al., 2001), it was possible to increase data availability significantly and consequently resolution, especially for the northernmost margin of Africa discussed here. However, the structure south of the margin is biased by smearing along the main path direction.

EAM02 shows on average the Moho discontinuity at 30 km depth beneath regions such as northern Egypt and northern Libya which have not experienced important tectonic episodes since the Paleocene (rifting phase in the Sirte Basin). A thickening of the crust is observed at the Nile delta, where thick sediments are present (Tawadros, 2001). However, the western part of the African continent is characterized by a rapid change from a relatively deep Moho (down to 42 km) below the Atlas Mountain Range to the thin crust of the southwestern Mediterranean Sea ( $< 20$  km). These features are a consequence of past tectonic movements, such as subduction along northern Algeria (Dercourt et al.,

1986). The tectonic activity of this area, still nowadays, is documented by seismicity (e.g. Buforn et al., 1995).

### 3.6.4 European continent

The main features observed for continental Europe (Fig. 3.5) are correlated with surface topography (Fig. 3.1). In fact, EAM02 shows crustal roots beneath mountain belts such as the Alps, the Dinarides, the Hellenides, the Pyrenees and the Carpathians, where the Moho discontinuity is deeper than 40 km. A deep crust-mantle boundary ( $> 35$  km) is also found beneath Turkey. A shallow Moho ( $< 30$  km) is observed in relation with extensional settings beneath the Pannonian Basin, the Black Sea and along the Central European Rift. A similar feature is present beneath Bulgaria. We compared our results for Europe with Meissner's (1987) map for the Moho depth which he obtained compiling several deep seismic and extensive reflection/refraction profiles. We observe strong similarities in the long wavelength character.

Comparing well are the results for Italy, where a complex structure can be expected because of the interacting crust of the Adria microcontinent and the European plate. Beneath Italy and the Corsica-Sardinia block the Moho discontinuity is found on average at 30 km depth. We also confirm that the crust of the Adria microplate is continental with the Moho at a depth of 30-35 km, as found by Meissner et al. (1987) and Morelli (1998). The seas west of Italy show a shallower Moho than inferred by Meissner et al. (1987). In the Ligurian Sea the crust-mantle boundary is found at 20 km depth. This value agrees with the minimum Moho depth of 16 km for this region proposed by Morelli (1998). Probably the higher values found by Meissner et al. (1987) arise from interpolation due to lack of data. For the Tyrrhenian Sea as well, a thin and stretched crust has been found by several authors like Calcagnile & Scarpa (1985) from regional dispersion of seismic surface waves and Locardi & Nicolich (1988) from deep seismic profiles and petrological studies. In EAM02 (Fig. 3.5) we also observe a shallow crust-mantle boundary beneath the Tyrrhenian Sea, confirming a stretched crust. However, the results in this area are constrained mainly by estimates of crustal thickness obtained in refraction and reflection profiles. The surface waves would prefer a thicker crust, probably because the recorded signals of deep earthquakes occurring beneath the Calabrian arc contain no fundamental-mode frequencies high enough to constrain the crustal thickness significantly. As a result, the value of the Moho depth stays close to the 30 km of the background model. The shallow Moho discontinuity found beneath the Tyrrhenian Sea has been set in relation with the extensional back-arc basin tectonics characterizing this area (e.g. Faccenna et al., 2001).

In eastern Europe more differences emerge compared to the Moho map by Meissner et al. (1987). First of all, beneath the Carpathian arc we find a deepening of the Moho to a maximum of 40 km along a NW-SE striking feature. The NW-SE trending structure with thickened crust that Meissner et al. (1987) found was narrower than what we observe. This difference is due to the smoothing effect of the surface waves. Our results agree with val-



ues obtained from refraction seismic profiles (Hauser et al., 2001), showing an increased crustal thickness under the Carpathians. To the south, in Bulgaria, EAM02 (Fig. 3.5) shows the Moho at a depth of 25-27 km. The crust of this area is poorly known and only a few studies have been carried out in the region. Several authors (Dachev & Volvovsky, 1985; Babuška & Plomerová, 1987; Shanov et al., 1992) suggest a quite complex crustal structure, with a deep Moho in the south, possibly related to a paleosubduction (Shanov et al., 1992) and crustal thinning in the northern-central part related to graben formation and a shallow asthenosphere. The zone of thin crust we imaged in Bulgaria is more elongated in the N-S direction compared to the studies mentioned above. The thickened crust in the southern part proposed by the authors above is possibly a small size perturbation which can not be efficiently detected by the surface waves. However, since enough seismic waves travel across this area, we believe that this region is characterized on average by a thin crust.

Greece is characterized by complex tectonics, with compressional processes in the outer zone and extension in the back-arc basin area (Dercourt et al., 1986) as reflected in its crustal structure (Fig. 3.5). In fact, we find the Moho deeper than 40 km beneath the Greek mainland and the Peloponnesus. The crust-mantle boundary beneath Crete is observed on average at 30 km. Moving from the collision zone to the back-arc basin (southern Aegean Sea), we observe a shallowing of the Moho to a minimum of 20 km. In the northern Aegean Sea the average Moho depth is 30 km. Our results agree with the Moho map of Makris (1985) obtained by interpolating refraction and reflection seismic data with information from gravity data. The zone of thin crust we image in the southern Aegean Sea is more elongated in an E-W direction, reaching the coasts of Turkey. In Makris' (1985) map this feature is limited to the region north of Crete, but his results on the eastern Aegean Sea are constrained by gravity data only. Similar features are also found in a smaller-scale study presented by Karagianni et al. (2002).

### 3.7 Isostatic compensation

To assess Airy isostatic compensation in the Mediterranean region, the obtained Moho depth model (Fig. 3.5) has been compared with a Moho depth model computed assuming isostatic equilibrium. For this purpose, a synthetic crustal model has been constructed. In particular, detailed information about sedimentary deposits as well as appropriate upper, middle and lower crustal densities at each single node on a  $0.5^\circ \times 0.5^\circ$  grid have been included according to the compilation of Laske & Masters (1997) and Bassin et al. (2000). The thickness of the sedimentary package and the ratio between the three crustal layers have been fixed at the values proposed by Laske & Masters (1997) and Bassin et al. (2000). The thicknesses of the single crustal units have been scaled according to the total crustal thickness in isostatic equilibrium. To obtain in the isostatic compensated model Moho depth variations of the same wavelength as in the observed (Fig. 3.5), the topography of the ETOPO5 dataset (National Geophysical Data Center, 1988) has been

smoothed.

In a first step (Fig. 3.9(a)), Moho depth has been computed considering isostatic compensation only for the crust and assuming a constant density for the uppermost mantle ( $\rho_{mantle} = 3.33 \text{ g/cm}^3$ ). The continental regions are characterized by residuals smaller than 5 km: the difference between EAM02 (Fig. 3.5) and the Moho topography for an isostatically compensated crust is less than 5 km. Considering the uncertainties in estimating the Moho depth (see section 3.5) and in the assumed densities, we conclude that the crust for the studied continental region is close to an isostatic equilibrium. The Mediterranean Basin is showing strong positive residuals compared to the continental regions, suggesting that either sub-Moho lithospheric densities are higher and/or crustal thickness has been overestimated. The Atlantic Ocean is also characterized mainly by positive residuals, possibly indicating that we underestimated the uppermost mantle density for an oceanic region.

In a second step, to include the effect of the lithosphere, we chose a compensation depth at 60 km and computed uppermost mantle densities, converting the  $S$ -velocities obtained in Marone et al. (2003a) according to a velocity-density-depth relationship provided by Cammarano et al. (2002). Also in this case, the observed residuals (Fig. 3.9(b)) for the continental region are smaller than 5 km almost everywhere, confirming isostatic equilibrium. In the Atlantic Ocean the observed and computed Moho topography differs less than in the previous case, which included only the crust. This confirms the necessity of considering the lithosphere with an appropriate oceanic density in isostatic computation. Considering that owing to a mainly E-W paths direction in the eastern Atlantic Ocean (Fig. 3.2), the obtained Moho topography has been averaged out and that the age dependence of the oceanic lithospheric density has not been considered, we conclude that isostatic compensation reigns at 60 km depth beneath this region. Beneath the Bay of Biscay negative residuals are found. This anomaly, not present in Fig. 3.9(a), correlates with an anomalous high  $S$ -velocity body in the uppermost mantle (Marone et al., 2003a). The over 5 km difference between the observed and computed Moho depths could possibly arise from overestimating the uppermost mantle densities. In fact, granulites representing at least partly, an Archaean crust with granulite facies metamorphism have been found in the Bay of Biscay (Guerrot et al., 1989). The Archaean age of the Bay of Biscay rocks compares to that of the west African craton, suggesting that the west European plate belonged to west Africa during the late Proterozoic (Guerrot et al., 1989). Although cratonic material shows high  $S$ -velocities, it is characterized by lower densities than expected due to depletion and leads here to overestimating of the lithospheric density because of the constant velocity-density-depth relationship used. Decreased residual values with the inclusion of the lithosphere are also observed for the central Mediterranean (between southern Italy and Libya), while residuals over 5 km are still present in the eastern Mediterranean. In this latter region isostatic compensation would require higher densities in the uppermost mantle. Therefore, according to the velocity-density-depth relationship of Cammarano et al. (2002), we expect higher  $S$ -velocities, which are, however, absent in Marone et al. (2003a). Such large discrepancies between observed and

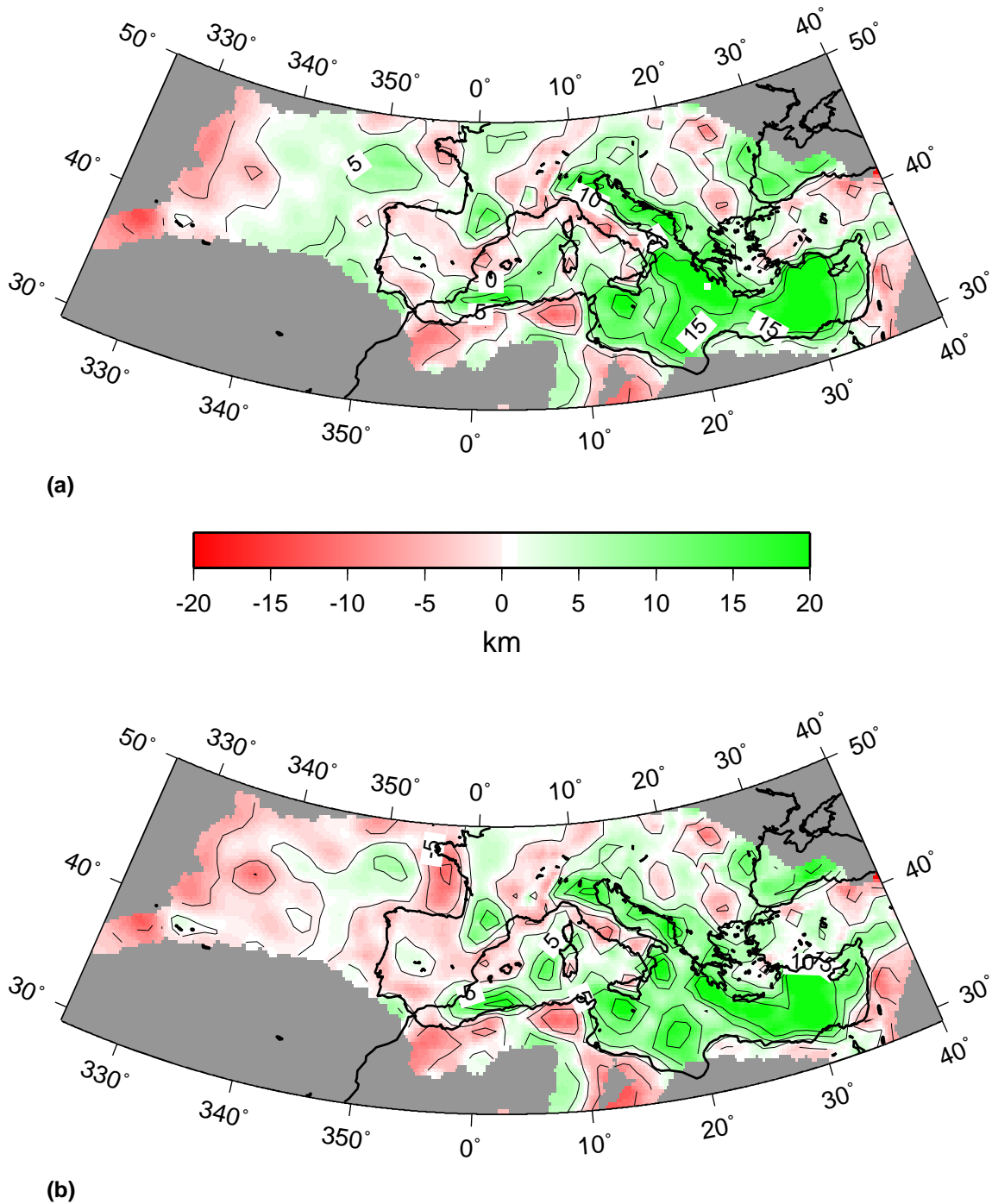


**Figure 3.9:** Moho depth residuals computed by subtracting the Moho depth calculated assuming isostatic equilibrium from the obtained Moho depth: (a) assuming isostatic compensation only for the crust and a constant density for the uppermost mantle, (b) assuming a compensation depth of 60 km and using uppermost mantle densities derived from the S-velocity model of Marone et al. (2003a).

computed Moho depths could arise from overestimating crustal thickness in this region. In fact the highest residuals correlate with the area having thickest crust offshore the Nile mouth. As pointed out in section 3.5, synthetic tests show that a trade-off exists between crustal velocity and thickness. Overestimating crustal velocity is responsible for overestimating the Moho depth. This effect is particularly important in the eastern Mediterranean Basin, where more than 10 km thick sediment deposits are present and crustal thickness could be overestimated by up to 8 km.

### 3.8 Conclusions

We are first to map Moho depth (EAM02) covering the whole Mediterranean region with reliable results also for the southern and eastern Mediterranean Basin and the northern African coasts, regions only occasionally considered in previous studies on the Mediterranean Basin. Information contained in surface waves has been used to interpolate between existing point estimates of crustal thickness.

The heterogeneous crust of the Mediterranean Sea confirms the complex evolution of this plate boundary region. In the west, the Moho discontinuity has been observed as shallow as 15-20 km. This extensively stretched and partly oceanic crust may have formed from extension in the back-arc of the retreating Calabrian slab. In contrast, the eastern Mediterranean region is characterized by 25-30 km thick crust on average. It is interpreted either as Mesozoic oceanic or thinned Precambrian continental crust covered by a thick pile of Mesozoic sedimentary rocks.

Below the eastern North Atlantic Ocean our results show a crust up to 5 km thicker than standard oceanic crust. From its highly perturbed relief, we interpreted the crust here to be heterogeneous, as a consequence of periods with different magma supply characteristic of slow spreading ridges. An additional effect contributing to the imaging of an apparently anomalous thickness could be the serpentinization of the sub-Moho mantle.

In Europe the presence of crustal roots beneath the major mountain belts has been confirmed, while thinned crust has been found below extensional basins.

Comparing the Moho topography obtained with the Moho depth computed assuming isostatic compensation at 60 km depth shows that most of the Mediterranean and eastern Atlantic region appears in isostatic equilibrium. In the eastern Mediterranean Basin strong positive residuals are likely due to overestimating the crustal thickness, owing to an extremely low average *S*-velocity in the upper crust. The lithospheric low density required for isostatic compensation in the Bay of Biscay region, contrasting with observed high *S*-velocities in the top 50 km of the mantle, confirms the presence of Archaean cratonic material.

# 3D upper mantle $S$ -velocity model for the Eurasia-Africa plate boundary region

---

## 4.1 Summary

A new regional  $S$ -velocity study resolving the Eurasia-Africa plate boundary region from the Azores to the eastern Mediterranean Sea is presented. The resolution of existing velocity models has been complemented by using new seismic broad band data recorded by the temporary MIDSEA network and at permanent European seismic stations. Following the Partitioned Waveform Inversion method, we interactively fitted the waveforms of  $S$ - and Rayleigh wave trains of more than 1100 seismograms. The linear constraints on upper mantle  $S$ -velocity provided by the waveform fits have been combined with independent estimates of Moho depth in a linear damped least-squares inversion for  $S$ -velocity and crustal thickness. The resulting  $S$ -velocity structure for the Mediterranean Sea shows strong lateral variations confirming the complex evolution of this plate boundary region. The upper mantle along the Eurasia-Africa suture zone is characterized by high-velocity material representing subducted oceanic lithosphere. This signature can be followed to as deep as 300-500 km, depending on the region and resolution. A high velocity body, possibly representing a fragment of subducted lithosphere, has been imaged beneath eastern

---

\*This chapter has been submitted to *J. Geophys. Res.* as: F. Marone, S. van der Lee, D. Giardini, 3D upper mantle  $S$ -velocity model for the Eurasia-Africa plate boundary region.

Spain between 250 and 500 km depth. Not only convergence has been recorded in the upper mantle, but also extension has its own signature beneath the Mediterranean. This is particularly clear for the Algero-Provençal and Tyrrhenian Basins, where a shallow asthenospheric layer is observed. The lithosphere-asthenosphere system of the western Mediterranean clearly differentiates itself from the structure of the older eastern Atlantic Ocean. Differences compared to the structure of a 4 to 20 Ma old ocean are also present. These observations support the idea that, rather than a young ocean, the western Mediterranean could be a strongly stretched continent, partly affected by spreading, formed at the back of a slab. The structure characterizing the eastern Mediterranean points to a continuation of the northern African continental lithosphere beneath the sea. Major structural differences in the eastern Atlantic Ocean are imaged between the Mid-Atlantic ridge and the older oceanic basins: the North Atlantic lithosphere is characterized by lower velocities beneath the spreading ridge than under the old ocean basins. Despite strong differences observed in the crustal structure between the Mid-Atlantic ridge and the Azores, no significant differences are observed in the upper mantle *S*-velocity structure.

## 4.2 Introduction

The Mediterranean region is characterized by the plate boundary between the Eurasian and African plates, extending from the Azores triple junction to Turkey and the eastern-most Mediterranean Sea. Convergence of these two large continental plates makes this a tectonically complex region showing strong lateral variations in past and present dynamics.

Fundamental for a deeper understanding of the evolution, deformation and dynamics of such a complex region, is the detailed knowledge of its 3D upper mantle structure. For example, a 3D velocity model can reveal differences in the nature of the Mediterranean basins, anomalies associated with mid-oceanic ridges, styles of past subduction, presence and extent of low rigidity parts of the mantle, differences in oceanic and continental lithosphere-asthenosphere systems and configuration of subducted lithosphere. This type of additional information about the ongoing processes is also necessary for advanced seismic and volcanic hazard assessment in the highly populated Mediterranean region. Moreover, a detailed velocity model is useful for removing wave propagation effects from seismograms, so reducing the uncertainties in earthquake location and focal mechanisms determination, in particular in highly heterogeneous regions, as for instance along a plate boundary.

Current models for the Mediterranean region are incomplete due to inhomogeneous data distribution. To improve the data coverage, 25 broad band three-component seismic stations have been deployed during the international project MIDSEA (Mantle Investigation of the Deep Suture between Eurasia and Africa) (Van der Lee et al., 2001). Most stations have been installed on Mediterranean islands or along the northern African coast and complement data coverage provided by existing networks and stations in the region.

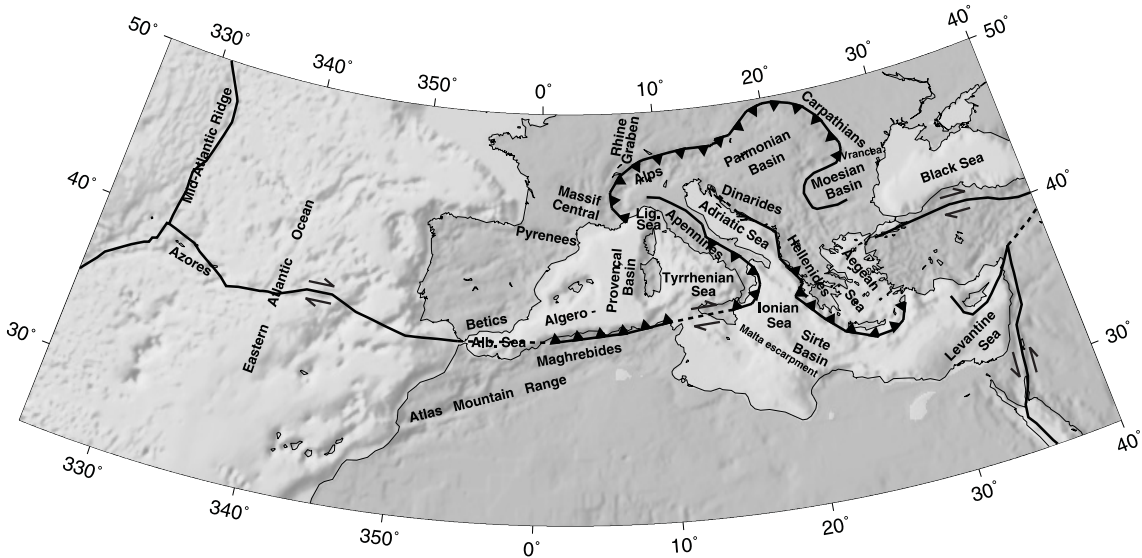


**Figure 4.1:** Topographic map of the Eurasia-Africa plate boundary region with approximate plate boundary location. Curves with sawtooth pattern indicate the present location of the convergent boundary, with sawteeth pointing in the direction of subduction or underthrusting. Strike-slip is represented by arrows.

In this study we combine new surface wave data recorded by the MIDSEA network with data from permanent broad band seismic stations to derive a 3D upper mantle  $S$ -velocity model for the Mediterranean region. We present the first regional model resolving the Eurasia-Africa plate boundary region from the Azores to the eastern Mediterranean Sea.

### 4.2.1 Tectonic background

The Eurasia-Africa plate boundary does not manifest itself as relatively sharp, but surface deformation, seismicity and earthquake focal mechanisms indicate a wide, diffuse and/or branched plate boundary. Owing to the formation and amalgamation of several semi-independent microcontinents between the two major plates, the plate boundary has changed location, shape and character throughout geological time (Dercourt et al., 1986). Despite slow convergence acting as the primary tectonic process in the region, different types of deformation affect and affected different parts of the suture zone. The plate boundary is not characterized by a single, continuous subduction zone, but several arcs with different orientations were active in different periods. Moreover, strike-slip and extension are also important tectonic processes influencing the region, e.g. along the Azores-Gibraltar fracture zone and in back-arc basins, respectively. Unique of the Mediterranean region is the small scale of complexity: typical lengths of the tectonic provinces span

1°-5° (Fig. 4.1).

The complex tectonic evolution of the plate boundary is described in detail in e.g. Dercourt et al. (1986), Dewey et al. (1989) and De Jonge et al. (1994). The history of the Mediterranean region is governed by the creation and subsequent destruction of the Tethys Ocean. After an early period dominated by extension and formation of oceanic lithosphere along different ridge systems, coincident with the breaking up of the Pangea landmasses (Jurassic-Cretaceous boundary), convergence has been acting as the primary plate tectonics process. About 65 Ma ago (Cretaceous-Tertiary boundary), following the opening of the Atlantic Ocean, the European and the African plates started to converge. Oceanic lithosphere formation in the region stopped and subduction and thrusting processes occurred along the entire northern Tethys margin. Owing to the continuous two-plate convergence, a large portion of oceanic lithosphere was consumed below several arcs marking the beginning (around 35 Ma ago) of mountain belts formation (Pyrenees, Betic Cordillera, Alps, Apennines, Carpathians, Dinarides and Hellenides). Parts of the original oceanic lithosphere (100 Ma old) are nowadays still preserved only in the eastern Mediterranean Sea (e.g. Levantine Basin). Recently, several back-arc basins were created mainly in the western Mediterranean Sea by rapid extensional activity (e.g. Algero-Provençal Basin (30-16 Ma) and Tyrrhenian Sea (10-0 Ma)).

#### 4.2.2 Previous studies

The upper mantle 3D velocity structure of the Mediterranean area has been the target of several tomographic studies. However, a detailed and complete image of the entire Eurasia-Africa suture zone has not yet been achieved. Existing models are either too local or patchy, or show a too long wavelength character inadequate to resolve features on Mediterranean scales.

Traveltime tomographic models, such as the non-linear global  $P$ -velocity model of Bijwaard & Spakman (2000) or regional  $P$ -velocity studies by e.g. Spakman et al. (1993) and Piromallo & Morelli (2003), do not resolve structures of the shallow mantle beneath the Mediterranean Basin. This is a consequence of lack of earthquakes and seismic stations in the sea and on the northern African coast and of the body waves travelling quasi-vertically through the lithosphere, leading to vertical leaking of the anomalies. The insufficient resolution of body wave tomographic models for the shallow mantle beneath aseismic regions covered by water has been documented by e.g. Spakman et al. (1993). Moreover owing to the different sensitivity of  $P$ -,  $S$ - and surface waves, our velocity model will emphasize different structures than body wave tomographic studies. For instance the conditions that decrease wave velocities, such as high mantle temperature, occurrence of melts and/or fluids or chemical composition, have a significantly larger effect on  $S$ - rather than on  $P$ -velocities (Cammarano et al., 2002). Therefore, locations where these conditions exist, are more easily detected using  $S$ - and surface waves.

Recent global studies that involve the inversion of surface-wave data (e.g. Boschi, 2001;



Shapiro & Ritzwoller, 2002) clearly image the long wavelength structure of the Mediterranean region, but are still inadequate to describe its complex upper mantle.

Surface waves regional studies for the Mediterranean region were introduced by Panza et al. (1980), who presented the first maps outlining the regionalization of the crust and lithosphere-asthenosphere system in the western and central Mediterranean. Snieder (1988) inverted waveforms of fundamental mode Rayleigh waves and their coda for a two-layered lateral model of  $S$ -velocities in the upper 200 km of the mantle. Zielhuis & Nolet (1994) presented a 3D  $S$ -velocity model for Europe and part of the Mediterranean region. However, they observed that surface wave analysis around the plate boundary region suffers from the structural complexity, which could not be adequately modeled for lack of closely distributed seismic stations. Zielhuis & Nolet (1994) show a map of wave paths for which the waveform fits were poor: the map is dominated by Mediterranean paths, often longer than  $20^\circ$ , while the typical length of tectonic provinces in the region spans  $1^\circ$ - $5^\circ$ . Marquering & Snieder (1996) did not improve the path coverage for the Mediterranean region relative to that of Zielhuis & Nolet (1994). Martínez et al. (2000) presented a 3D  $S$ -velocity model focused on the Mediterranean Basin. However, their model is based on a limited set of available seismograms and on only fundamental mode Rayleigh waves. Moreover, a geodynamic interpretation of their results is not yet possible since the spatial resolution of their dataset is still unpublished.

Higher-resolution regional studies tend to focus on a specific region within the Mediterranean Basin. Among others, Papazachos & Nolet (1997) have resolved the high-velocity structure of the subducting African plate in the mantle beneath the Aegean region using  $P$ - and  $S$ -waves travel times. Southern Spain and the Alboran Sea have also been the target of several tomographic studies. Here, a high velocity body has been imaged in the mantle between 200 and 700 km. Blanco & Spakman (1993) interpreted this anomaly as subducted lithosphere, possibly detached from the surface. The upper mantle beneath the Italian peninsula has also been the object of intensive investigations (e.g. Lucente et al., 1999).

Only few  $S$ -velocity studies exist for northern Africa. Ritsema & Van Heijst (2000) presented a regional model for entire Africa, focusing on gross features such as cratons and the East African Rift, while short wavelength structures typical for the Mediterranean region are averaged out.

### 4.3 Method

We apply the version of Partitioned Waveform Inversion (PWI) described by Van der Lee & Nolet (1997). Here we use PWI to image the 3D  $S$ -velocity upper mantle structure of the Mediterranean region using vertical and radial component seismograms recorded at European and northern African broad band seismic stations. In addition to the 3D  $S$ -velocity model presented here, the application of this technique also yields a map for the Moho discontinuity, which has been discussed separately (Marone et al., 2003b).

In the first part of PWI, the 1D average  $S$ -velocity structure and Moho depth along each path are determined by non-linear waveform fitting of wave trains composed of fundamental and higher mode surface waves. In the second part, the path average velocity structures obtained from waveform fitting and independent point constraints on Moho depth are combined in a damped linear inversion for 3D  $S$ -velocity and crustal thickness.

### 4.3.1 Waveform modeling

We obtained path average 1D  $S$ -velocity models, for which synthetic seismograms best fit observed waveforms, by minimizing the objective function  $F(\gamma)$  making use of a non-linear optimization method based on conjugate gradients (Nolet, 1990; Van der Lee & Nolet, 1997):

$$F(\gamma) = \int w^2(t)[\mathbf{R}d(t) - \mathbf{R}s(t, \gamma)]^2 dt \quad (4.1)$$

where  $d(t)$  is the recorded and  $s(t, \gamma)$  the synthetic seismogram, which depends on the model parameters  $\gamma$ .  $\mathbf{R}$  is a filtering and windowing operator and  $w(t)$  a weighting function designed, using the inverse of the signal envelope, to enhance the contribution to the misfit of the higher modes with respect to the naturally dominating fundamental mode.

We constructed synthetic seismograms by summation of the first 20 Rayleigh mode branches, with phase velocities between 2 and 10 km/s. The non-linear nature of the waveform fitting procedure requires the use of 1D starting models close to the average  $S$ -velocity structure along each path. Strongly affecting the computed synthetic waveforms is the choice of the Moho depth and the presence of a water layer. To significantly reduce effects possibly introduced by nonlinearities, we used different 1D background models to compute synthetic seismograms for each wave path according to the average structure of the region crossed by the seismic wave. For continental paths, models similar to *iasp91* (Kennett & Engdahl, 1991) with different crustal thicknesses (ranging from 20 to 45 km) have been chosen. For paths crossing comparable amount of sea and land, a water layer (2 km or 4 km thick for waves travelling through the Mediterranean region or the Atlantic Ocean, respectively) has been introduced in the above-mentioned models. A 1D velocity model characterized by upper mantle low velocities (minimum velocity of 4.29 km/s at 100 km depth and velocities 0.1 km/s smaller than for *iasp91* between 210 and 410 km depth) has been used for paths crossing Eastern Europe. Moreover, local Earth structure at the earthquake source is accounted for by assuming appropriate Earth model (out of the described set) when excitation factors are computed. In addition to a priori information on the path average structure, a second criterium for the selection of the 1D background models was the similarity between recorded and synthetic waveforms. Using surface wave ray theory (WKB approximation), the synthetic is expressed in terms of the average wave number along the path. Perturbations to the wave number are related to variations in the starting model using Fréchet derivatives (Takeuchi & Saito, 1972), which are used to compute waveform derivatives.

The average velocity perturbation along the path between source and receiver is parameterized in terms of a number of basis functions, which are chosen as a mix of boxcar and triangular functions in order to incorporate both discontinuities and gradients in the model. The perturbations are then expressed in the form of linear equations with uncorrelated uncertainties.

The fits are dominated by phase matches for the waves of different modes and frequencies, while the amplitude differences between observed and synthetic waveforms are not explicitly included as constraints on Earth structure because of the strong ambiguity in the interpretation of Rayleigh wave amplitude anomalies (Van der Lee, 1998). Since in PWI the observed and synthetic waveforms are compared in the time domain, it is possible to identify data contaminated by significant multipathing effects. Selection of wave trains uncontaminated by scattered waves ensures accuracy of our measurements.

#### 4.3.2 Point constraints on crustal thickness

To reduce trade-offs between Moho depth and velocity structure around it, which are inherent in the Rayleigh waves used in this study, we have collected independent estimates of Moho depth obtained from receiver function analysis, seismic refraction/reflection surveys and gravity data studies (see Appendix A in Marone et al. (2003b) for complete list of references). Uncertainties related to the individual point measurements differ depending on the method used to determine the crustal thickness estimate. Under the assumption of a flat Moho (e.g. Van der Meijde et al., 2003b), crustal thickness data obtained with receiver function analysis have an error around  $\pm 1$ -2 km. Uncertainties related to the results of refraction and/or reflection seismology vary depending on the data quality. In general results of gravity studies have larger errors.

#### 4.3.3 3D inversion

The 3D  $S$ -velocity model is parametrized as coefficients of a Cartesian grid of nodes, while for the Moho depth a triangular grid of nodes is adopted on a spherical shell (Van der Lee & Nolet, 1997). For the  $S$ -velocity model, the distance between the nodes in the  $x$  and  $y$  direction is 100 km, in the  $z$  direction 60 km. The distance between the nodes of the triangular grid is compatible with the inter-knot spacing in the Cartesian grid and is 97 km on average. Trilinear interpolation was used to determine the value of the solution at a given point.

Since the 1D path average velocity models obtained by fitting waves travelling through the Mediterranean region show that the crust is on average thinner than the 35 km of *iasp91* and that the upper 200 km of the mantle are characterized by low velocities, we have used a reference model in the inversion for the 3D  $S$ -velocity structure that is similar to *iasp91*, but has a crustal thickness of 30 km and lower  $S$ -velocities in the upper mantle (Fig. 4.2). However, the obtained 3D solution is robust and does not depend on the adopted 1D start-

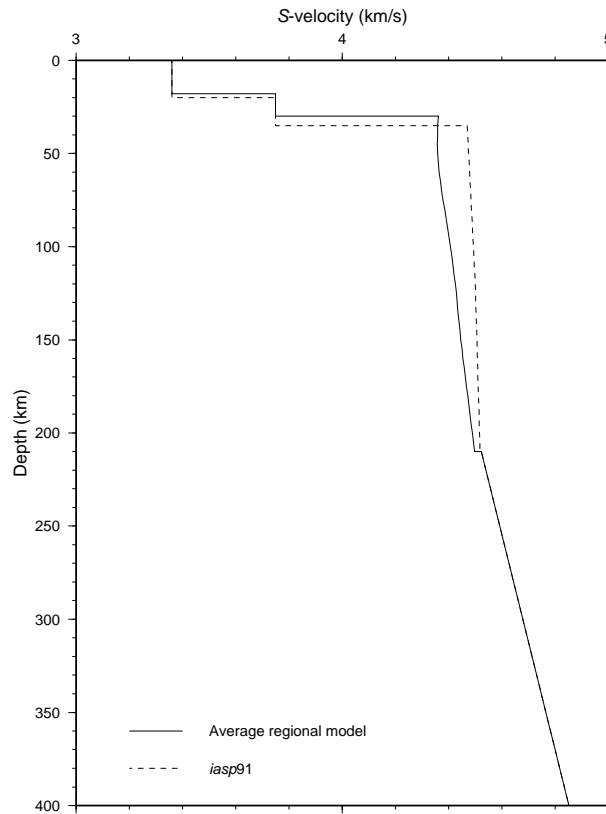


**Figure 4.2:** Average  $S$ -velocity model for the Mediterranean region used as starting model in the 3D inversion compared to *iasp91* (Kennett & Engdahl, 1991).

ing model: minor differences, smaller than the estimated uncertainties, are observed for the amplitudes of the anomalies, while the shape and position of the velocity anomalies are robust features. Similar results are also achieved using as starting model a realistic 3D velocity model for the Mediterranean region. Since we chose 1D starting models for the waveform fitting specific for each path, the obtained linear equations are rewritten to describe 3D perturbations in Earth structure with respect to the 1D reference model chosen for the 3D inversion.

Since the algorithm used to solve the system of equations (LSQR (Paige & Saunders, 1982)) yields a minimum-norm solution, we work with a dimensionless model vector. The model vector is made dimensionless by scaling it with the expected standard deviation of the model parameters: 225 m/s for  $S$ -velocities and 4 km for Moho depths. Since we are jointly inverting 2 different sets of constraints, the system has to be scaled. The data covariance matrix  $C_d$  scales each row of the constraint matrix, controlling the relative importance of each constraint. As scaling factor, the estimated uncertainty of each

constraint is used: for surface wave constraints derived in the waveform fitting procedure (Van der Lee & Nolet, 1997), for point constraints taken from the literature (see section 4.3.2). To select the relative weight of the 2 datasets, we opted for a balance between smoothed Moho topography and exact match between point constraints and resulting crustal thickness values. For the chosen balance, most point constraints are met by the Moho map within their double standard deviation, while Moho topography remains smooth (Marone et al., 2003b).

We obtain the linear system of equations:

$$C_d^{-\frac{1}{2}} \mathbf{A} \mathbf{m} = C_d^{-\frac{1}{2}} \mathbf{d} \quad (4.2)$$

where  $\mathbf{A}$  is the constraint matrix,  $\mathbf{m}$  the model and  $\mathbf{d}$  the data vector. To imitate the wide sensitivity region of long period waves and to suppress the artificial rough structure in the model caused by errors in the data, we require a priori that the velocity in the Mediterranean region varies smoothly. Smoothing was applied horizontally. The value of the smoothing function decreases linearly from the center to zero at a chosen distance. This means that we express the model  $\mathbf{m}$  as:

$$\mathbf{m} = \mathbf{S} \mathbf{n} \quad (4.3)$$

where  $\mathbf{S}$  is the smoothing matrix and  $\mathbf{n}$  the rough model. The system becomes:

$$C_d^{-\frac{1}{2}} \mathbf{A} \mathbf{S} \mathbf{n} = C_d^{-\frac{1}{2}} \mathbf{d} \quad (4.4)$$

which is rewritten as:

$$\mathbf{H} \mathbf{n} = \mathbf{q} \quad (4.5)$$

where  $\mathbf{H} = C_d^{-\frac{1}{2}} \mathbf{A} \mathbf{S}$  and  $\mathbf{q} = C_d^{-\frac{1}{2}} \mathbf{d}$ .

We add regularization equations to the system that bias the rough solution  $\mathbf{n}$  towards zero norm. The system then becomes:

$$\begin{pmatrix} \mathbf{H} \\ \lambda \mathbf{I} \end{pmatrix} \mathbf{n} = \begin{pmatrix} \mathbf{q} \\ \mathbf{0} \end{pmatrix} \quad (4.6)$$

where  $\lambda$  is the damping coefficient. We solved this linear system of equations iteratively using the least squares algorithm LSQR (Paige & Saunders, 1982).

## 4.4 Data

The coverage of the Mediterranean region with broad band seismic stations is inhomogeneous. While for Europe the availability of broad band data in the last decade has significantly increased, broad band stations are inexistent or rare in northern African countries, on Mediterranean islands and on the seafloor. Moreover, because the Mediterranean upper

**Table 4.1:** *Location of the MIDSEA stations.*

<b>Code</b>	<b>Location</b>	<b>Latitude</b>	<b>Longitude</b>	<b>Altitude (m)</b>
CDLV	Spain	29.163	-13.444	37
EBRE	Spain	40.823	0.494	36
MELI	Spain	35.290	-2.939	40
POBL	Spain	41.379	1.085	550
DUOK	Croatia	44.113	14.932	115
HVAR	Croatia	43.178	16.449	250
APER	Greece	35.550	27.174	250
ITHO	Greece	37.179	21.925	400
KOUM	Greece	37.704	26.838	340
GHAR	Libya	32.122	13.089	650
MARJ	Libya	32.523	20.878	650
CALT	Italy	37.579	13.216	955
DGI	Italy	40.318	9.607	343
GRI	Italy	38.822	16.420	525
MGR	Italy	40.138	15.553	297
SOI	Italy	38.073	16.055	300
VENT	Italy	40.795	13.422	110
ABSA	Algeria	36.277	7.473	1025
RUSF	France	43.943	5.486	520
SMPL	France	42.094	9.285	405
COV2	Portugal	39.677	-31.113	194
PGRA	Portugal	39.029	-27.981	245
PSCM	Portugal	38.701	-27.117	400
PSJO	Portugal	38.422	-28.303	258
PSMA	Portugal	36.996	-25.131	249

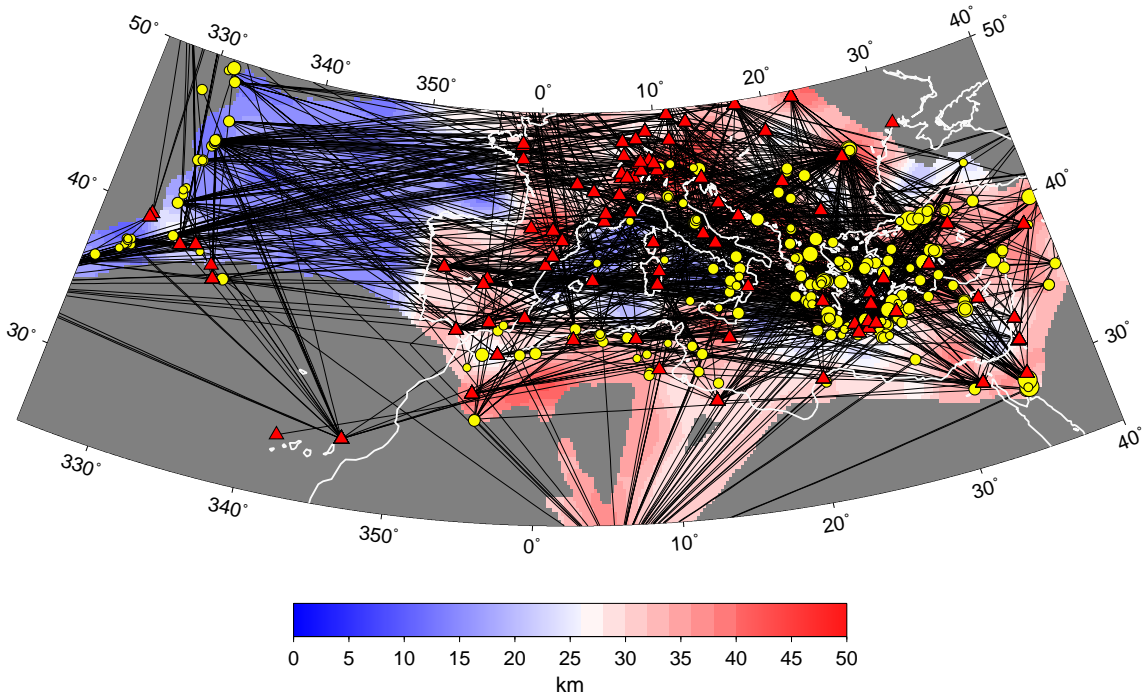


**Figure 4.3:** Great circle ray paths for the 1136 seismograms used in this study. Red triangles and yellow dots represent used broad band seismic stations and events, respectively. In the background the Moho map obtained in Marone et al. (2003b) is shown.

mantle is characterized by strong lateral heterogeneities associated with subduction of the African plate, which results in distortion of the waveforms by scattered energy, we need to include relatively short wave paths. For these reasons, during the MIDSEA project, 25 broad band recording instruments were temporarily installed in locations with a poor station density (Tab. 4.1) (Van der Lee et al., 2001). In addition to data of the temporary MIDSEA network, seismograms recorded by permanent broad band stations of the Swiss National Network (Baer, 1990), IRIS, MedNet (Boschi et al., 1991), Un. Trieste, Géoscope (Romanowicz et al., 1984), RéNaSS, TGRS, GEOFON (Hanka & Kind, 1994), GRSN (Hanka, 1990), GRF, Un. Stuttgart, GII, Un. Barcelona, Un. Madrid, Inst. Andaluz, Czech National Seismological Network (CZ), NARS (Paulssen, 1992), GI\_Budapest and Blacknest have been collected.

For this study we selected vertical and radial component seismograms with a good signal-to-noise ratio for  $SV$  and/or Rayleigh waves for regional events occurred between 1985 and 2002. Our dataset consists of events with a magnitude between 4.1 and 7.6. The hypocenter depth ranges from 1.5 down to 396 km. The epicentral distance is, except for the events located in the Atlantic Ocean,  $< 30^\circ$  and the median path length is  $15^\circ$ . For the

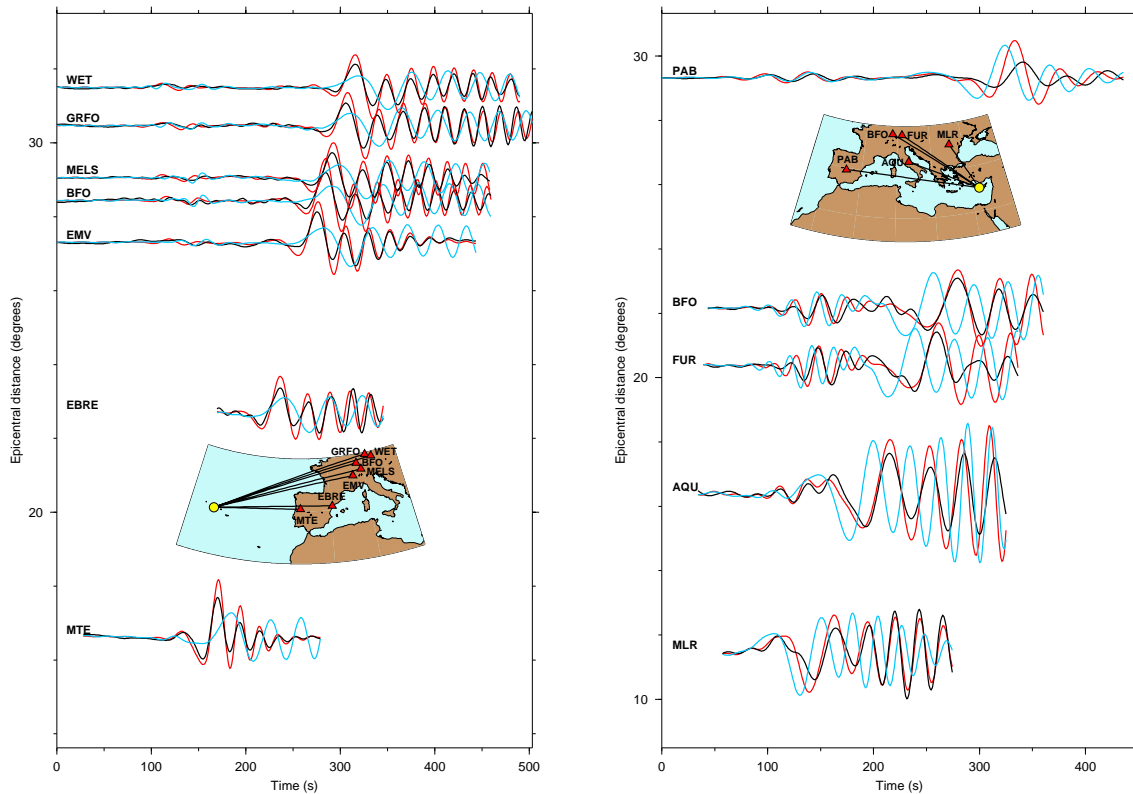


**Figure 4.4:** Observed waveforms (black lines), synthetic seismograms for the 1D average  $S$ -velocity model for the Mediterranean region used as starting model in the 3D inversion (blue lines) (Fig. 4.2) and synthetic seismograms computed with the obtained 3D  $S$ -velocity model (red lines). The wave paths and the location of the events and stations are shown in the insets. A reduction velocity of 6 km/s has been used - On the left for the event on August 1, 2000,  $m_w$  5.1 at the Mid-Atlantic Ridge, - On the right for the event on May 29, 1995,  $m_w$  5.3 on Cyprus.

synthetic seismogram calculation the hypocenter location and origin time were taken from NEIC Preliminary Determination of Hypocenters for recent earthquakes and from the catalogue of Engdahl et al. (1998) and Engdahl (personal communication) for older events, the moment tensor solutions from online Harvard catalogues (e.g. Dziewonski et al., 1994) when available. For small regional events that occurred between 1999 and 2002, we used the solutions computed by Braunmiller et al. (2002). In a few cases we adopted the focal mechanisms from online MedNet catalogue ([www.ingv.it/seismoglo/RCMT/](http://www.ingv.it/seismoglo/RCMT/)) or obtained by Thio et al. (1999). Only azimuths away from the fundamental mode Rayleigh wave source-radiation nodes have been considered.

For each selected seismogram, after a quality check and deconvolution of the instrument response, one or two time windows containing the fundamental mode and/or higher modes



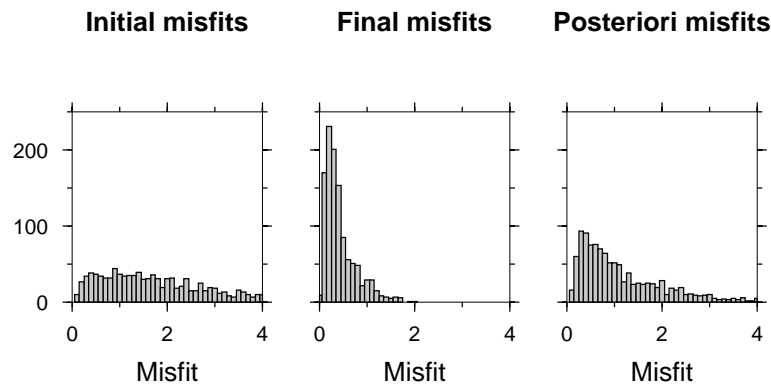


**Figure 4.5:** Histogram for the misfit for each waveform computed according to eq. 4.1. On the left, misfit of synthetics computed using our best guessing starting model ('initial' fits); in the center, calculated with the best 1D path-averaged model ('final' fits); on the right, calculated from the final 3D  $S$ -velocity model EAV03 ('posteriori' fits). The total misfit reduction from 'initial' to 'final' is 81%, from 'initial' to 'posteriori' is 41%.

of the Rayleigh wave forms were interactively fitted. Frequencies ranging from 6 mHz up to 100 mHz were included in the optimal case. After data selection and following analysis, 1136 fitted waveforms of vertical and radial component seismograms from 235 events recorded by 117 different seismic stations have been obtained (Fig. 4.3), which result in 8212 linear constraints on the 3D upper mantle  $S$ -velocity structure for the Mediterranean region. A joint linear inversion of these constraints and independent estimates of crustal thickness (Marone et al., 2003b) yields our 3D  $S$ -velocity model (EAV03). The value of the damping parameter was chosen so as to optimize the trade-off between variance reduction and model smoothness and was set equal to 1.0. We chose 200 km for the half width of the smoothing function. After 40 iterations, the inversion starting with the average 1D model for the Mediterranean region (Fig. 4.2) resulted in a 96% variance reduction and the linear constraints were fitted to approximately 3 estimated standard deviations. After 60 additional iterations the fit to the linear constraints is changing by less than 0.1%.

The fit to the data was assessed by calculating a posteriori synthetic waveforms and comparing them to the data. A posteriori synthetic seismograms have been computed by mode summation using 1D averages through the obtained 3D velocity model along the source-receiver paths (Fig. 4.4). The fit to the data is good both for the fundamental mode Rayleigh wave trains and the higher-mode/body wave trains. Owing to the applied damping and smoothing and to the least squares nature of the 3D inversion, the 'posteriori' fits are not as good as the individual 'final' fits (not shown here) and as expected the misfit distribution is slightly wider than for the 'final' fits (Fig. 4.5). However, a significant improvement compared to the 'initial' waveform fits (Fig. 4.4) is observed as well as a significantly narrower misfit distribution (Fig. 4.5). A systematic analysis of the ray

paths with the worst ‘posteriori’ fits did not show any clear correlation with geography or epicentral distance. This indicates that the influence of scattered wave energy due to complexity in the earth structure is limited and that the isolated large misfits are a consequence of inaccuracies e.g. in seismic moment determination and unmodeled attenuation structure.

## 4.5 Resolution

The coverage of the Mediterranean region with great circle wave paths, from which linear constraints have been derived with the waveform fitting procedure, gives a first idea of the resolution, which can be achieved with our dataset. Fig. 4.3 shows that the path coverage is not homogeneous. For eastern, central Europe and the northern part of the Mediterranean Basin an optimal resolution can be expected, because the region is sampled by a large number of crossing waves. However, for the eastern Atlantic Ocean, for the southern Mediterranean Basin and especially for northern Sahara, the path coverage is sparse due to an inconvenient station and event distribution. The path density is not as high as for continental Europe and for the northern Mediterranean Basin and most waves travel parallelly. Therefore the resolution will be limited and lateral smearing along the main path directions has to be expected.

To assess the resolving power of our dataset, we have performed tests, in which a known Earth model and the data sensitivity matrix ( $\mathbf{H}$  in eq. 4.5) of our system are used to compute synthetic data ( $\mathbf{q}$  in eq. 4.5). After adding Gaussian distributed noise so as to simulate the same signal-to-noise ratio as for the data, the inversion is performed with the same parameters as for the real data. To test different aspects of the resolution, a series of different Earth models has been chosen, ranging from completely unrealistic but standard pattern of spike anomalies to realistic models simulating e.g. subduction zones and asthenospheric layers. A series of checkerboard tests with synthetic anomalies at different depths, of different sizes and arranged in different patterns shows that the resolution decreases with depth and bigger anomalies are better resolved than smaller ones. Also the recovered anomaly amplitude decreases with depth. Horizontal smearing in the main path direction is observed in regions with insufficient crossing paths. This effect is more prominent at depth. Examples are shown in Figs. 4.6 and 4.7. The input models for these resolution tests consist of variable-size  $S$ -velocity anomalies of alternating sign with an amplitude of  $\pm 250$  m/s and  $\pm 400$  m/s relative to an average Mediterranean 1D velocity model (Fig. 4.2) in Figs. 4.6 and 4.7 respectively. The best resolution is observed at 75-100 km depth, where the anomaly shape is well recovered and the amplitude is restored up to 70% for the Mediterranean region, eastern, central and western Europe. Beneath northern Africa, the Atlantic European coast and the eastern Atlantic Ocean the resolution is limited due to insufficient data and horizontal smearing along the dominant wave paths direction is observed. At 300 km depth, for the regions with the best path coverage, the anomalies are fairly well recovered, even if smearing in E-W direction is present and

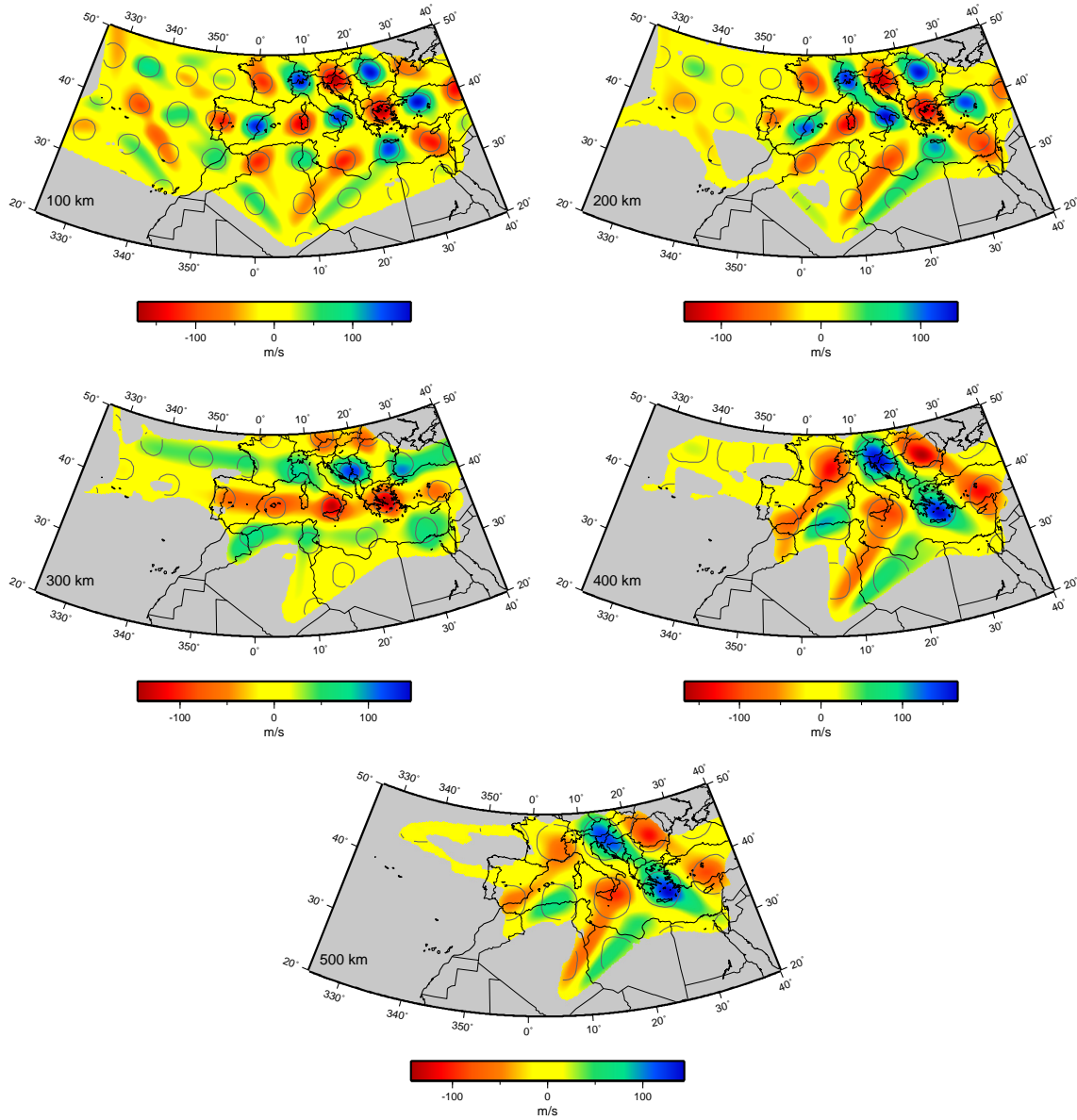


**Figure 4.6:** Spike resolution test results at different depths. The input model is represented by the grey contours at  $\pm 100$  m/s. The anomalies of the output model are shaded.

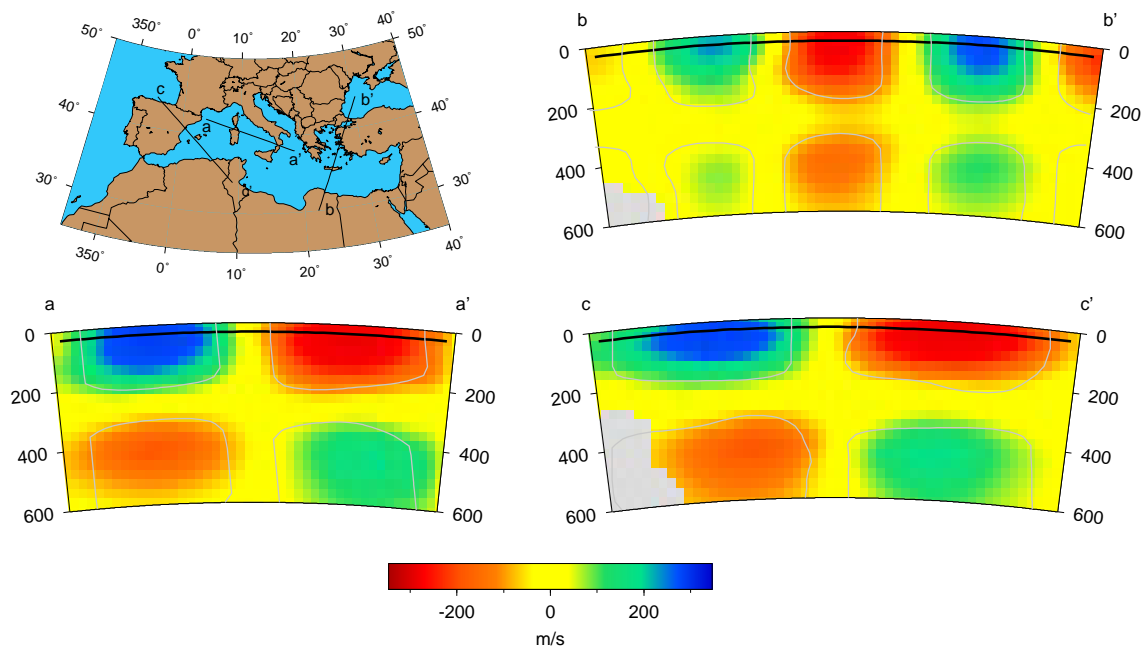


**Figure 4.7:** Spike resolution test results for three different cross sections taken along the great circle segments shown in the map. The  $\pm 150$  m/s level of the anomaly amplitude of the input model is represented by the contours. The anomalies of the output model are shaded.

the magnitude of the anomalies is underestimated by 50% because of damping applied in the inversion. Thanks to the inclusion of constraints from higher mode waveforms, the sensitivity deeper in the upper mantle is still significant. As deep as 500 km, 800 km wide structures can still be detected beneath Europe and the Mediterranean region. However, up to 50% of the original anomaly amplitude can be recovered only beneath the eastern and central part of the Mediterranean. For northern Africa and the western Mediterranean Basin not more than 25% of the input amplitude is restored. Our dataset provides an excellent resolution of the depth extent of the anomalies as shown in Fig. 4.7.

The resolution was further investigated using a model with more realistic anomalies simulating subducting lithosphere beneath e.g. the Hellenic and the Calabrian arc and an asthenospheric layer beneath e.g. the western Mediterranean (Fig. 4.8). For this test an adapted version of the  $P$ -velocity model BSE\_NL of Bijwaard & Spakman (2000) was used as input structure. The recovered model shows, that the short-wavelength  $P$ -velocity structure could not be resolved, because the limit of the resolving power of the surface waves in the frequency range we used was reached and because of the applied smoothing. However, especially at shallow depths (75-150 km), the long-to-intermediate wavelength character of the input structures has been resolved. Even narrow features as the high velocity anomaly beneath the Hellenic arc can be imaged with our dataset. Deeper in

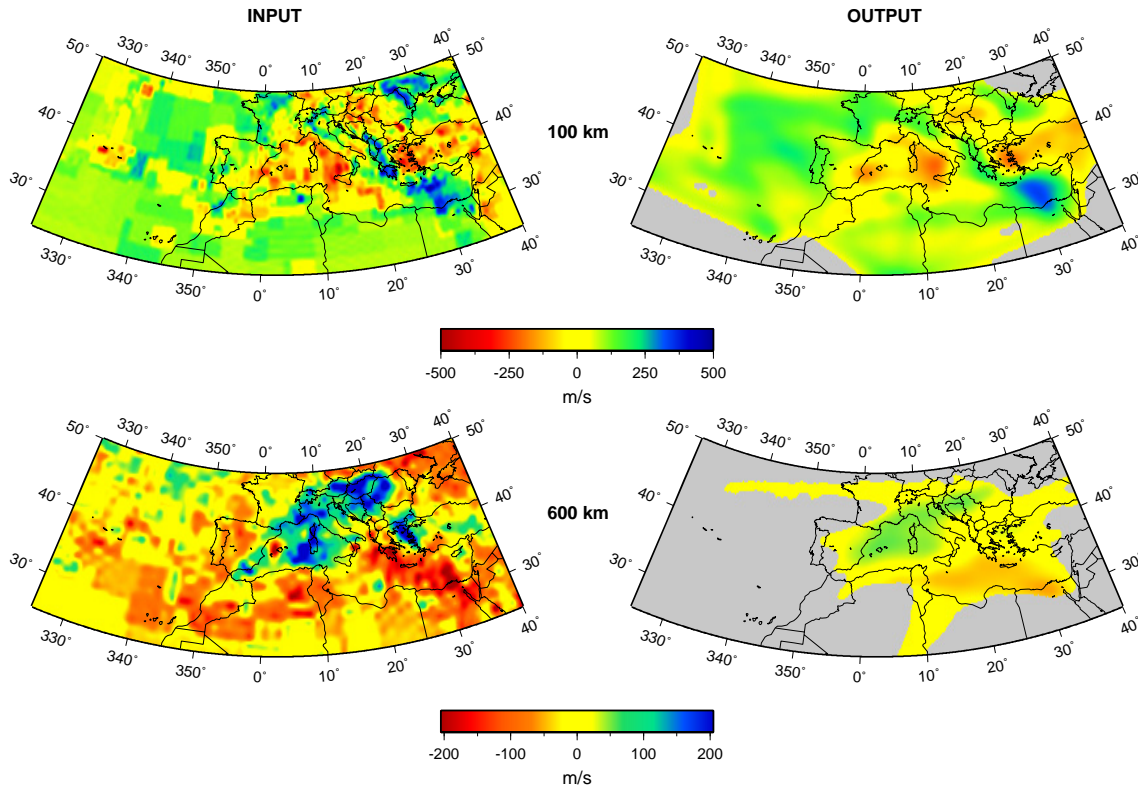


**Figure 4.8:** Results at 2 different depths of a recovery test with a realistic input model (on the left) simulating structures present in the Mediterranean region. The recovered model is shown on the right.

the upper mantle, the major structures could be imaged down to 600 km, although the anomaly amplitudes are reduced by 50% and horizontal smearing is observed in regions with a poor crossing wave path coverage.

We carried out further testing to check that no structural bias is introduced by the wave path geometry and data sensitivity. For this purpose we used a constant synthetic model, with a velocity anomaly of 300 m/s and no noise addition. In a second step the influence of noise has been tested using the same input structure, but adding noise vectors with different standard deviations to the computed synthetic data. As expected it has been observed that with increasing standard deviation of the noise vector, the amplitude of the recovered perturbations with respect to the constant synthetic model is also increasing, but that increasing damping is limiting the bias of the results due to noise. For the damping value used in this study, the anomaly amplitudes of the recovered noise artifacts are only 1/8 of those in the obtained  $S$ -velocity model, so that normally distributed noise is not significantly biasing the recovered structure. In Fig. 4.9 an example is shown, where

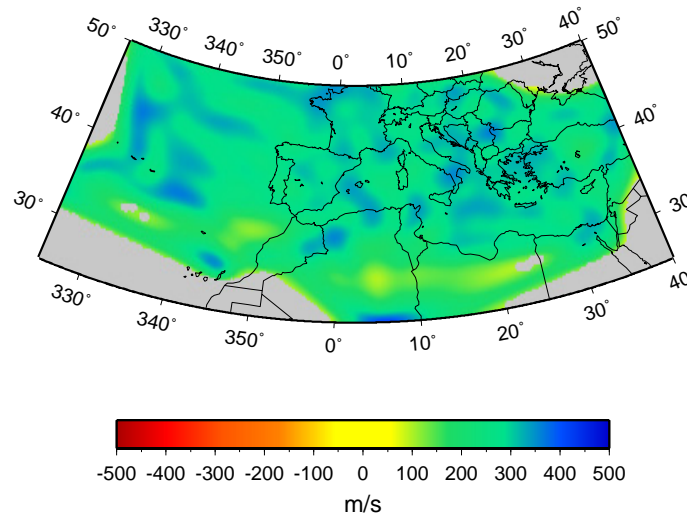


**Figure 4.9:** Results of a resolution test showing the effect of noise on the obtained velocity model at 100 km depth. The input model consists of a constant velocity anomaly of 300 m/s, the standard deviation of the noise vector has been chosen so as to simulate the signal-to-noise ratio of the data.

the standard deviation of the noise vector has been chosen so as to simulate the signal-to-noise ratio of the real data.

Several inversions with different subsets of the complete dataset have also been performed to investigate the influence of specific paths on certain anomalies. In a first step, the subsets have been created randomly. The inversion results show that the recovered upper mantle  $S$ -velocity structure is robust and does not depend on single paths. In a second step, data belonging to specific events have been removed, to check the reliability of individual structures. Also in this case, it turned out that the observed features are robust and do not depend on one single event or path.

In theory, the obtained  $S$ -velocity model could be biased by the presence of azimuthal anisotropy. In regions with a dense coverage with crisscrossing paths, this possible effect is reduced because the azimuthal variations are averaged out at each point of the model. The influence of azimuthal anisotropy on our model has, however, been estimated (Llyod, 2003), by constructing a vector  $\mathbf{q}$ , which describes the contribution of azimuthal anisotropy for each single path (Schmid et al., 2003). The model obtained in an inversion using the so constructed data vector, shows that the estimated azimuthal anisotropy, even for the extreme case where it is concentrated in the thinnest possible shallow layer, is not significantly biasing our results. The strongest effect of ignoring the contribution of azimuthal anisotropy on our model is observed along the Italian peninsula, where large delay times between fast and slow wave components have been measured (Margheriti et al.,

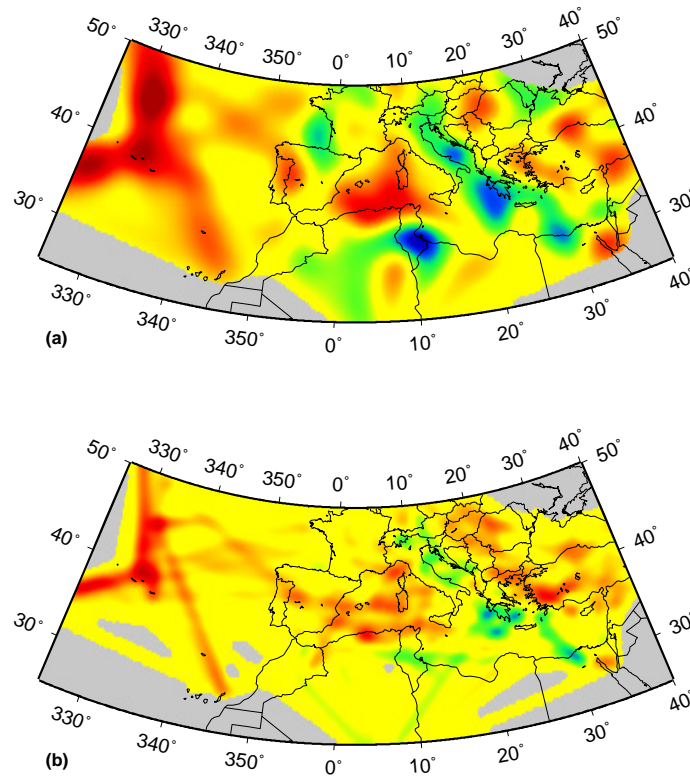


**Figure 4.10:** Horizontal slices at 100 km depth through two  $S$ -velocity models, which show a comparable fit to the data - (a) “Smooth” model obtained with a node spacing of 100 km and 60 km in the horizontal and vertical directions respectively, and a smoothing function half width of 300 km, (b) “Rough” model obtained with a smaller grid spacing (50 km and 30 km in the horizontal and vertical directions) and a smaller half width for the smoothing function (100 km).

2003). Here we locally overestimate uppermost mantle velocities by up to 2%, possibly contributing to image positive anomalies artificially more homogeneous and continuous.

#### 4.5.1 Choice of the final model

Solution of underdetermined problems is non-unique and a set of models exists, which fit the data equally well. Models differ depending on the regularization applied, on the cell size and smoothing parameter chosen for the inversion. In Fig. 4.10, two end-members of the possible solution range are shown. The quality of the fit to the data of the posteriori synthetics computed with these two models is comparable to the posteriori fits obtained with our preferred model. For the first  $S$ -velocity model presented, a smoothing function half width of 300 km has been chosen. The characteristic wavelength of the anomalies in this model is comparable with the size of the features imaged e.g. in regional tomo-

graphic results obtained from global measurements (Boschi, 2001). The second example has been chosen because it shows the same characteristics, in terms of model roughness and anomaly size, as *P*-velocity models (e.g. Piromallo & Morelli, 2003). This solution has been obtained using a finer Cartesian grid of nodes and a smaller half width for the smoothing function (100 km) compared to the previous example. However, the reliability of this model is questionable because of artefacts introduced by the increased relative influence of noise and wave path distribution.

An estimate of the details, which can be resolved with the used dataset, guides in the selection of node spacing and smoothing parameter. First, the resolving power of a seismogram for the average earth structure along its path is controlled by the Fresnel zone. If ray theory is used, as in this study, heterogeneities smaller than the width of the first Fresnel zone can not be resolved. To exceed this limit, scattering of surface waves should be taken into account as described by e.g. Nolet & Dahlen (2000), Spetzler et al. (2001) and Ritzwoller et al. (2002). Second, due to the averaging properties of surface waves propagating along a great circle, better resolution is expected in depth than in the horizontal directions (Figs. 4.6 and 4.7). For these reasons, we chose the node spacing in the *z* direction to be 60 km, smaller than the 100 km node spacing selected for the *x* and *y* directions. The lesser resolution in the horizontal directions is additionally taken into account by a smoothing function, which, in the selected final model, has a half width of 200 km.

The value of the damping parameter was chosen so as to optimize the trade-off between variance reduction and model smoothness. The applied damping limits the possible bias of the sub-Moho mantle velocity structure arising from trade-offs with the insufficiently controlled crustal *S*-velocities. Only in regions with an anomalously low average crustal velocity due to thick sedimentary deposits (up to 14 km in the eastern Mediterranean), the uppermost mantle velocity could be significantly underestimated. Damping is however also responsible for the strong underestimation (up to 60-70%) of the amplitude anomaly in the lower upper mantle (400-600 km).

## 4.6 Results

The obtained *S*-velocity structure for the Mediterranean and surrounding regions (EAV03) is shown in horizontal slices at different depths in Fig. 4.11. The complex origin and evolution of this plate boundary area (Dercourt et al., 1986) is reflected in the upper mantle structure: the presented shear wave velocity model is strongly heterogeneous.

Compared to previous *P*- (e.g. Piromallo & Morelli, 2003) and *S*-velocity models (Zielhuis & Nolet, 1994; Marquering & Snieder, 1996) for the Mediterranean region, we extended the results for the Mediterranean Sea itself and for northern Africa. Also the crust and uppermost mantle structure beneath the eastern Atlantic Ocean is better constrained compared to existing *P*- (e.g. Bijwaard & Spakman, 2000) and *S*-velocity (e.g. Silveira & Stutzmann, 2002) studies.



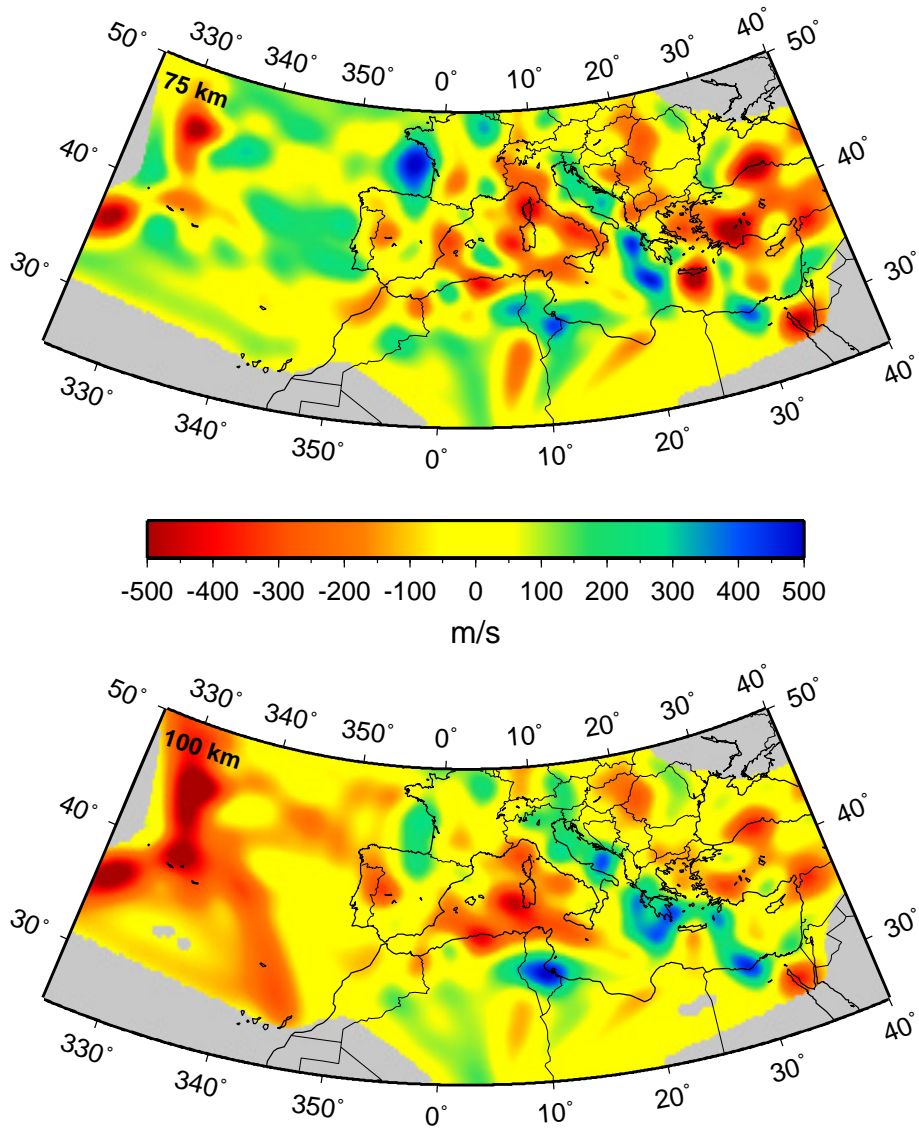


**Figure 4.11:** Horizontal slices at different depths through EAV03. Velocities are relative to the 1D average velocity model shown in Fig. 4.2.

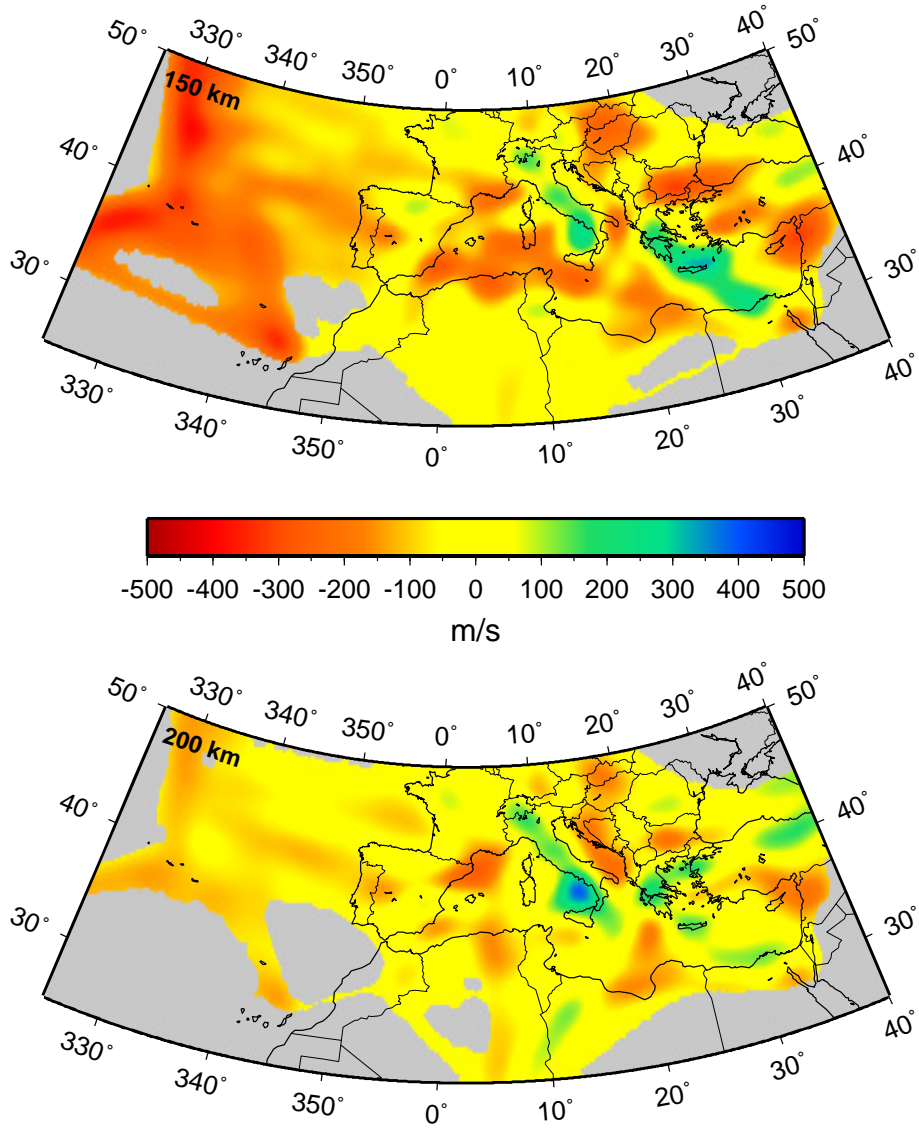


Figure 4.11: (continued)

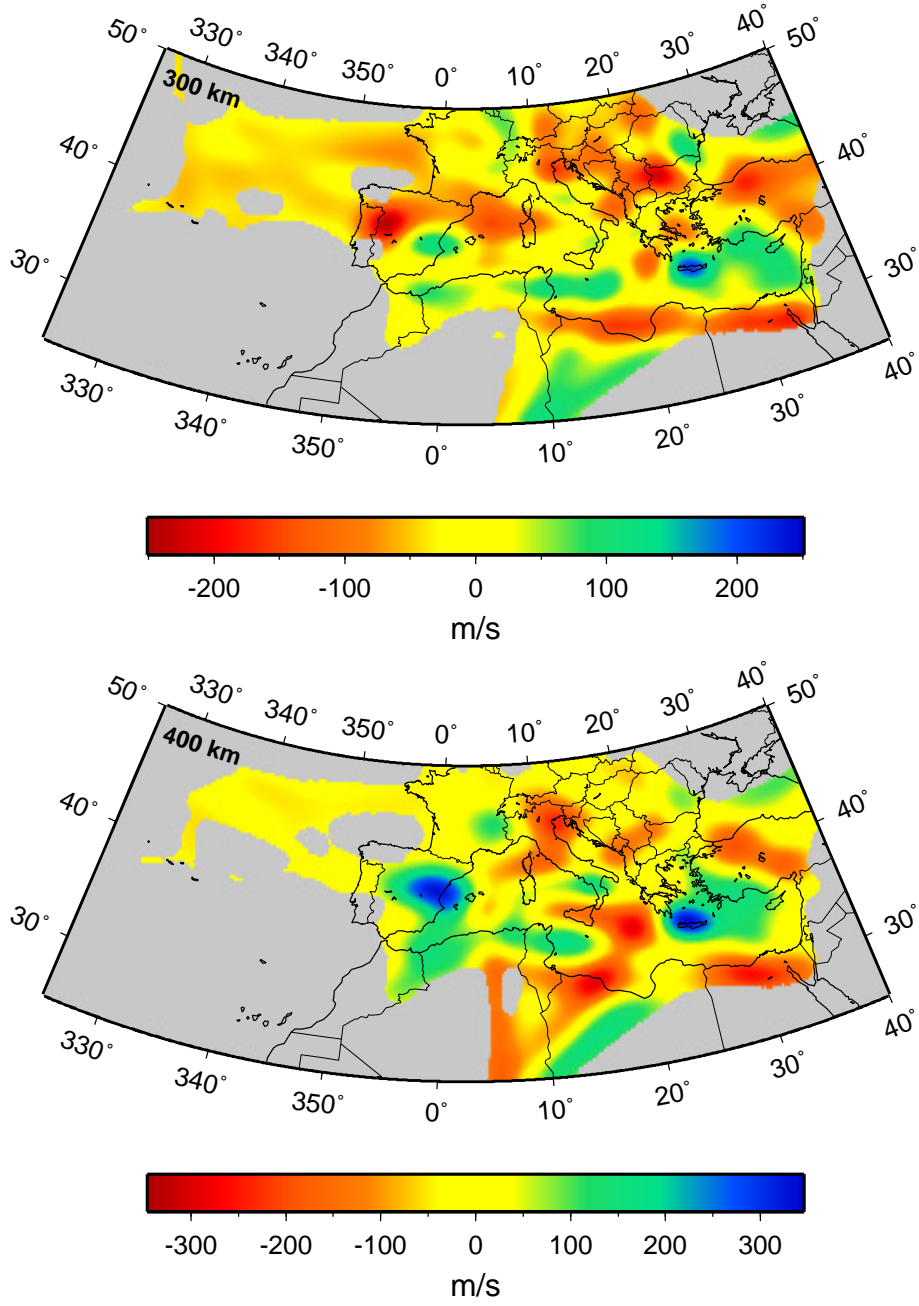
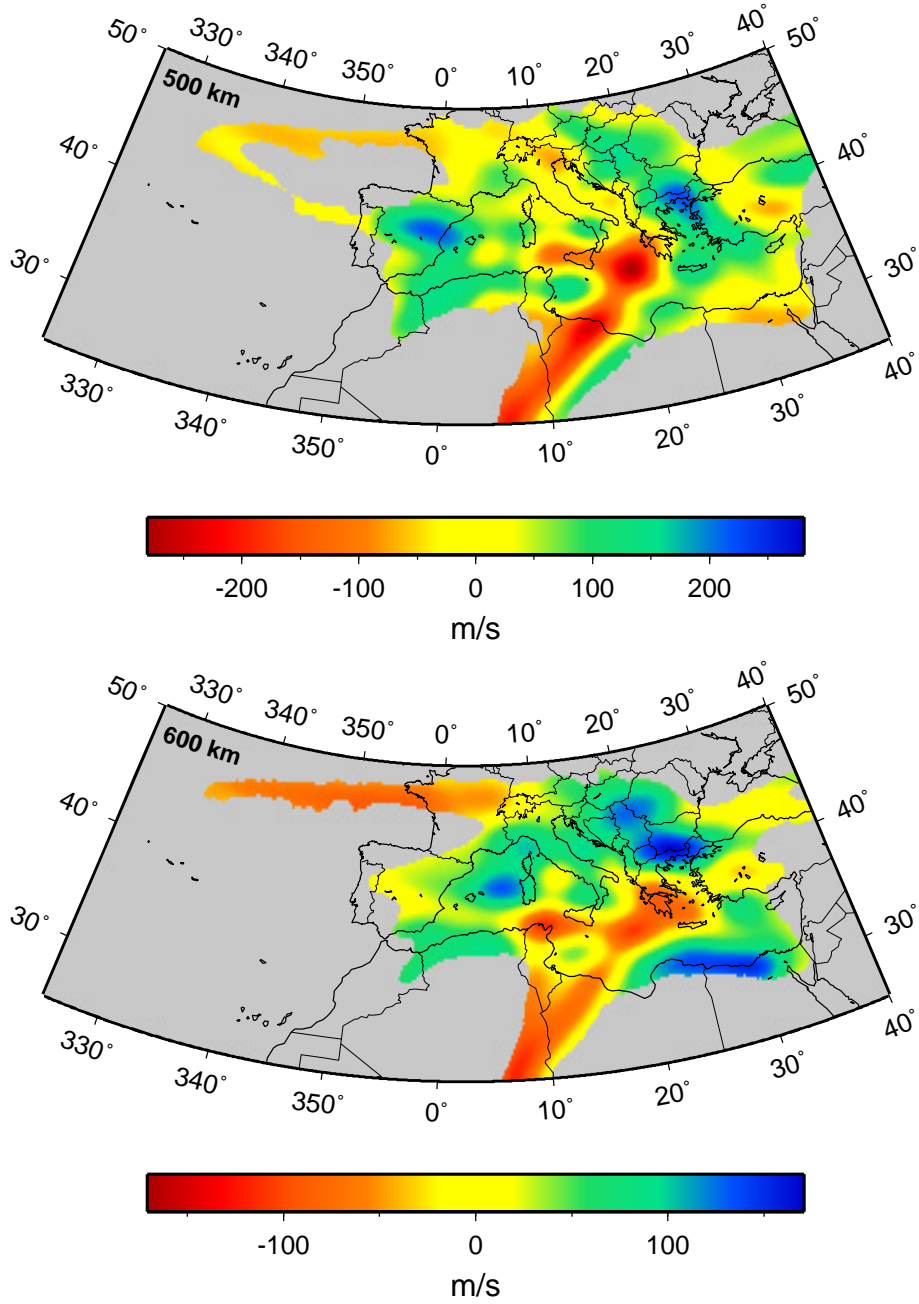
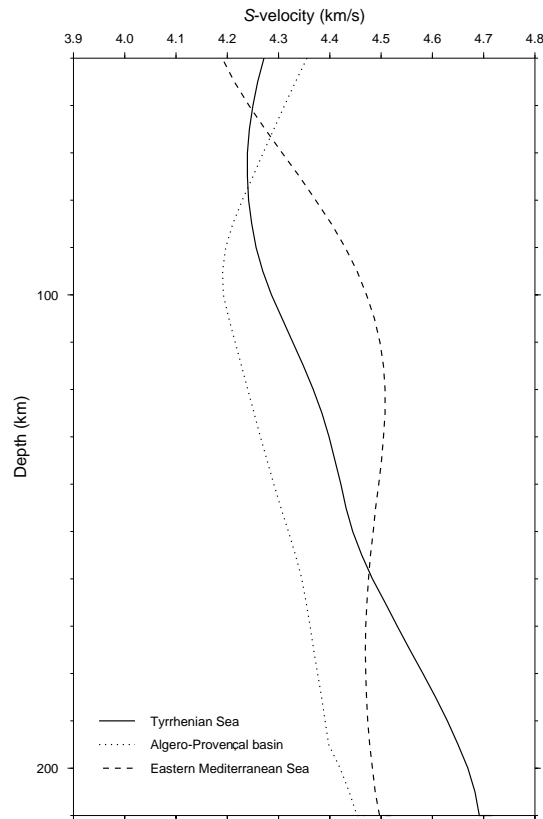


Figure 4.11: (continued)



**Figure 4.11:** (continued)



**Figure 4.12:** 1D  $S$ -velocity models computed by averaging the velocity structure beneath the Algero-Provençal Basin, the Tyrrhenian Sea and the eastern Mediterranean Sea.

#### 4.6.1 Mediterranean Sea

The Mediterranean Sea exhibits strong lateral variations in crustal (Marone et al., 2003b) and upper mantle structure (Fig. 4.11), confirming different origin and evolution of the western and eastern parts.

The western Mediterranean Sea, in particular the Algero-Provençal Basin, is underlain by average to high velocities in the uppermost 80 km. Between 80 and 200 km,  $S$ -velocities as low as 4.2 km/s are the indication for an asthenospheric layer. Deeper, average  $S$ -velocities for the Mediterranean region (4.6-4.8 km/s) are mapped. The lithosphere-asthenosphere system present beneath the Algero-Provençal Basin can also clearly be seen in a 1D average  $S$ -velocity profile (Fig. 4.12). A similar velocity profile is also observed for the Tyrrhenian Sea. However, higher velocities have been found below 100 km due to the presence of high velocity subducted material beneath the Apennines and the Calabrian arc.

Both the horizontal as well as the vertical extent of the imaged features is well resolved

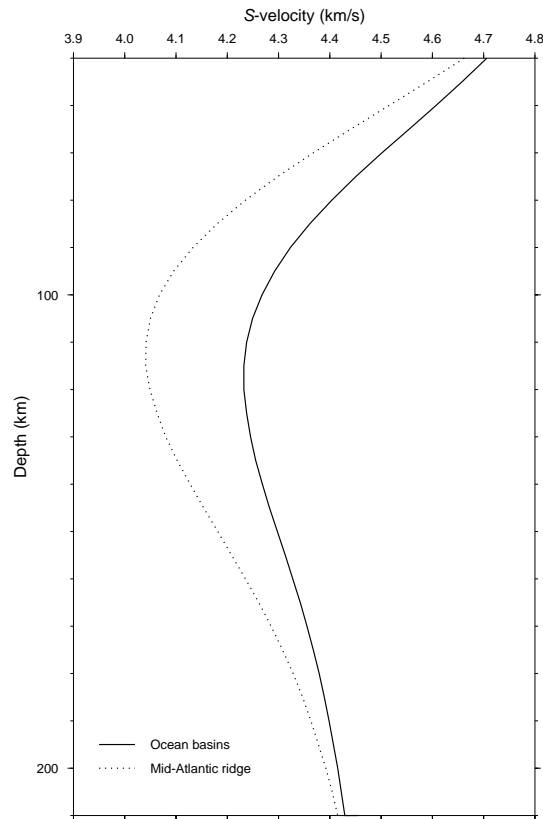


**Figure 4.13:** 1D  $S$ -velocity models computed by averaging the velocity structure beneath the ocean basins and the Mid-Atlantic ridge.

down to 300 km (Fig. 4.6). The low  $S$ -velocity layer between 80 and 200 km is also present in the results of Zielhuis & Nolet (1994), while  $P$ -velocity models (Piromallo & Morelli, 2003; Spakman et al., 1993) show a more diffuse zone, both in horizontal and vertical directions. This is likely due to different wave path coverage and lower sensitivity of  $P$ -waves to this structure.

The lithosphere-asthenosphere system of the western Mediterranean Basin clearly differentiates itself from the structure of the older (23-84 Ma) eastern Atlantic Ocean (Fig. 4.13): significantly lower  $S$ -velocities down to 150 km as well as a thinner lithosphere ( $\sim 80$  km) characterize this region. Differences compared to the structure of a young ocean are also observed. Besides a narrower  $S$ -velocity minimum around 95 km depth and a smaller velocity gradient for the lithosphere, the western Mediterranean Basin also shows higher velocities (at least 0.1 km/s) between 120 and 200 km depth than an oceanic structure of comparable age (Nishimura & Forsyth, 1989). Its structure is also significantly different from the average velocity structure mapped at the Mid-Atlantic ridge, where the imaged

velocities are almost 0.2 km/s lower.

The imaged *S*-velocity structure beneath the western Mediterranean confirms that, rather than a young ocean, this basin could be a strongly stretched continent, partly affected by “back-arc” spreading, formed at the back of the NW subducting African oceanic lithospheric slab between  $\sim 30$ -22 Ma. The measured high heat flow (Burrus & Foucher, 1986), the proposed reduced densities (Yegorova et al., 1998) and the found low *S*-velocities suggest that warm asthenospheric material could be present at shallow depth beneath the western Mediterranean. Water, possibly brought into the upper mantle by subduction of oceanic lithosphere, could play a role in decreasing the *S*-velocities (Thompson, 1992).

The Central Mediterranean, i.e. the area between southern Italy, Greece and Libya, is characterized by a sharp transition in *S*-velocity structure from north to south (Fig. 4.11). This is especially evident in the uppermost mantle (50-150 km), where *S*-velocities as high as 4.8 km/s offshore Greece change abruptly to average *S*-velocities for the Mediterranean Sea (4.4 km/s) along a line connecting Sicily to Benghazi (Libya). As deep as 200 km this abrupt velocity variation disappears and the entire region shows slightly low velocities (4.3 km/s).

The imaged and resolved (Fig. 4.6) structure correlates with the sea floor topography (Fig. 4.1). In fact along the line connecting Sicily to eastern Libya an escarpment with steep slope (Malta escarpment) has been mapped at the sea bottom surface. A similar feature has also been observed in the Moho topography (Marone et al., 2003b). This transition in uppermost mantle *S*-velocities, in crustal thickness and the escarpment at the surface could represent a suture zone between two blocks of different origin: deep oceanic basins (Ionian and Sirte Basins) to the north and a continental platform to the south (Dercourt et al., 1986).

The eastern Mediterranean is underlain by a complete different structure compared to the western part (Figs. 4.11 and 4.12), implying a different origin and evolution of the two regions. The most striking difference is the absence, in the east, of a low velocity layer between 100 and 200 km. On the contrary, average to high *S*-velocities at these depths have been imaged. Between 150 and 200 km, low *S*-velocities are mapped beneath Cyprus and the Turkey-Syria border region. No evidence of subducting or subducted material along the Cyprus arc is present.

Synthetic tests (Fig. 4.6) show that we can rely on the imaged structure as deep as 300 km. However, the upper mantle structure down to 80-90 km could be bias by unmodeled, exceptionally low velocities in the upper crust due to up to 14 km thick layers of sediment. At 50 km depth, the *S*-velocity e.g. just north of the Nile delta is underestimated by at least 0.1 km/s. Compared to previous *S*-velocity models (e.g. Zielhuis & Nolet, 1994; Marquering & Snieder, 1996; Martínez et al., 2000), where only few paths crossing the eastern Mediterranean Sea have been included, we achieved a significant improvement.

However, due to inhomogeneous earthquake and station distribution the resolution for this region is not as good as for the western Mediterranean.

The structure characterizing the eastern Mediterranean (missing asthenospheric layer and average *iasp91* upper mantle *S*-velocities) suggests that this region is different from an oceanic basin or a strongly stretched continent. The imaged structure points to a continuation of the northern African continental lithosphere beneath the sea (Meier et al., 2003).

#### 4.6.2 Northern Africa

In previous studies about the plate boundary in the Mediterranean region, only few results exist for the African side. Hardly any broad band seismic station was installed along the northern African coasts and due to the uneven event distribution in the southern Mediterranean, the resulting path density was not high enough to achieve an acceptable resolution. The additional seismic stations installed in several northern African countries during the MIDSEA project (Van der Lee et al., 2001) are crucial to the resolving power we have achieved for this region.

Our model (Fig. 4.11) exhibits *S*-velocities as low as 4.1 km/s for northern Algeria at 100 km depth. This negative anomaly, which is well resolved down to 200 km (Fig. 4.6), is an extension of the asthenospheric layer imaged beneath the western Mediterranean Sea. The deeper structure (beneath 300 km) is dominated by a E-W striking high velocity (4.7-4.8 km/s) features. Its N-S extent is well resolved, while the E-W trending could be affected by smearing (Fig. 4.6). Nevertheless it can be concluded that, on average, the mantle at these depths is characterized by high shear wave velocities, possibly related to subduction processes occurred in the area during the early Miocene (Dercourt et al., 1986).

Tunisia is characterized by *S*-velocities higher than the average mean for the Mediterranean region at 100 km depth. This anomaly is reasonably well resolved but the resolution rapidly decreases south of, west of and below (> 150 km) it.

The resolution for the eastern part of the northern African margin is not as good as for the western part. Consequently, our model is close to the starting model of the 3D inversion and is not showing any significant feature in this region.

#### 4.6.3 Eastern Atlantic Ocean

The plate boundary between the African and the Eurasian continents continues west of Gibraltar in the Atlantic Ocean as far as the Azores triple junction.

The imaged *S*-velocity structure for the eastern Atlantic Ocean (Fig. 4.11) is quite homogeneous, showing high velocities at 75 km depth between 25°W and the European coasts, while at the same depth a negative anomaly is mapped beneath the Mid-Atlantic ridge and the Azores Archipelago. This low velocity feature is becoming more prominent at 100 km depth, while beneath the older oceanic basins average *S*-velocities are observed. At 150



km, the negative anomaly beneath the ridge and the Azores is still present. On average, slightly low velocities (4.3 km/s) at this depth are also imaged beneath the eastern Atlantic Ocean. Anomalously high velocities (up to 4.8 km/s) are imaged in the uppermost mantle beneath the Bay of Biscay. Isostatic studies (Marone et al., 2003b) suggest for this region lower densities than expected at this depth for an old ocean and they relate them to depletion. They also point to the possible Archean age of the lithospheric rocks in the Bay of Biscay.

Paths crossing the eastern Atlantic Ocean are generally longer than  $20^\circ$ . The path integral approximation used for the synthetics computation is satisfactory for the modelling of surface and body waves which bottom in the same depth range as the surface wave modes used. This condition is satisfied for both surface and body waves travelling for less than 2800 km, while this approximation is less accurate for larger epicentral distances because the 2D nature of the sensitivity kernel is ignored (Marquering & Snieder, 1996). Moreover, due to the shallow hypocenter depth of the earthquakes occurring at the Mid-Atlantic ridge, the excitation of high amplitudes higher modes is limited. These factors are restricting the use of higher modes for paths crossing the eastern Atlantic Ocean, thus reducing the imaging capability of our dataset deeper than 200 km.

A similar image of the uppermost mantle in the eastern Atlantic has been obtained by Silveira & Stutzmann (2002) from Rayleigh and Love waves phase velocities.

Because of low spreading rates of the Mid-Atlantic ridge (1 to 4 cm/year), the age of the ocean floor rapidly increases with distance from the ridge axis. Owing to predominant W-E direction of the seismic waves travelling through the oceanic region (Fig. 4.3), the retrieved velocity structure is averaged out in this direction, hindering accurate observation concerning the dependence of the mantle velocity structure on lithospheric age. Several average 1D *S*-velocity models for different latitude bands between  $40^\circ\text{N}$  and  $50^\circ\text{N}$  have been computed to study the N-S velocity variation. Confirming the structural homogeneity of the horizontal slices at different depths (Fig. 4.11), no significant trend in the computed 1D average models has been observed. Unfortunately a comparison between the upper mantle *S*-velocity structure north (Eurasian plate) and south (African plate) of the Azores-Gibraltar fracture zone is not possible, because of lack of resolution in the southern part.

#### 4.6.4 Europe

The eastern continuation of the plate boundary can be followed beneath central-southeastern Europe (Fig. 4.11). An almost continuous belt of high shear velocities (4.5-4.7 km/s) is imaged at 100 km depth beneath Italy, the Adriatic Sea, the Dinarides, the Peloponnesus and southern Greece. Deeper, these positive anomalies are limited to the Italian and Greek regions, while former Yugoslavia is characterized by slightly low *S*-velocities. High velocities are present continuously down to the transition zone only beneath Crete. This high velocity belt dominating the central-eastern European upper mantle is inter-

preted as African oceanic lithosphere subducting beneath the European plate, thereby marking the plate boundary.

Synthetic resolution tests show that the resolving power of our dataset for central and eastern Europe is very good (Fig. 4.6). Beneath Italy and Greece, the regions with the highest path density, small-scale heterogeneities, such as subducted lithosphere, are imaged. In some regions, reduced sensitivity of the modeled waveforms for structures between 300 and 400 km prevents the imaging of continuous subducting slabs down to the transition zone, as e.g. beneath southern Italy.

Existing *S*-velocity models (Zielhuis & Nolet, 1994; Marquering & Snieder, 1996) also show the presence of high-velocity anomalies along the suture zone. However, lack of resolution hinders any conclusion about slab geometry and continuity. The general features imaged in *P*-velocity studies (Spakman et al., 1993; Wortel & Spakman, 2000; Piromallo & Morelli, 2003) compare well with our model, even though the *P*-velocity anomalies are narrower due to different data and imaging characteristics.

More into details, our model for Italy shows a continuous high velocity anomaly from northern to southern Italy down to 300 km, interpreted as subducted lithosphere. Although synthetic tests indicate that both horizontal and vertical tears in the subducted body would be resolved by our dataset (see Appendix B, Figs. B.1-B.3), small gaps in the lateral continuity of the slab can not be excluded.

A high velocity body (4.7 km/s) has also been imaged beneath the Calabrian arc between 100 km and 300 km (Fig. 4.14(a)). In the transition zone beneath the Tyrrhenian and Provençal Basins, indication of seismically fast material is also present. The small deviations of the imaged velocity from the regional average (< 100 m/s) result from the strong underestimation of the anomaly amplitudes at these depths (see section 4.5). These features have been interpreted as the image of subducted Ionian lithosphere. The reduced thickness of this slab is close to the limits of the resolving power of our dataset. This is preventing us from imaging a continuous slab. Synthetic tests also show that anomalies with a size comparable to inter-nodes distance can hardly be detected and are sometimes introducing artefacts in the model. This is a possible explanation for the observed shift towards the Tyrrhenian Sea of the anomaly beneath Calabria.

The Hellenic arc shows lateral continuity from northern Greece all the way to the Turkish coasts (Rhodos island), while further to the east no anomalies interpretable as subducting lithosphere are present.

Beneath Crete, we imaged a continuous steep positive anomaly, however with variable amplitudes, from 100 km depth down to the transition zone (Fig. 4.14(b)). At 500 km depth, the slab is lying horizontally. Resolution tests show that the horizontal orientation of the imaged high velocity layer is resolved and is not an artefact due to horizontal smearing (see Appendix B, Fig. B.4).

Beneath the Peloponnesus and northern Greece, we image subducted fast Ionian litho-

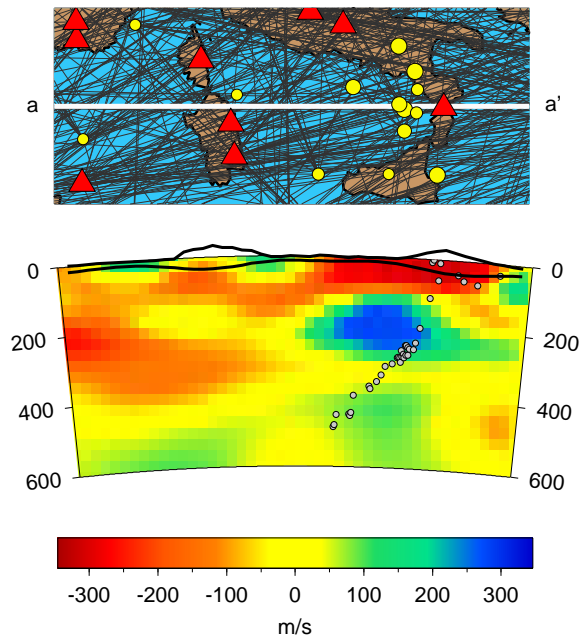


**Figure 4.14:** Vertical cross sections through our  $S$ -velocity model along the great circle segments shown in the map in Fig. 4.7 (a saturated color scale has been used to enhance structures in the transition zone, for the absolute values compare with Fig. 4.11) - (a) profile perpendicular to the Calabrian arc.

sphere down to 200 km. A positive anomaly is present also deeper, but between 300 and 400 km average  $S$ -velocities for the region are observed. A similar structure has also been imaged with body wave tomography (Wortel & Spakman, 2000). A good correlation exists between earthquake hypocenters from the catalogue of Engdahl et al. (1998) and the upper boundary of the subducting slab.

Other relevant features present in our model are low  $S$ -velocities between 100 km and 200 km depth beneath the Pannonian and the Moesian Basins, regions dominated by extensional tectonics. Between 75 and 100 km depth, a negative cylindrical anomaly is found also beneath the Massif Central, which we interpret as hot mantle material close to the surface. This is in agreement with the measured high heat flow (up to  $110 \text{ mWm}^{-2}$ ) (Cermák & Rybach, 1979).

#### 4.6.5 Iberian peninsula

In this study we included additional data from MIDSEA stations and Mid-Atlantic ridge earthquakes covering the Iberian Peninsula (Fig. 4.3), so that resolution for Spain has significantly increased (Fig. 4.6). Beneath the western part of the peninsula, we imaged

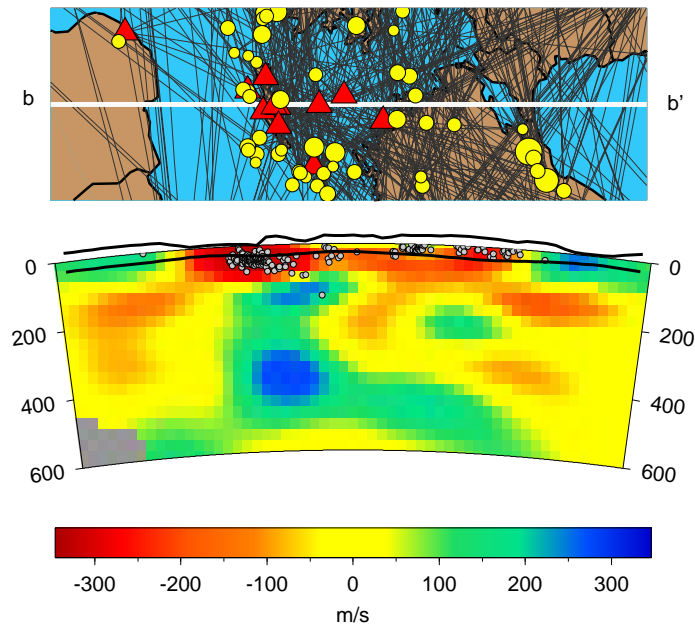


**Figure 4.14:** (b) Profile from northern Libya to the Black Sea.

(Fig. 4.11) low  $S$ -velocities (4.2 km/s) between 75 km and 300 km, while the eastern Iberian margin below 250 km is characterized by a strong positive anomaly (this high velocity feature is discussed further in section 4.7.2). The resolution of small-scale features beneath the Alboran region is restricted to the uppermost mantle, due to limited number of paths crossing the area (Fig. 4.3).

## 4.7 Discussion

### 4.7.1 Spreading ridges and old basins

Major structural differences in the eastern Atlantic Ocean are observed between the Mid-Atlantic ridge and the older oceanic basins (see section 4.6.3 and Fig. 4.11). In Fig. 4.13, 1D average  $S$ -velocity models for these two regions are shown. The mean velocity structure for the deep basins is characterized by a fast 80 km thick lithosphere, while a low velocity layer (4.3 km/s) is present between 90 and 130 km depth. The mean structure beneath the Mid-Atlantic ridge is on average 0.2 km/s slower down to 120 km depth. Our results confirm that the North Atlantic lithosphere is characterized by lower velocities beneath the spreading ridge than under the old ocean basins as observed in regional 3D models obtained using surface wave phase velocities (e.g. Mocquet & Romanowicz, 1990; Silveira & Stutzmann, 2002) or  $S$ -wave travel times (e.g. Grand, 1994). Comparison of the average 1D upper mantle structures with results for the Pacific Ocean obtained

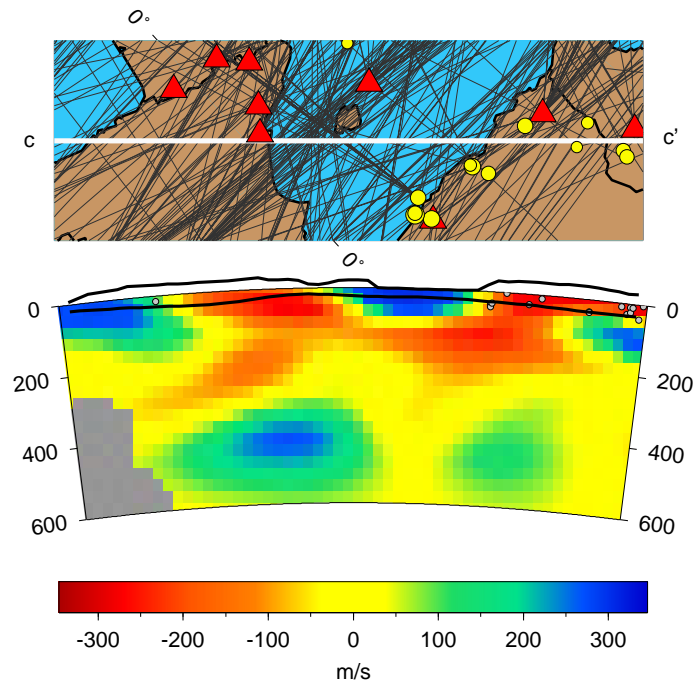


**Figure 4.14:** (c) Profile from northern Spain to northern Algeria.

e.g. by Nishimura & Forsyth (1989) shows that on average the eastern Atlantic Ocean is characterized by higher  $S$ -velocities down to a depth of 150 km for areas of a similar age. Despite strong differences observed in the crustal structure between the Mid-Atlantic ridge and the Azores (Marone et al., 2003b), EAV03 does not reveal significant differences in the upper mantle  $S$ -velocity structure. However, due to the limited resolution of our dataset in this region, we can not exclude that the Mid-Atlantic ridge and the Azores distinguish themselves not only in the crustal but also in the upper mantle structure. With the current extension of the MIDSEA broadband network towards the west (Van der Lee et al., 2001; Silveira et al., 2002), availability of high quality data for the westernmost part of the Eurasia-Africa plate boundary significantly increased, giving the opportunity to obtain a better constrained model for this region.

#### 4.7.2 Slab fragments in the western Mediterranean

EAV03 adds new information for a better understanding of the western Mediterranean evolution. In particular, we have mapped a high velocity anomaly beneath eastern Spain between 250 and 500 km depth, which could be related to the early stage of subduction in the western Mediterranean (Fig. 4.14(c)). Although resolution tests show that the shape of this feature is affected by smearing, the existence of the heterogeneity is resolved (see

Appendix B, Fig. B.5). At similar depths, a positive anomaly, E-W trending, has also been found beneath northern Algeria. Although this feature could have been smeared in a coast-parallel direction, its N-S extent is well resolved.

The strongest high velocity heterogeneity imaged in *P*-velocity models (e.g. Blanco & Spakman, 1993) beneath Spain is located more south than in our model, beneath the Alboran Sea and the Betic Cordillera. West of the Balearic islands a significant positive anomaly, however limited in size, is visible only around 500 km. The deep upper mantle structure beneath northern Algeria imaged by body wave tomographic models is also characterized by high velocities, however localized only in northeastern Algeria and Tunisia.

While different tomographic models and tectonic reconstructions agree on the northern African anomaly representing detached subducted oceanic lithosphere, the processes involved in the evolution of the eastern Iberian peninsula are still a matter of debate.

NW subduction of oceanic lithosphere along the eastern Spanish coast began about 80 Ma ago as consequence of the continuous Africa-Eurasia convergence (Dercourt et al., 1986). First evidences of trench migration and back-arc extension date back 30 Ma (Faccenna et al., 2001). We suggest that the deep imaged high velocity body west of the Balearic islands could be a fragment of this subducting slab, which detached in an early stage of the subduction. Presence deep beneath eastern Spain of subducted oceanic lithosphere, probably originally rich in water, is consistent with the work of Van der Meijde et al. (2003a) showing evidence for water at 400 km depth beneath this region. However, time and origin of this event are still unclear. For instance, as suggested by Zeck (1999), the slab could have been segmented in three distinct arcs separated by transform faults. Such development of the subduction system may have been controlled mainly by the variable nature of the subducting Tethyan lithosphere and the shape of the Iberian continental plate. A lithospheric fragment could have partly or completely detached from a slab edge and sunk down to the transition zone. This event could be at the origin of the unusual evolution of the Valencia trough: rifting in this extensional basin began during late Oligocene-early Miocene and then suddenly failed (18 Ma) (Watts & Torné, 1992). Owing to the composite nature of the subducting oceanic lithosphere, it is also plausible that the imaged high velocity anomaly is detached from the surface due to the subduction of a small ridge. This suggests that subduction of oceanic lithosphere along the eastern Iberian margin could have come to an end. A new subduction arc could have initiated later further east. Although more investigation is needed to understand mechanisms and chronology, the new image of the eastern Iberian upper mantle could represent a new key element for the reconstruction of the western Mediterranean history.

### 4.7.3 Transition zone

Including body waves in our waveform fitting, which however do not bottom in the mantle beneath the realm of the surface wave modes, has provided sufficient resolution to

image the gross-scale structure in the transition zone beneath the studied region (Fig. 4.6) and prevents from the tendency for the sign of the heterogeneities to reverse with depth due to the neglect of surface wave mode coupling (Marquering & Snieder, 1996). While the Mediterranean uppermost mantle is dominated by low rigidity material, the picture changes dramatically in the transition zone, where extensive positive anomalies are imaged (Fig. 4.11). We observe high velocities in the transition zone beneath the western Mediterranean Basin, Italy, the Alps, the Pannonian Basin and eastern Europe. Low rigidity material is found in the central Mediterranean Sea and the Hellenic arc. A similar pattern has been imaged in body wave tomographic studies (e.g. Spakman et al., 1993; Wortel & Spakman, 2000; Piromallo & Morelli, 2003). The imaged seismically fast structure has been interpreted as cold subducted African lithosphere, which did not penetrate into the lower mantle and lies horizontally in the transition zone. The deep structure at the edge of our model and in particular beneath northern Africa is not well constrained and is strongly influenced by horizontal smearing along the main path directions (Fig. 4.6).

## 4.8 Conclusions

We present the first regional study resolving the Eurasia-Africa plate boundary region from Azores to the eastern Mediterranean Sea. The resolution of existing velocity models has been complemented by the temporary deployment of 25 broad band seismic stations (MIDSEA project) along the suture zone and by using new *S*- and surface waveforms recorded at permanent European seismic stations.

Striking similarities for the extensively studied continental European region between our shear wave velocity model and body wave tomographic images (e.g. Bijwaard & Spakman, 2000) have been observed. As expected, due to smoothing and different data characteristics, the imaged heterogeneities in our model show a longer wavelength character compared to *P*-velocity models. However, where the resolving power of the used dataset is good, body and surface wave tomography studies (independent data with different sensitivity) show consistent results. This is giving further confidence to our *S*-velocity model for regions poorly studied before, where we could achieve an unprecedented resolution, like in particular for the shallow mantle beneath the Mediterranean Sea, northern Africa and the eastern Atlantic Ocean.

Our *S*-velocity model shows the same order of complexity as observed at the surface: the imaged heterogeneities in the Mediterranean upper mantle correlate with the tectonics and geology along the plate boundary. The Eurasia-Africa suture zone manifests itself in the upper mantle mainly as a belt of high-velocity material representing subducted oceanic lithosphere. It can be followed as deep as 300-500 km, depending on the region and resolution. Since subduction did not occur contemporarily throughout the region and sinking velocities are not necessarily spatially homogeneous, fragments of African lithosphere reside at different depths in the upper mantle. Where the process is still active (e.g. Crete), a continuous positive anomaly is observed from the surface down to the transition zone. At

old subduction zones (e.g. Spain), detached pieces of seismically fast material are imaged deeper than 250 km.

In particular a new resolved feature of our *S*-velocity model is a positive anomaly imaged beneath eastern Spain between 250 and 500 km depth. We suggest that this fast body could be a fragment of subducted lithosphere, which detached in an early stage of NW subduction of oceanic lithosphere in the western Mediterranean.

Not only convergence has been recorded in the upper mantle, but also extension has its own signature beneath the Mediterranean. This is particularly clear for the Algero-Provençal and Tyrrhenian Basins, where a shallow asthenospheric layer is observed.

The lithosphere-asthenosphere system of the western Mediterranean clearly differentiates itself from the structure of the older eastern Atlantic Ocean. Differences compared to the structure of a 4 to 20 Ma old ocean are also present. These observations support the idea that, rather than a young ocean, the western Mediterranean could be a strongly stretched continent, partly affected by spreading, formed at the back of a slab. The structure characterizing the eastern Mediterranean (missing asthenospheric layer and average *iasp91* upper mantle *S*-velocities) suggests that this region is different from both an oceanic basin and a strongly stretched continent. The imaged structure points to a continuation of the northern African continental lithosphere beneath the sea.

Major structural differences in the eastern Atlantic Ocean are imaged between the Mid-Atlantic ridge and the older oceanic basins: the North Atlantic lithosphere is characterized by lower velocities beneath the spreading ridge than under the old ocean basins.

Beneath northern Africa, we imaged detached subducted lithosphere beneath northern Algeria.

In summary, EAV03 is characterized by strong contrasts between the transition zone and uppermost mantle structure. High velocity anomalies related to fragments of subducted lithosphere have been imaged in the transition zone throughout the Mediterranean region and document its long history of subduction. The structure of the uppermost mantle is instead dominated by rapidly laterally varying low velocity anomalies, witnessing the complex tectonic evolution of this region.



# Love and Rayleigh wave incompatibility

---

Although current applications of the Partitioned Waveform Inversion (PWI) (e.g. Nolet, 1990; Van der Lee & Nolet, 1997) only make use of Rayleigh waves, this inversion method can also be applied to retrieve information on the upper mantle velocity structure from Love waves. Using the PWI formalism, Rayleigh and Love waveforms can even be jointly fitted.

We applied PWI in the Eurasia-Africa suture zone to retrieve the 3D crustal and upper mantle  $S$ -velocity structure (Marone et al., 2003a,b). In particular, we modeled fundamental and higher mode waveforms of both Rayleigh and Love waves. The structure information we gained, is however suggesting that it cannot be assumed that Love and Rayleigh waves are sensitive to the same structures in a comparable way, but rather that major differences exist, which should be understood before combining these two types of waves in the same inversion.

## 5.1 1D path average velocity models

We determined the 1D average  $S$ -velocity structure and Moho depth along wave paths by nonlinear waveform fitting of wave trains composed of fundamental and higher mode surface waves. We considered Rayleigh and Love wave trains with a good signal-to-noise ratio and azimuth away from fundamental mode wave source radiation nodes. Although a satisfactory fit for individual waveforms (Rayleigh or Love) using a realistic 1D veloc-

ity model could often be obtained (Fig. 5.1), it was never possible to fit both Love and Rayleigh waves travelling along the same path with a single velocity model (Fig. 5.2). To better understand this phenomenon we performed several tests, excluding that the observed discrepancy in the 1D path average velocity models retrieved from Rayleigh and Love waves is determined by methodology choices. We also show that the observed incompatibility of the velocity models is not an artefact due to unmodeled scattered energy in the data or uncertainties in event parameters.

### 5.1.1 Influence of methodology choices

#### Misfit definition

In this study, average 1D  $S$ -velocity models, for which synthetic seismograms best fit observed waveforms, are obtained by minimizing the following objective function  $F(\gamma)$  (Nolet, 1990; Van der Lee & Nolet, 1997):

$$F(\gamma) = \int w^2(t) [\mathbf{R}d(t) - \mathbf{R}s(t, \gamma)]^2 dt \quad (5.1)$$

where  $d(t)$  is the recorded and  $s(t, \gamma)$  the synthetic seismogram, which depends on the model parameters  $\gamma$ .  $\mathbf{R}$  is a filtering and windowing operator and  $w(t)$  a weighting function designed, using the inverse of the signal envelope, to enhance the contribution to the misfit of the higher modes with respect to the naturally dominating fundamental mode. The 1D average velocity model obtained for every single path is robust and does not depend on the choice of the windowing and filtering parameters. We further tested the robustness of the results of the nonlinear waveform fitting procedure by using two different objective functions. The first one, in addition to the difference between observed and synthetic waveforms (eq. 5.1), also minimizes the misfit between their dispersion curves. Depending on the relative weighting of the two contributions, a different fit of the higher modes waveforms was obtained, which was however not significantly influencing the retrieved velocity models. The fit obtained by jointly inverting Love and Rayleigh waves was also in this case not satisfactory. A single velocity model compatible with both Love and Rayleigh waveforms was also in this case not realistic. A second approach is based on a frequency dependent misfit, computed as the sum of the waveform misfits obtained in different frequency windows defined by consecutive closely spaced filters (multiple filtering) (Lebedev, 2000). Similar average  $S$ -velocity models have been obtained as by using the traditional misfit definition (eq. 5.1) and the discrepancy between models obtained with Rayleigh and Love waves could, also in this case, not be explained.

#### Model parameterization

The average  $S$ -velocity perturbations along the path between source and receiver are expressed in terms of a number of basis functions, which are chosen as a mix of boxcar

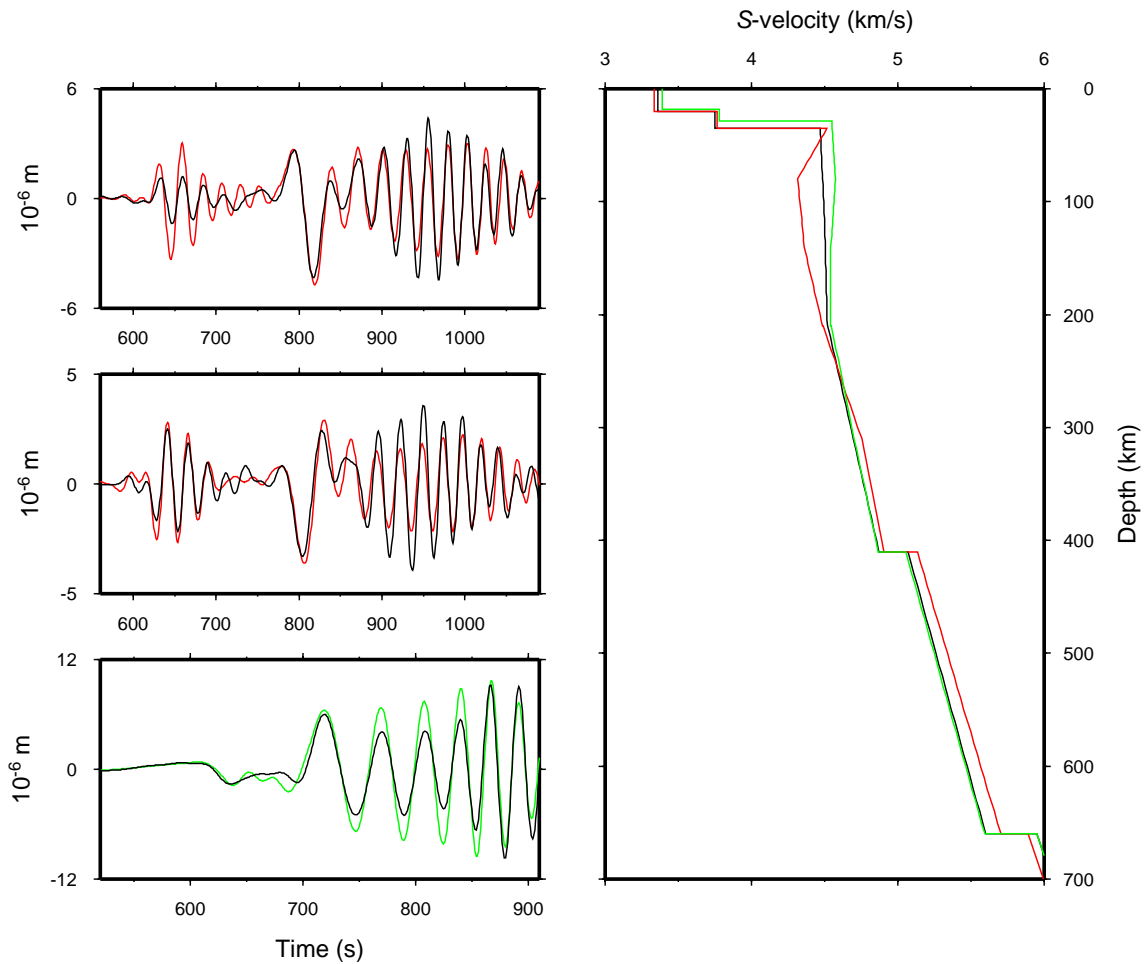


**Figure 5.1:** Waveform fitting results for the event in Egypt on November 23, 1995 recorded at the station TAM in Algeria. Rayleigh and Love waves have been inverted separately. On the left the observed waveforms (black lines, vertical, radial and transverse component from top to bottom) together with synthetic seismograms (red for Rayleigh, green for Love) computed with the corresponding 1D path average velocity models (shown on the right with iasp91 for comparison).

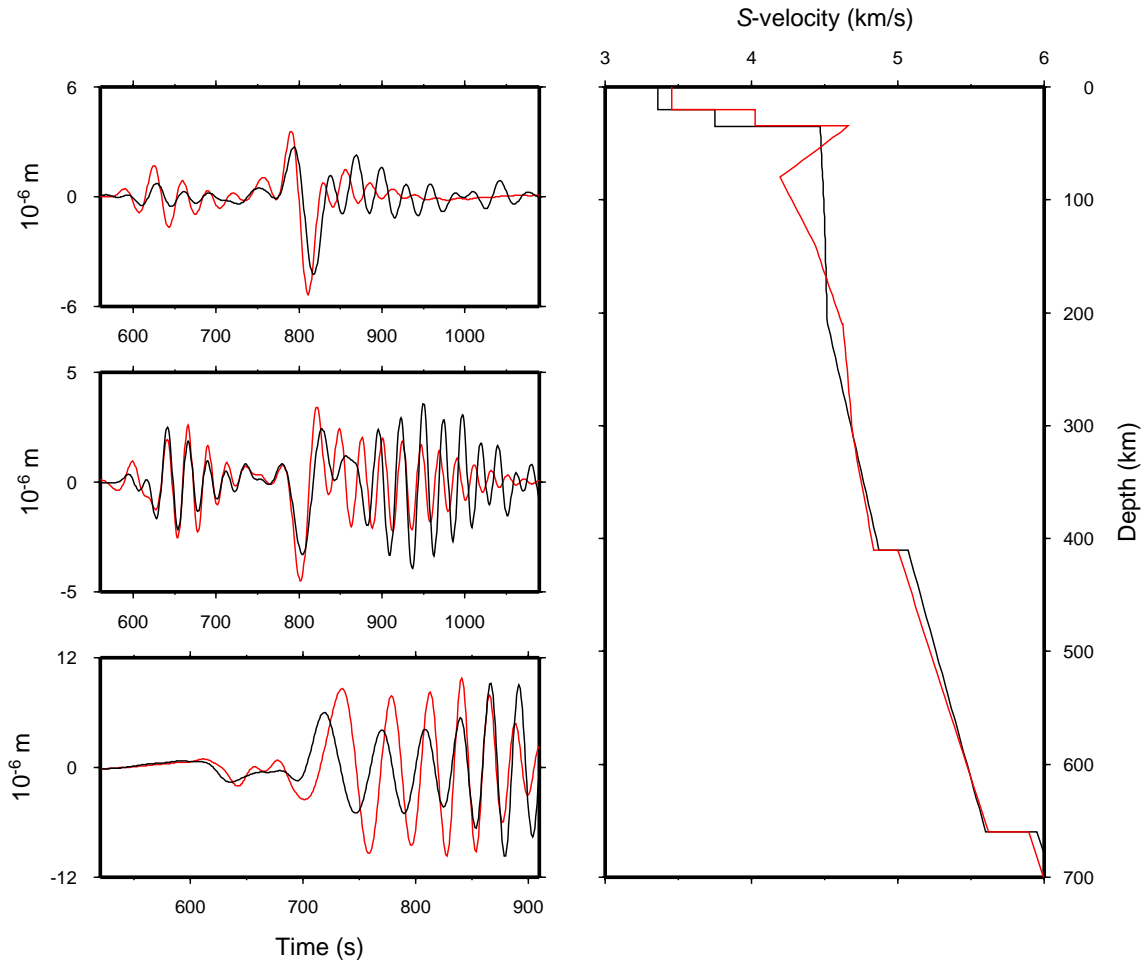


**Figure 5.2:** Waveform fitting results for the event in Egypt on November 23, 1995 recorded at the station TAM in Algeria. Rayleigh and Love waves have been jointly inverted. On the left the observed waveforms (black lines, vertical, radial and transverse component from top to bottom) together with synthetic seismograms (red lines) computed with the obtained 1D path average velocity model (shown on the right with iasp91 for comparison).

and triangular functions in order to incorporate both discontinuities and gradients in the model. Theoretically, it is always possible to fit a seismogram, if an infinite number of model parameters is allowed, but the resulting velocity model can be highly unrealistic. In spite of a finer parameterization (number of parameters doubled), the joint inversion of the 3 component seismograms did not result in any satisfactory waveform fit. In general, the retrieved 1D velocity models showed unrealistic strong gradients.

### ***P*-velocity and density structure**

The sensitivity of surface waves to *P*-velocity and density is much smaller than to *S*-velocity. However, to exclude any influence of these parameters on the observed incompatibility between data with primary sensitivity to  $v_{SH}$  and to  $v_{SV}$ , inversion runs have been performed, where *P*-velocities and density structure have been included as independent parameters. While inverting also for density perturbations did not significantly improve the waveform fit and modify the obtained 1D velocity models, including *P*-velocity as an independent parameter in the joint inversion of 3 component seismograms led to a satisfactory waveform fit. The obtained *P*-velocity model shows however unrealistic large perturbations with opposite sign compared to the retrieved *S*-velocity structure.

### **5.1.2 Influence of uncertainties in source parameters and unmodeled physical processes**

#### **Source parameters**

Van der Lee (1998) showed that, for the combination of path lengths and frequencies we are interested in, epicentral variations resulting from the use of source coordinates from different catalogues are negligible factors in the waveform inversion. However, depending on focal geometries, depth will control both amplitude and phase excitation of the various overtones building the seismogram. Moreover, a change in depth may move the source across the Moho discontinuity, thus strongly affecting the excitation. Although an incorrect source depth could result in an unsatisfactory waveform fit, inversion runs for single paths with an artificially modified event depth between 5 and 40 km, showed that depth uncertainties are however not responsible for the discrepancy between the average models obtained from Love and Rayleigh waves.

The excitation factor used for the computation of the synthetics can also be affected by uncertainties in the source mechanism. Source radiation patterns for Love and Rayleigh waves are often complementary: azimuths with maximum energy radiation for one type of wave correspond to source radiation nodes for the other. Therefore, for most simultaneous inversions of Rayleigh and Love waveforms, the fit is dominated by the wave with the highest energy radiation. Slight errors in orientation of the source mechanism could cause a large difference in the excitation factor used for the synthetics computation, especially for azimuths close to radiation nodes. However, tests show that rotation of the source

mechanism up to  $10^\circ$  mainly influences the synthetic amplitudes, while the retrieved path average velocity model is not significantly affected.

### Scattered energy

Due to the strong heterogeneous upper mantle velocity structure in the Mediterranean region (Marone et al., 2003a), the amount of scattered energy on the recorded seismograms can be large (Zielhuis & Nolet, 1994). Theoretical studies (e.g. Wang & Dahlen, 1995) suggest that scattering affects both phase and shape of the waves, translating into errors in the results.

To study how scattered energy influences a seismogram and, in particular, how neglecting it by using the phase-integral approximation affects the obtained velocity model, we performed synthetic tests. We computed synthetic seismograms with different amounts of scattered energy from scatters at different locations. We used the same source and path parameters as for regional seismograms recorded in the Mediterranean region, for which no velocity model could be found, explaining both Love and Rayleigh waveforms, although the radiation pattern was optimal for simultaneously fitting the two types of waves. Independently from the strength of the scattered energy, it was always possible to jointly fit the 3 component seismograms, recovering a 1D  $S$ -velocity model not significantly different from the input structure. Thus, we exclude that the observed discrepancy in the models obtained from Love and Rayleigh data results from unmodeled scattered energy in the seismograms.

#### 5.1.3 Anisotropy

The uppermost mantle velocity structure retrieved from Rayleigh data is consistently slower (up to 4%) than velocities obtained from Love wave data. Comparing the average  $S$ -velocity models obtained by separately inverting Love and Rayleigh waveforms with the global anisotropic model PREM (Dziewonski & Anderson, 1981), we observe a strong analogy. This suggests that the observed incompatibility between the velocity models obtained with the two datasets, at least in part, is due to radial anisotropy in the Mediterranean upper mantle.

## 5.2 3D upper mantle velocity models

Due to the observed incompatibility between 1D average path velocity profiles obtained from Love and Rayleigh waves, it was not recommendable to jointly invert the two sets of linear constraints, at least not in the PWI isotropic framework. Useful information could instead be gained from the comparison of 3D velocity models obtained from the inversion of homogeneous datasets. The upper mantle  $SV$ -velocity model obtained from the inversion of linear constraints provided by analysis of Rayleigh waves is extensively

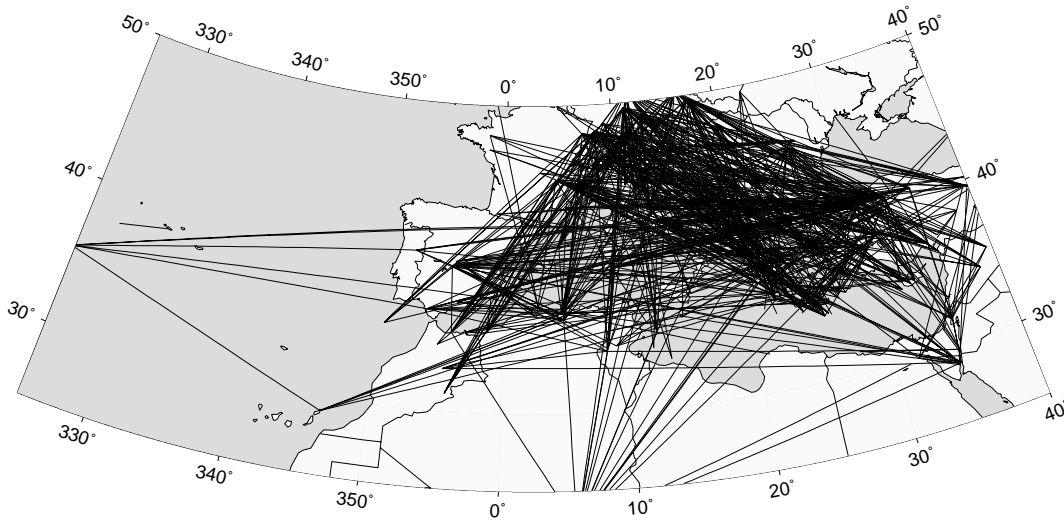


**Figure 5.3:** Great circle wave paths for the transverse seismograms which provided linear constraints.

presented in Marone et al. (2003a). The inversion of linear constraints provided by Love waves and the resulting 3D *SH*-velocity model show major differences compared to the Rayleigh waves case, which are extensively discussed in the following paragraphs.

The data coverage obtained with wave paths for analysed transverse component seismograms is restricted to a smaller region than for Rayleigh waves (Figs. 5.3 and 4.3). A comparable path density as for the Rayleigh case is observed only for the northern Mediterranean Basin, central and eastern Europe. We would expect the *SV*- and *SH*-velocity models for these regions obtained from analogous inversions with same damping and smoothing parameters to show similar characteristics (e.g. horizontal resolving power and size of the retrieved anomalies). Comparison of horizontal sections through the models (Figs. 5.4 and 4.11) shows that this is however not the case. Besides the expected higher *SH*-velocities in the uppermost mantle, as observed in the 1D path average velocity structures, and reduced resolution of Love waves beneath 200 km, the size of the imaged velocity anomalies is on average larger for the *SH*- than for the *SV*-velocity model. Additionally, correlation of the uppermost mantle anomalies retrieved from Love waves with surface geology and tectonic processes is not straightforward: the tomographic images are mainly dominated by broad high velocity anomalies (Fig. 5.4) not directly related e.g. to subducted lithosphere. The asthenospheric layer beneath the western Mediterranean is hardly detected and low velocity anomalies associated with extensional basins (e.g. Pannonian Basin) are not present (compare Figs. 5.4 and 4.11).

Differences are not limited to the retrieved velocity models, but are also observed for the convergence and variance reduction of the inversion. Although the system of linear equations provided by Love waves is smaller, more iterations are necessary for the inversion

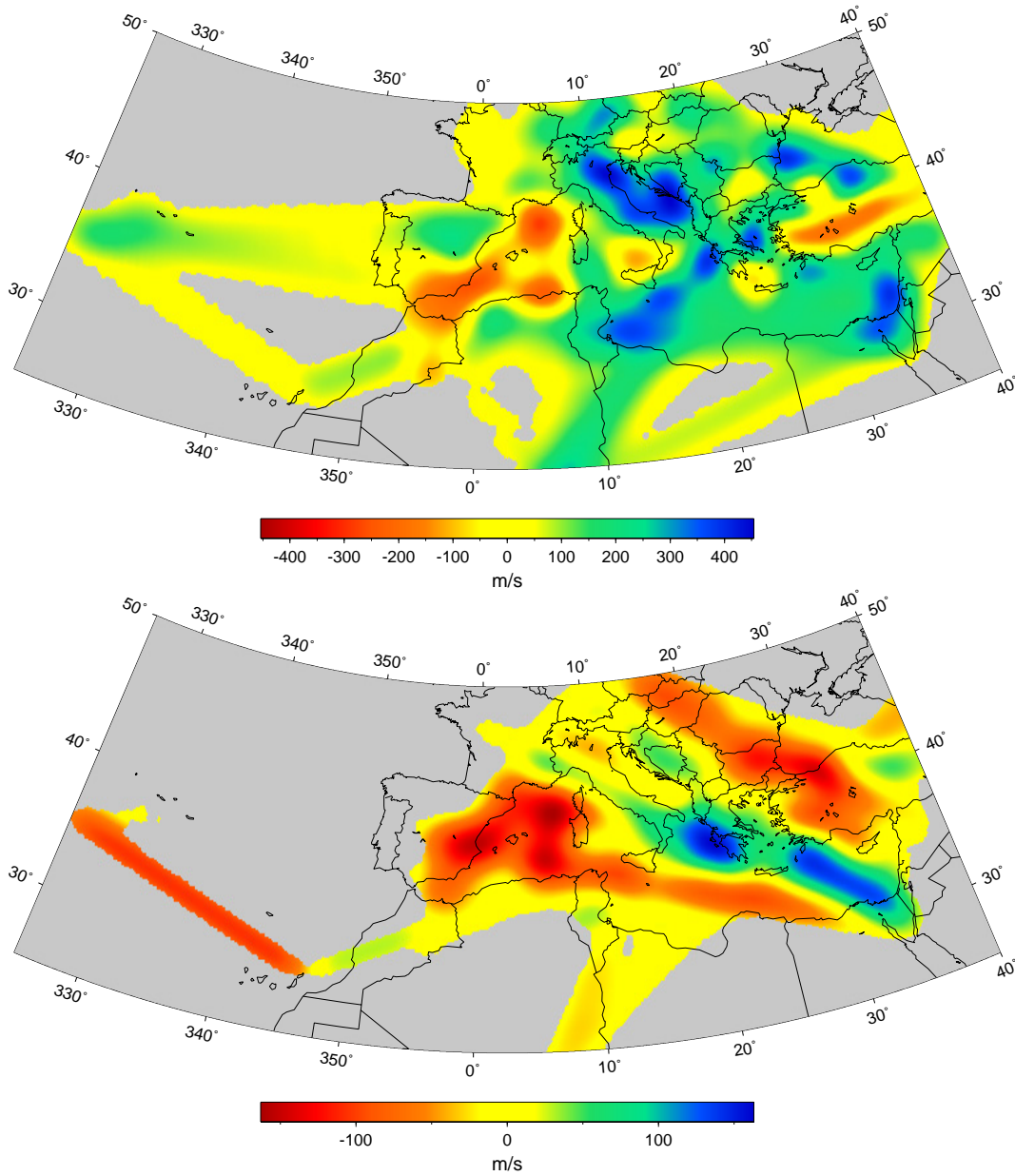


**Figure 5.4:** Horizontal slices at 100 km (top) and 200 km (bottom) depth through the S-velocity model obtained from inversion of Love waves data.



to converge and the achieved variance reduction is smaller. In theory, if the number of constraints is reduced, the inversion should converge earlier and a better variance reduction should be achieved. In practice, the inversion of the Love dataset shows that the constraints obtained by the analysis of the Love waves might be more inconsistent among each other compared to the constraints in the Rayleigh dataset.

We are actually not only inverting for the  $S$ -velocity structure, but also for Moho depth. To reduce trade-offs between Moho depth and velocity structure around it, which are inherent in surface waves used here, independent estimates of Moho depth have been added in the inversion (Marone et al., 2003b). To investigate the possible influence of trade-offs between crustal thickness and sub-Moho mantle velocities in regions not constrained by point measurements of the Moho depth, we performed an inversion of the Love dataset, with the Moho depth fixed at the values of EAM02 (Marone et al., 2003b). The obtained 3D velocity model shows significant differences only down to 80 km beneath southeastern Europe, where the Moho depth resulting from the joint inversion of linear constraints and independent Moho depth estimates is unrealistically small ( $< 20$  km). This is also the region, for which no independent point constraints have been added. This indicates that Love waves alone cannot uniquely determine Moho depth and velocities around it. Additional evidence comes from the increased variance reduction and early convergence achieved in the inversion with fixed Moho depth, despite the larger size of the system of equations. Although by fixing the Moho depth, inconsistencies in the dataset have been reduced, the characteristics of the retrieved model have not significantly changed.

In the following sections, we study in more details the sensitivity of Rayleigh and Love waves to upper mantle structures, to better understand possible differences in the information contained in these two types of waves.

### 5.3 Significant modes

For each surface wave mode, eigenfrequencies and corresponding partial derivatives can be computed for an Earth model described by  $\alpha(r)$ ,  $\beta(r)$  and  $\delta(r)$ . Partial derivatives show how a physical properties (e.g. phase velocity) for a particular period change in response to a shear velocity perturbation at a specific depth, i.e. describe the sensitivity of a mode to anomalies in the Earth structure. Higher modes sense the Earth deeper, while for a specific mode, higher frequencies indicate sensitivity for shallower structure.

The sensitivity of a seismic wave to the Earth structure depends, among others, on which modes build the waveform. The set of modes constituting a seismogram and the relative contribution of each mode are determined by the seismic source and the Earth structure at the hypocenter.

To better understand differences in Earth models obtained from Love and Rayleigh waves, we analysed the modes composing the waveforms used in this study. In particular we determined which modes are significantly contributing in the waveform fitting to determine the 1D path average velocity structure. For every path, using the real moment tensor solu-

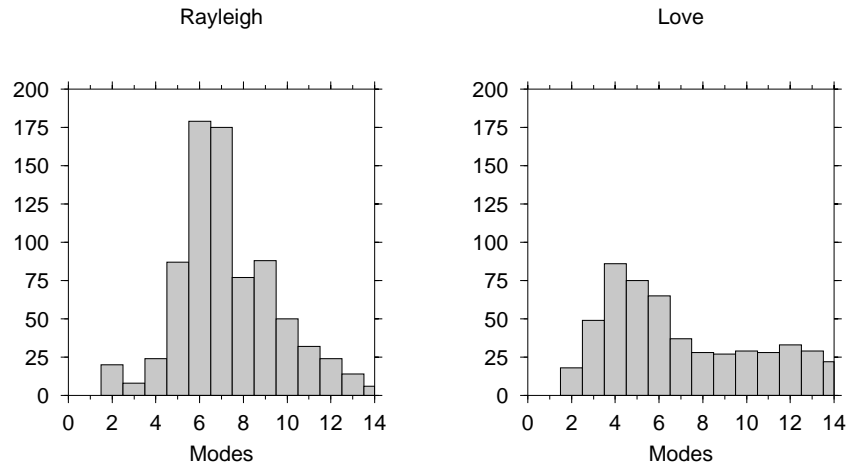


**Figure 5.5:** Histograms of the number of significant higher modes contributing to the waveform misfit.

tion, we computed synthetic seismograms composed only by the fundamental mode, the fundamental and the first higher mode, the fundamental and the first two higher modes, and so on. We selected the same time and frequency window as for the corresponding real seismogram and computed the misfit according to eq. 5.1 between the waveform composed only by the fundamental mode and the synthetic seismograms containing the higher modes. Since seismograms are dominated by energy of the fundamental and first higher modes, addition of other modes is hardly changing the waveform and therefore the corresponding misfit. For every path, a misfit curve describing the dependence of the misfit on the number of higher modes has been obtained. The number of significant higher modes has been defined as the highest number, for which the difference between the misfit and the mean of the misfit curve for that specific path does not fall within the standard deviation. Fig. 5.5 shows the distribution of the number of significant higher modes for all analysed waveforms. Although the mean value is around 7 for both types of waves, the distribution shows significant differences. For Rayleigh waves, most seismograms are indeed constituted by 6-7 significant higher modes. For Love waves, the distribution is broader with a maximum observed for 4 significant higher modes. Inspection of single examples showed that often for Love waves there are two maxima in the misfit curve, while for Rayleigh waves, on average, after growing the misfit stabilizes around a constant value. A difference is also observed in the misfit absolute value between Love and Rayleigh waves. The misfit is on average more than 2.5 times smaller for Love than Rayleigh waves. Love waveforms seem to be less influenced by higher modes, suggesting that Love waves might contain less information on the Earth velocity structure than Rayleigh waves. A dependence of the number of significant higher modes from hypocenter depth is not observed.

## 5.4 Significant linear constraints

Following Van der Lee & Nolet (1997), the average  $S$ -velocity perturbation  $\overline{\delta\beta(r)}$  along the path between source and receiver has been expressed in terms of a number of basis functions  $h_i(r)$ :

$$\overline{\delta\beta(r)}/\sigma_\beta = \sum_{i=1}^M \gamma_i h_i(r) \quad (5.2)$$

where  $\gamma_i$  are the parameters to be determined by minimizing eq. 5.1 and  $\sigma_\beta$  is the estimated standard deviation of the distribution of existing  $S$ -velocities. Since the average velocity perturbation along the surface wave path  $P_j$  is defined as

$$\overline{\delta\beta_j(r)} = \frac{1}{\Delta_j} \int_{P_j} [\beta(\theta, \phi, r) - \beta_j^0(r)] d\Delta \quad (5.3)$$

where  $\Delta_j$  is the epicentral distance along the great circle path  $P_j$  and  $\beta_j^0(r)$  is the background  $S$ -velocity model along  $P_j$ , once  $\gamma = \gamma_{opt}$  for the minimum of  $F(\gamma)$  have been determined, we have obtained  $M$  linear constraints for the Earth model  $\beta(\theta, \phi, r)$ . If every  $\gamma_i$  would be uniquely determined, we could obtain  $\beta(\theta, \phi, r)$  by solving the system composed by linear constraints from many paths. However, there is no guarantee that the equations for  $\gamma_i$  are independent. On the contrary, they often occur to be highly dependent. The shape of  $F$  around the minimum  $\gamma_{opt}$  can be used to determine new directions in the parameter space useful to transform eq. 5.2 into a system of independent data. To this end, the Hessian matrix  $H_{ij} = \frac{\partial^2 F}{\partial \gamma_i \partial \gamma_j}$  around the minimum  $\gamma = \gamma_{opt}$  is diagonalized

$$\mathbf{H} = \mathbf{S}\mathbf{\Lambda}\mathbf{S}^T \quad (5.4)$$

and a new parameter is defined as

$$\boldsymbol{\eta} = \mathbf{S}^T \boldsymbol{\gamma} \quad (5.5)$$

Since  $\mathbf{H}$  is symmetric,  $\boldsymbol{\gamma} = \mathbf{S}\boldsymbol{\eta}$ . Eq. 5.2 can now be rewritten in terms of the new parameters

$$\overline{\delta\beta(r)}/\sigma_\beta = \sum_{i=1}^M \sum_{j=1}^M S_{ij} \eta_j h_i(r) = \sum_{j=1}^M \eta_j g_j(r) \quad (5.6)$$

with transformed basis functions

$$g_j(r) = \sum_{i=1}^M S_{ij} h_i(r) \quad (5.7)$$

To investigate how many and which independent linear constraints contribute significantly to the determination of the path average velocity structure for Love and Rayleigh waves

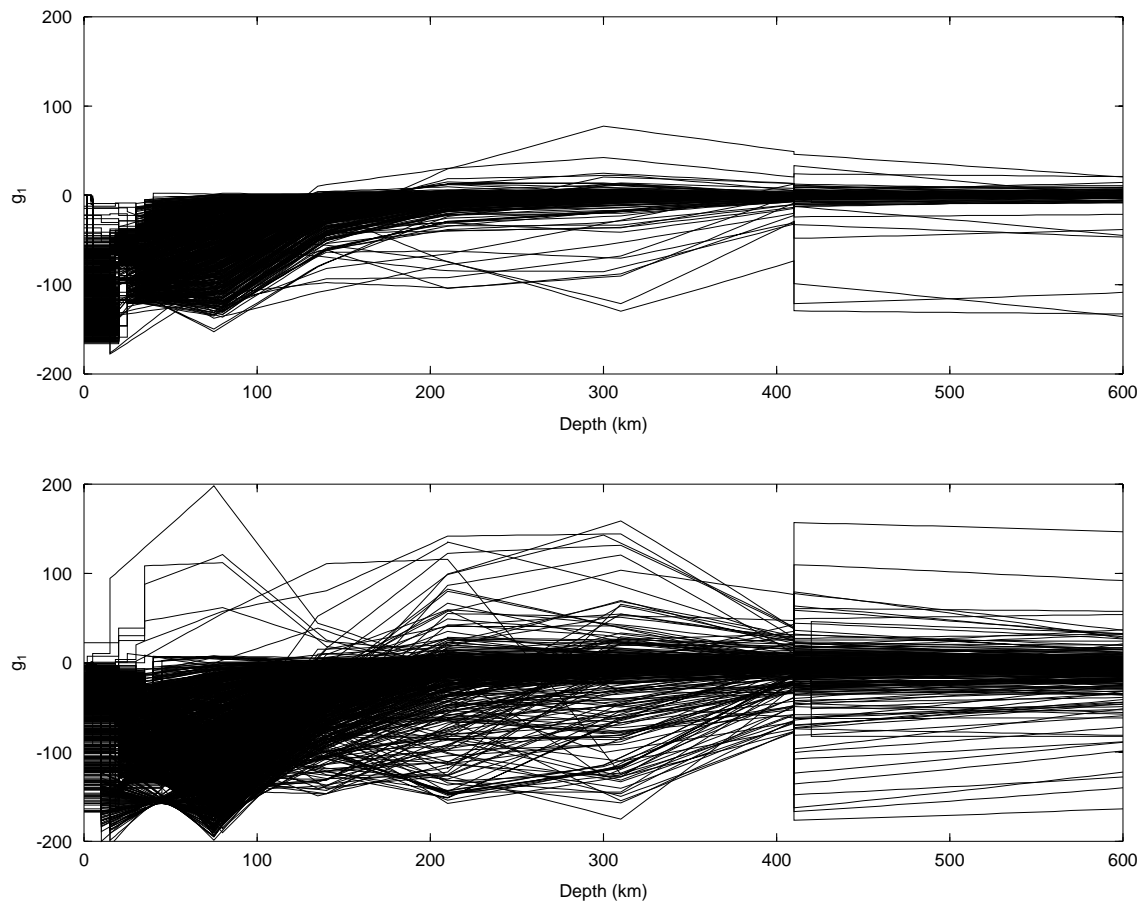


**Figure 5.6:** Transformed basis functions  $g_1(r)$  corresponding to the most significant independent parameter  $\eta_1$  for Love (top) and Rayleigh (bottom) waves. The largest sensitivity for Love waves is observed down to 130 km depth, without distinction between crust and upper mantle. For Rayleigh waves more diversity is present. Largest sensitivity is observed for the upper mantle down to 200 km, while on average is reduced for the crust.

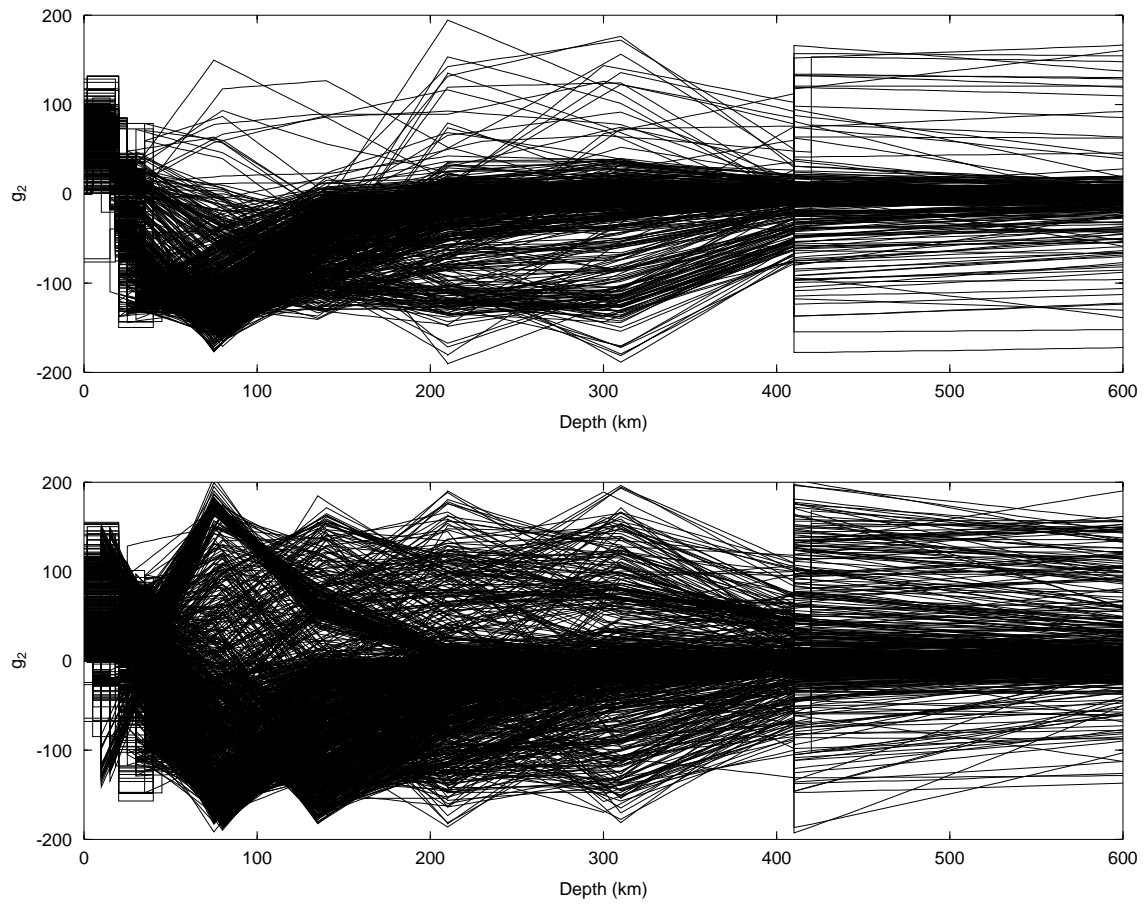


**Figure 5.7:** Transformed basis functions  $g_2(r)$  corresponding to the second most significant independent parameter  $\eta_2$  for Love (top) and Rayleigh (bottom) waves.

and therefore better understand the actual, empirical sensitivity of surface waves to Earth structure, we proceeded similarly as in section 5.3. The eigenvalues of  $\mathbf{H}$  are used to compute the standard deviations  $\Delta\eta$  and therefore describe the significance of the elements of  $\eta$ . For each path, we computed seismograms considering only the most significant, the 2 most significant, the 3 most significant elements of  $\eta$  and so on. The misfit between these seismograms and the data has been computed according to eq. 5.1. We determined the number of significant parameters contributing to the 1D path average velocity structure by selecting the highest number after which the misfit is not significantly changing anymore, though more parameters are added. The number of parameters significantly contributing to the determination of the path average velocity structure for Love and Rayleigh waves are 3 and 4 respectively. Information on the sensitivity of Love and Rayleigh waves to Earth structures can be gained from the inspection of the transformed basis functions  $g_i(r)$  (eq. 5.7) corresponding to the significant parameters  $\eta_i$ . Particularly striking is the difference between  $g_1(r)$  (basis function corresponding to the most significant element of  $\eta$  ( $=\eta_1$ )) for Love and Rayleigh waves (Fig. 5.6). The largest sensitivity for Love waves is observed for the crust and uppermost mantle down to 130 km depth.  $g_1(r)$  for all paths look similar. For Rayleigh waves, the picture is much more diverse. Largest sensitivity is observed for the upper mantle down to 200 km, while on average is reduced for the crust. Significant sensitivity is present down to the transition zone.  $g_2(r)$ , the transformed basis functions corresponding to the second most important independent parameter  $\eta_2$ , are shown in Fig. 5.7. Although the sensitivity variability for Love waves increased compared to Fig. 5.6,  $g_2(r)$  for Rayleigh waves show a larger diversity. Love waves are on average sensitive to the difference between the uppermost mantle and crustal structure. The sensitivity of Rayleigh waves is much more complex and different from path to path. On average Love waves are only sensitive to the combination of crustal and upper mantle structure. There is strong indication that no independent information on crustal or upper mantle structure is present. This suggests that strong trade-offs between crustal and upper mantle velocities could exist and bias the resulting 3D velocity model.

Larger trade-offs between crustal thickness and upper mantle velocities for Love than for Rayleigh waves have also been observed. In Fig. 5.8 the misfit (eq. 5.1) as a function of changes in Moho depth and sub-Moho velocity is plotted for several examples. A comparison of the plots for Rayleigh and Love waves shows that the minimum in the case of Rayleigh waves is better defined (contour lines closer together) and that the trade-offs between Moho depth and sub-Moho velocity, although existent for both types of waves, are larger for Love waves.

## 5.5 Surface wave refraction at sharp vertical boundaries

Sharp vertical discontinuities in the crust and upper mantle system such as ocean-continent boundaries and/or regions of transition between old and thick lithosphere (cratons) and younger continental provinces, can strongly influence the propagation of surface waves.

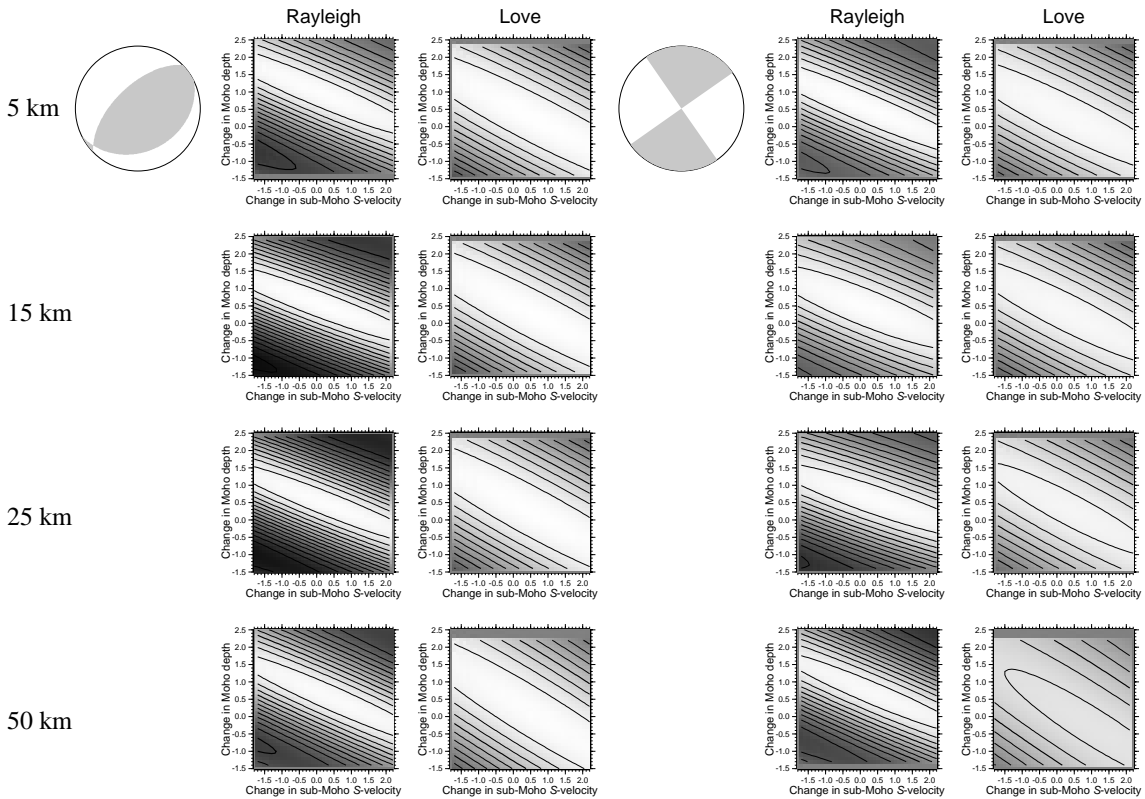


**Figure 5.8:** Contour plot of the misfit (eq. 5.1) as a function of changes in Moho depth and sub-Moho S-velocity (in the scale, 1 corresponds to one estimated standard deviation: 225 m/s for S-velocity, 5000 m the Moho depth). Examples for 2 different focal mechanisms and 4 hypocenter depths are shown. The epicentral distance is  $10^\circ$ .

Since for a specific frequency, Love waves are more sensitive to shallow structures than Rayleigh waves and the strongest vertical boundaries are observed in the uppermost mantle, processes such as refraction could be more important for Love waves.

Although no real ocean-continent or craton-young lithosphere boundary is present in the Mediterranean area, a laterally strong heterogeneous structure has been imaged in the uppermost mantle (Marone et al., 2003a). Tectonic provinces with different structural characteristics such as mountain ranges, back-arc basins and subduction zones are contiguous. Most paths we analysed in the Mediterranean region are not confined within one province, but cross at least one boundary.

To evaluate the possible effect of sharp vertical boundaries on the direction of the wave propagation path, we selected several 1D S-velocity models characteristic for the Mediterranean region, computed corresponding phase velocities for Rayleigh and Love waves and calculated path deviations assuming that the refraction process follows Snellius law.

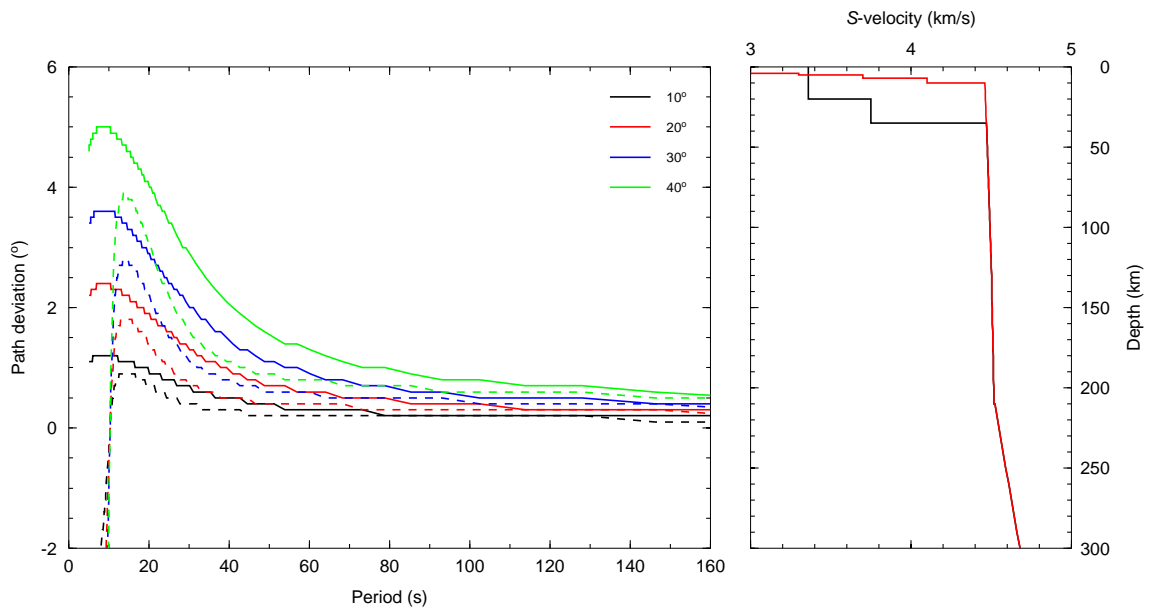


**Figure 5.9:** On the left, angles of the path deviation at the source for different incident angle at the vertical boundary for Love (continuous line) and Rayleigh waves (dashed line). On the right, two 1D  $S$ -velocity models representing the Earth structure on either side of the vertical discontinuity: in black *iasp91*, in red a profile for an oceanic structure. We assumed the transition to be in the middle between source and receiver.

### 5.5.1 Path deviations

We calculated the azimuthal deviation of paths at the source compared to the great circle, if refraction at a vertical boundary is taken into account. In Figs. 5.9 and 5.10 deviations for different angles of incidence are shown for two different structures. Positive values are obtained if the phase velocity for the first medium is slower than for the second and vice versa. In the first example (Fig. 5.9), we simulated an ocean-continent transition. Maximum deviations ( $4^\circ$ - $5^\circ$ ) are observed for the shorter period waves, propagating through the crust. The difference between Rayleigh and Love waves is smaller than  $1^\circ$ . In Fig. 5.10 we selected two extreme 1D  $S$ -velocity models from a regional 3D velocity model for the Mediterranean region (Marone et al., 2003a): one representing a back-arc basin (thin crust and low upper mantle velocities), the other one for a subduction environment (thick crust and high upper mantle velocities). For Rayleigh waves, significant azimuthal deviations are observed only for periods smaller than 50 s, while for Love waves  $2^\circ$  path perturbations are present up to periods of 80 s. However, even for a boundary between such extreme models, the maximum deviation at the source of the actual path from the great circle is  $9^\circ$  for both Rayleigh and Love wave.

To study the influence of path deviations on the waveform fit, we computed synthetic



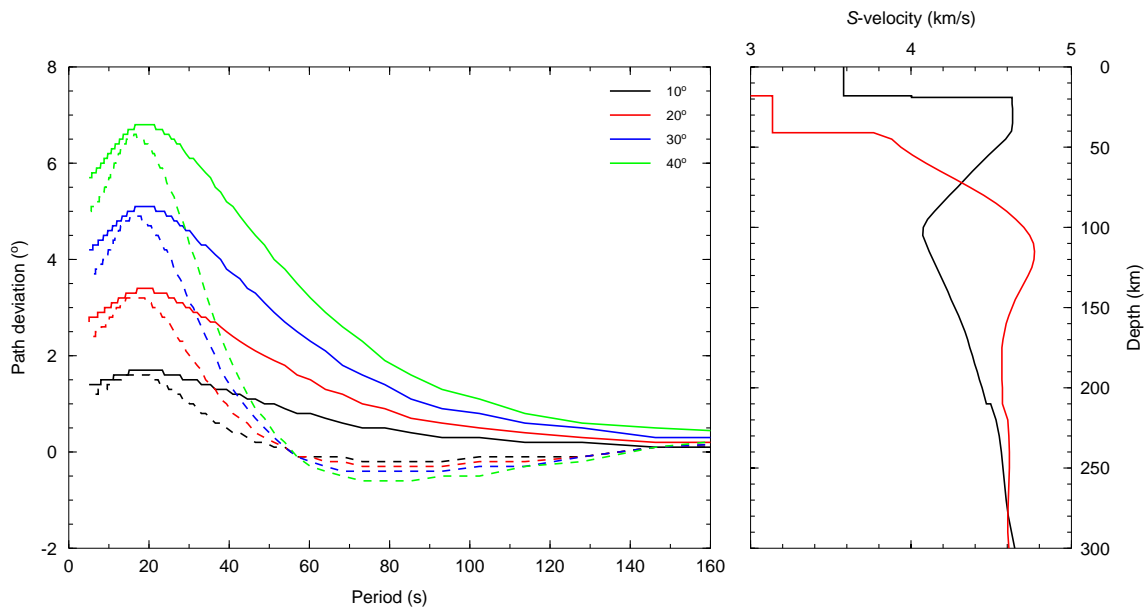


**Figure 5.10:** On the left, angles of the path deviation at the source for different incident angle at the vertical boundary for Love (continuous line) and Rayleigh waves (dashed line). On the right, two 1D  $S$ -velocity models representing the Earth structure on either side of the vertical discontinuity. The profile in black represents the structure of a back-arc basin (Algero-Provençal Basin), with a thin crust and an asthenospheric layer. The red profile shows the upper mantle structure beneath station ITHO (Fig. 2.1) and is characterized by a 40 km thick crust and high upper mantle velocities traceable to the subducted Hellenic slab. We assumed the transition to be in the middle between source and receiver.

seismograms for waves travelling along refracted paths. We assumed  $10^\circ$  deviation at the source. We fitted this synthetic data (Love and Rayleigh waveforms separately) assuming waves propagation direction and excitation at the source along the great circle path (an example is shown in Fig. 5.11). In most cases we observe differences in the amplitude of Love waves. Source radiation patterns for Love waves show in general 4 nodes, while for Rayleigh waves in most cases only 2 are present. Therefore a wrong wave azimuth has a stronger influence on Love waveforms, because the excitation factor is varying more rapidly within a small angle. The obtained fit between observed and synthetic Rayleigh waveforms is very satisfactory. Only the radial waveform is partially distorted. Although it was not possible to obtain a perfect match between observed and synthetic waveforms, the difference between the retrieved and the original upper mantle  $S$ -velocity models for both Love and Rayleigh waves falls within the uncertainties. Less than 1 km difference is observed between the original and retrieved Moho depth. Since it was also always possible to jointly fit the 3 components of these test waveforms with a single 1D model for

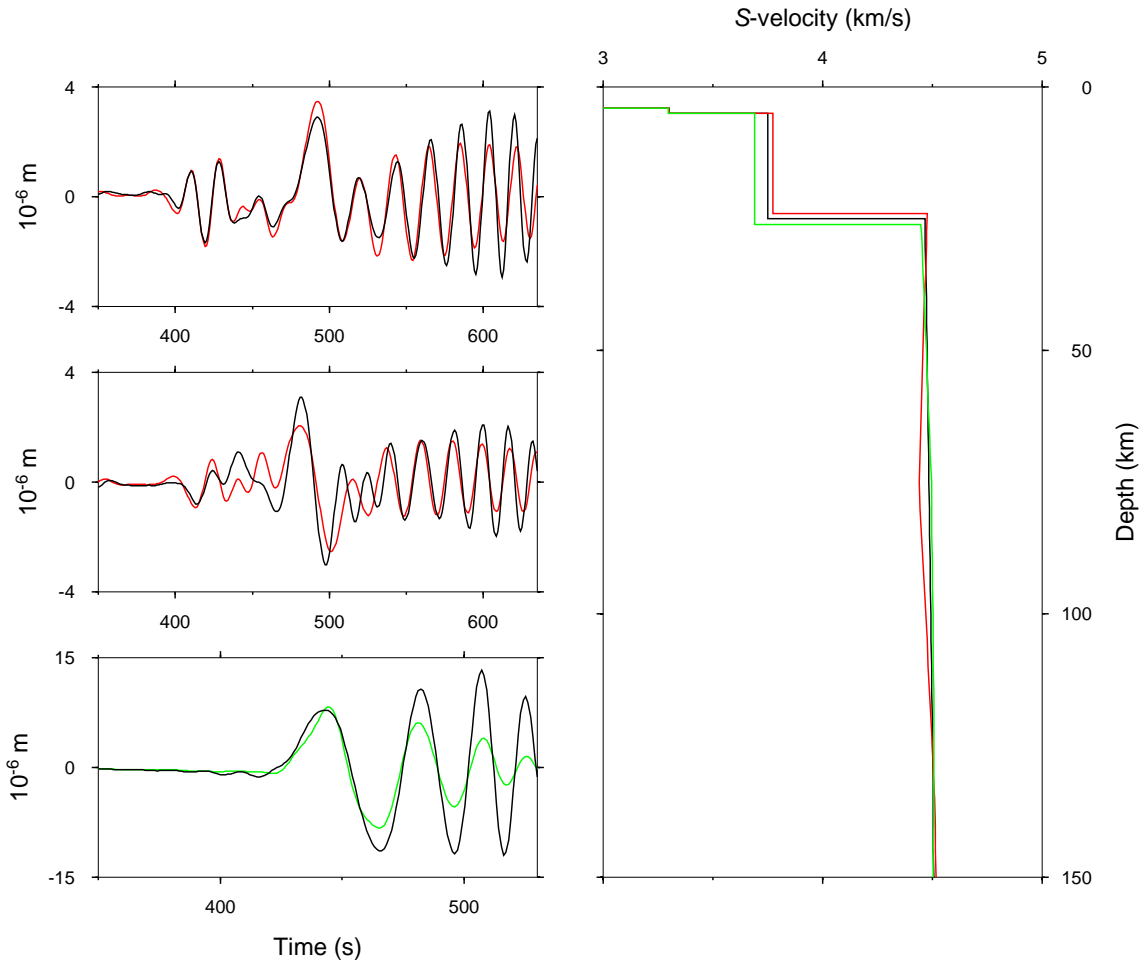


**Figure 5.11:** Three component synthetic seismograms for waves travelling along a refracted path (black) for  $10^\circ$  azimuthal variation at the source have been fitted assuming wave propagation direction and excitation at the source along the great circle path (in red for Rayleigh (vertical and radial components at the top and in the middle respectively), in green for Love waves). On the right the corresponding S-velocity models.

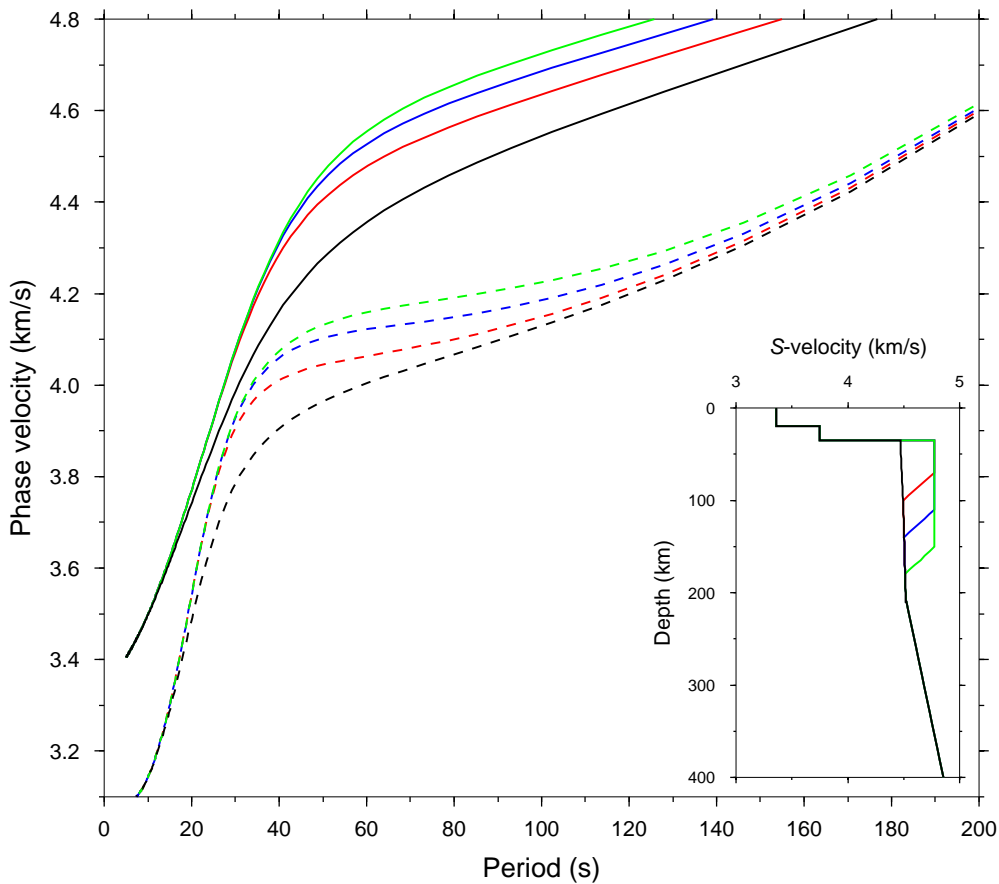


**Figure 5.12:** Phase velocities for Love (continuous line) and Rayleigh waves (dashed line) for the models shown in the inset.

Love and Rayleigh waves, realistic deviations of the wave path from the great circle do not explain the observed incompatibility of 1D velocity models derived from Love and Rayleigh data (section 5.1).

### 5.5.2 Phase velocities

Information on surface waves sensitivity to Earth structure can be gained from the inspection of phase velocity curves. We computed phase velocities for the fundamental mode surface wave (both Rayleigh and Love) from a set of 1D  $S$ -velocity models. In the first example (Fig. 5.12), we simulated a lithosphere with different thicknesses. While Rayleigh waves clearly detect the base of the lithosphere and for long periods (sensitive to deeper structure) the curves merge together, the sensitivity of Love waves seems to be reduced to the uppermost mantle. The base of the lithosphere is not detected: the phase

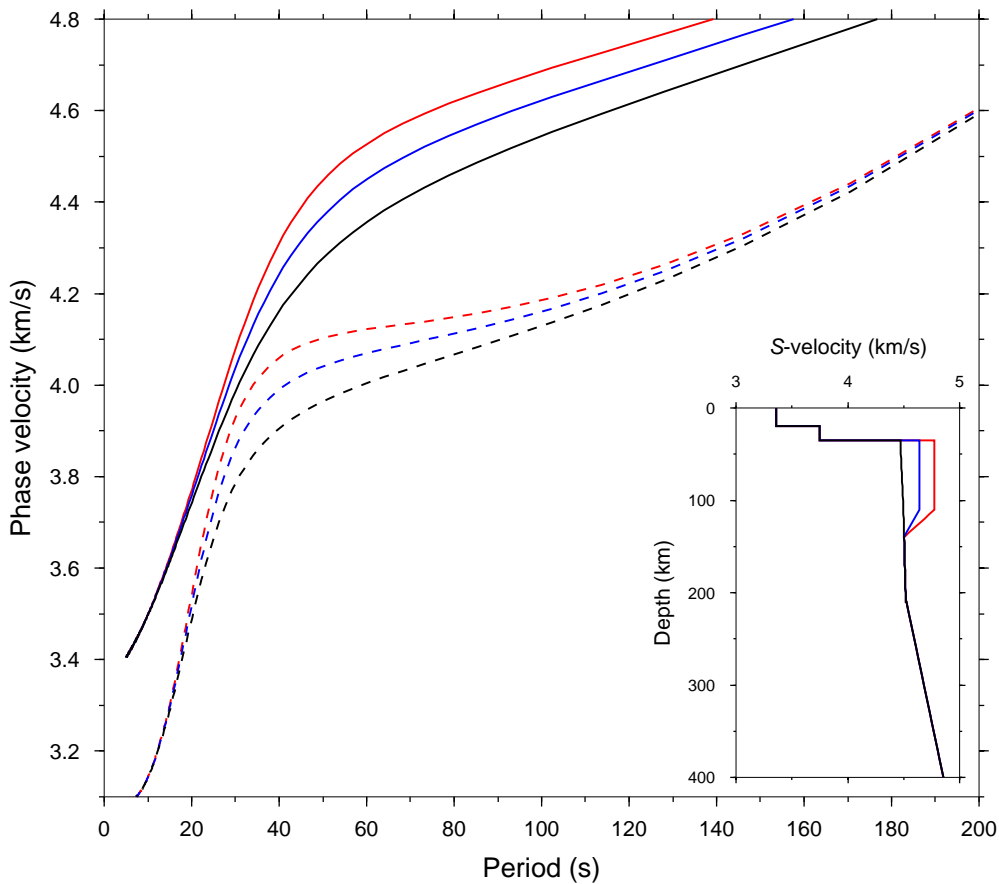


**Figure 5.13:** Phase velocities for Love (continuous line) and Rayleigh waves (dashed line) for the models shown in the inset.

velocity curves are parallel for periods larger than 60 s and do not merge. Fig. 5.13 shows phase velocity curves for models characterized by a lithosphere with different velocities but constant thickness. Same features as in Fig. 5.12 are observed and a close comparison of Figs. 5.12 and 5.13 shows how non-unique the information contained in phase velocity curves can be. It is difficult to distinguish between phase velocity curves corresponding to 1D models with a thin fast lithosphere or a thick slower one. This ambiguity is more marked for Love waves, which seem to be more sensitive to an average upper mantle structure than to single velocity anomalies. This type of wave can also not uniquely determine the depth of similar high velocity anomalies (Fig. 5.14), while crossing phase velocity curves for Rayleigh waves indicate anomalies starting and ending at different depths.

Phase velocities curves for different 1D  $S$ -velocity models suggest that Rayleigh waves can more unambiguously determine strength and depth of velocity anomalies than Love

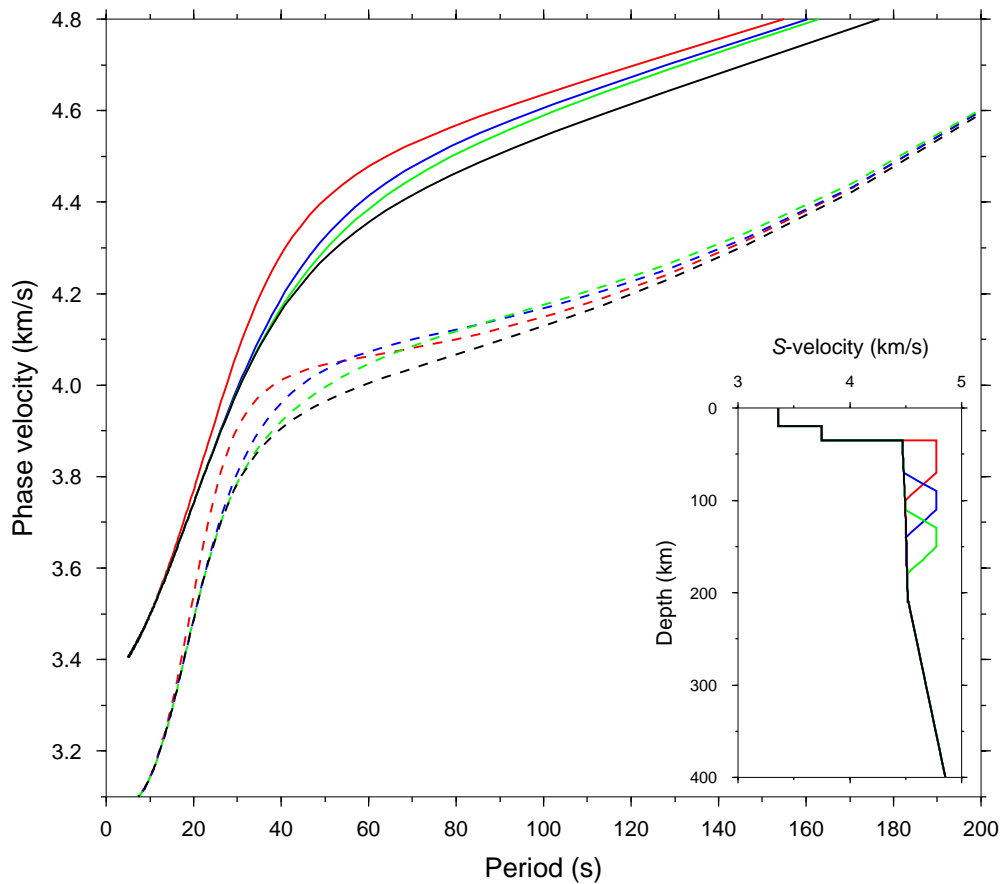


**Figure 5.14:** Phase velocities for Love (continuous line) and Rayleigh waves (dashed line) for the models shown in the inset.

waves, which are in general only sensitive to a mean average model. A similar sensitivity difference has also been suggested by the analysis of the significant parameters and corresponding basis functions obtained in the waveform fitting (section 5.4).

## 5.6 Conclusions and outlook

We have described discrepancy between 1D path average velocity models obtained from Love and Rayleigh waves travelling through the same region. The similarity of the retrieved 1D  $S$ -velocity models with anisotropic PREM (Dziewonski & Anderson, 1981) suggests that at least part of the discrepancy could be traceable to radial anisotropy. Therefore, the linear constraints extracted from Love and Rayleigh waves have been inverted separately. The obtained 3D velocity models show different characteristics, which

can only partly be explained by the possible presence of anisotropy. The horizontal size of the anomalies in the model retrieved from Love waves is larger than in the model obtained from Rayleigh waves. In addition, although the system of linear equations provided by Love waves is smaller than in the Rayleigh case, more iterations are necessary for the inversion to converge and the achieved variance reduction is smaller. The inversion of the Love dataset shows that the constraints obtained by the analysis of Love waves might be more inconsistent among each other compared to the constraints in the Rayleigh dataset. The larger variance reduction and early convergence obtained by fixing the Moho depth to the values of EAM02 in a test inversion of the linear constraints derived from Love waves suggest that Love waves cannot uniquely determine Moho depth and velocities around it. Inspection of surface waves sensitivity suggests important differences in the ability of determining the Earth structure for Rayleigh and Love waves. While the sensitivity of Rayleigh waves is strongly diverse and is path dependent, the sensitivity variability for Love waves is reduced. The largest sensitivity for Rayleigh waves is observed for the upper mantle down to 200 km, while on average is reduced for the crust. Love waves are only sensitive to the combination of crustal and upper mantle structure, while there is strong indication that they do not contain any independent information on crustal or upper mantle structure. This suggests that for models derived from Love waves strong trade-offs between crustal and upper mantle velocities could exist and bias the resulting 3D velocity structure. Synthetic tests also shows larger trade-offs between Moho depth and uppermost mantle velocities for Love than Rayleigh waves.

Although the Mediterranean crust and upper mantle are characterized by strong lateral heterogeneities and due to refraction at sharp vertical boundaries variations in azimuth up to  $10^\circ$  with respect to the great circle path can occur, bias of the retrieved velocity model is minimal and falls within the uncertainties for both Love and Rayleigh waves. However, at sharp vertical boundaries, a seismic wave not only is refracted, but part of the energy is reflected and/or converted to a different mode. To better understand the information contained in surface waves, it would be interesting to compute synthetic seismograms for a 3D *S*-velocity model taking into account physical processes such as reflection, refraction and mode conversion at sharp boundaries. Comparison of these 3D synthetic seismograms with real data and synthetic waveforms computed according to path average velocity structures could be important to determine possible differences of e.g. energy contamination on Love and Rayleigh waveforms, which could be responsible for biases in the imaged velocity structures and for inconsistencies within datasets.

## Conclusions

---

Thanks to new data recorded at 25 broad band seismic stations temporarily deployed along the Eurasia-Africa plate boundary region (MIDSEA project) as well as at permanent European seismic stations, we can present the first Moho depth map and regional *S*-velocity model resolving the complete Eurasia-Africa plate boundary region from the Azores to the eastern Mediterranean Sea. Striking similarities between our shear wave velocity model and body wave tomographic images (e.g. Bijwaard & Spakman, 2000) for the extensively studied continental European region have been observed. Although the imaged heterogeneities in our model show a longer wavelength character compared to *P*-velocity models due to smoothing and different data characteristics, we do observe consistent results between body and surface wave tomography studies (independent data with different sensitivity) where the resolving power of the used dataset is good. This is giving further confidence to our *S*-velocity model for regions poorly studied before where we could achieve an unprecedented resolution, like for the shallow mantle beneath the Mediterranean Sea, northern Africa and the eastern Atlantic Ocean.

The imaged heterogeneous crust and upper mantle structure of the Mediterranean area confirms the complex evolution of this plate boundary region and shows the same order of complexity as observed at the surface. The Moho topography as well as the imaged upper mantle heterogeneities correlate with the tectonics and geology along the plate boundary. The suture zone between Eurasia and Africa is characterized by mountain ranges, extending from northern Algeria, through Italy, the Balkans and Greece to Turkey and is outlined by high seismicity. Thick crust (> 35 km) has been found in correspondence of the collision zones such as the Maghrebides, Alps, Dinarides and Hellenides. The Eurasia-Africa

suture zone manifests itself in the upper mantle mainly as a belt of high-velocity material representing subducted oceanic lithosphere. It can be followed as deep as 300-600 km, depending on the region and resolution. Since subduction did not occur contemporarily throughout the region and sinking velocities are not necessarily spatially homogeneous, fragments of African lithosphere reside at different depths in the upper mantle. Where the process is still active (e.g. Crete), a continuous positive anomaly is observed from the surface down to the transition zone. At old subduction zones (e.g. Spain), detached pieces of seismically fast material are imaged deeper than 250 km.

A new, striking and resolved feature of our *S*-velocity model is a positive anomaly imaged beneath eastern Spain between 250 and 500 km depth. We suggest that this fast body could be a fragment of subducted lithosphere, which detached in an early stage of NW subduction of oceanic lithosphere in the western Mediterranean. Although time and mechanisms of this event are still unclear, the new image of the eastern Iberian upper mantle could represent a new key element for the reconstruction of the western Mediterranean history.

The Mediterranean Sea exhibits strong lateral variations in crustal and upper mantle structure, confirming different origin and evolution of the western and eastern parts. In the west, the Moho discontinuity has been observed as shallow as 15-20 km. Between 80 and 200 km, *S*-velocities as low as 4.2 km/s are the indication for an asthenospheric layer. The lithosphere-asthenosphere system of the western Mediterranean clearly differentiates itself from the structure of the older eastern Atlantic Ocean as well as from the structure of a young (4 to 20 Ma old) ocean. The extensively stretched and partly oceanic crust together with the uppermost mantle structure support the idea that, rather than a young ocean, the western Mediterranean could be a strongly stretched continent, partly affected by spreading, formed at the back of a slab. The structure characterizing the eastern Mediterranean (25-30 km thick crust, missing asthenospheric layer and average *iasp91* upper mantle *S*-velocities) suggests that this region is different from both an oceanic basin and a strongly stretched continent. The imaged structure points to a continuation of the northern African continental lithosphere beneath the eastern Mediterranean Sea.

Below the eastern North Atlantic Ocean the obtained Moho map shows a crust up to 5 km thicker than standard oceanic crust. From its highly perturbed relief, we interpreted the crust here to be heterogeneous, as a consequence of periods with different magma supply characteristic of slow spreading ridges. An additional effect contributing to the imaging of an apparently anomalous thickness could be the serpentinization of the sub-Moho mantle. Major structural differences in the eastern Atlantic Ocean upper mantle are imaged between the Mid-Atlantic ridge and the older oceanic basins: the eastern Atlantic lithosphere is characterized by lower velocities beneath the spreading ridge than under the old ocean basins. Despite strong differences observed in the crustal structure between the Mid-Atlantic ridge and the Azores, no significant differences are observed in the upper mantle *S*-velocity structure.



Airy isostatic compensation in the Mediterranean region has been assessed by comparing the Moho topography obtained with the Moho depth computed assuming isostatic compensation at 60 km depth. Most of the Mediterranean and eastern Atlantic region appears in isostatic equilibrium. In the eastern Mediterranean Basin strong positive residuals are likely due to overestimating the crustal thickness, owing to an extremely low average  $S$ -velocity in the upper crust due to the presence of thick sedimentary deposits. The lithospheric low density required for isostatic compensation in the Bay of Biscay region, contrasting with observed high  $S$ -velocities in the top 50 km of the mantle, confirms the presence of Archaean cratonic material.

Although only information provided by  $S$ - and Rayleigh waves has been used to derive the presented Moho depth map and upper mantle velocity model, Love waveforms have also been analysed. Discrepancy between 1D path average velocity models obtained from Love and Rayleigh waves travelling through the same region has been observed. The uppermost mantle velocity structure retrieved from Rayleigh data is consistently slower (up to 4%) than velocities obtained from Love wave data. Comparing the average  $S$ -velocity models obtained from Love and Rayleigh waveforms with the global anisotropic model PREM (Dziewonski & Anderson, 1981), we observe a strong analogy. This suggests that the observed incompatibility between the velocity models obtained with the two types of data, at least in part, is due to radial anisotropy in the Mediterranean upper mantle. However, comparison of the results of separate 3D inversions of linear constraints obtained from Love and Rayleigh data suggests that the constraints obtained by the analysis of Love waves might be more inconsistent among each other compared to the constraints in the Rayleigh dataset. Inspection of surface wave sensitivity to Earth structure indicates that such inconsistencies could arise from trade-offs between crustal and upper mantle velocities as well as Moho depth and uppermost mantle velocities, which have been observed to be larger for Love than Rayleigh waves. Bias of the retrieved velocity models due to path deviations with respect to the great circle due to the strong laterally heterogeneous upper mantle structure of the Mediterranean region is instead minimal and falls within the uncertainties for both Love and Rayleigh waves.



# Point constraints references

---

## A.1 Receiver function studies

- Bertrand, E. & Deschamps, A., 2000. Lithospheric structure of the southern French Alps inferred from broadband analysis, *Phys. Earth Planet. Inter.*, **122**, 79–102.
- Li, X., Harjes, H.-P., Vafidis, A., Van der Meijde, M., Hanka, W., Wylegalla, K., Bock, G., Kind, R., & Yuan, X., 2001. A receiver function study of the Hellenic subduction zone, in *Newsletter, European Geophysical Society Newsletter*, vol. 78, p. 64, XXVII General Assembly, Nice, France.
- Megna, A. & Morelli, A., 1994. Determination of Moho depth and dip beneath Med-Net station AQU by analysis of broadband receiver functions, *Annali di geofisica*, **XXXVII**(5), 913–928.
- Paulssen, H. & Visser, J., 1993. The crustal structure in Iberia inferred from *P*-wave coda, *Tectonophysics*, **221**, 111–123.
- Sandvol, E., Seber, D., Calvert, A., & Barazangi, M., 1998. Grid search modelling of receiver functions: Implications for crustal structure in the Middle East and North Africa, *J. Geophys. Res.*, **103**(B11), 26899–26917.
- Saunders, P., Priestley, K., & Taymaz, T., 1998. Variations in the crustal structure beneath western Turkey, *Geophys. J. Int.*, **134**, 373–389.

Van der Meijde, M., Van der Lee, S., & Giardini, D., 2003. Crustal structure beneath broadband seismic stations in the Mediterranean region, *Geophys. J. Int.*, **152**, 729–739.

## A.2 Gravity studies

Best, J., Barazangi, M., Al Saad, D., Sawaf, T., & Gebran, A., 1990. Bouguer gravity trends and crustal structure of the Palmyride Mountain Belt and surrounding northern Arabian platform in Syria, *Geology*, **18**(12), 1235–1239.

Khair, K., Khawlie, M., Haddad, F., Barazangi, M., Seber, D., & Chaimov, T., 1993. Bouguer gravity and crustal structure of the Dead Sea transform fault and adjacent mountain belts in Lebanon, *Geology*, **21**(8), 739–742.

Khair, K., Tsokas, G., & Sawaf, T., 1997. Crustal structure of the northern Levant region: multiple source Werner deconvolution estimates for Bouguer gravity anomalies, *Geophys. J. Int.*, **128**, 605–616.

Makris, J., Henke, C., Egloff, F., & Akamaluk, T., 1991. The gravity field of the Red Sea and East Africa, *Tectonophysics*, **198**(2-4), 369–381.

Mickus, K. & Jallouli, C., 1999. Crustal structure beneath the Tell and Atlas Mountains (Algeria and Tunisia) through the analysis of gravity data, *Tectonophysics*, **314**, 373–385.

Seber, D., 1995. *Lithospheric and Upper Mantle Structure Beneath Northern Morocco and Central Syria*, Ph.D. thesis, Cornell University.

Tsokas, G. & Hansen, R., 1997. Study of the crustal thickness and the subducting lithosphere in Greece from gravity data, *J. Geophys. Res.*, **102**(B9), 20585–20597.

## A.3 Reflection and refraction seismic studies

Bohnhoff, M., Makris, J., Papanikolaou, D., & Stavrakakis, G., 2001. Crustal investigation of the Hellenic subduction zone using wide aperture seismic data, *Tectonophysics*, **343**, 239–262.

Collier, J., Buhl, P., Torné, M., & Watts, A., 1994. Moho and lower crustal reflectivity beneath a young rift basin: results from a two-ship, wide-aperture seismic-reflection experiment in the Valencia Through (western Mediterranean), *Geophys. J. Int.*, **118**, 159–180.

- De Voogd, B., Truffert, C., Chamot-Rooke, N., Huchon, P., Lallemand, S., & Le Pichon, X., 1992. Two-ship deep seismic soundings in the basins of the Eastern Mediterranean Sea (Pasiphae cruise), *Geophys. J. Int.*, **109**, 536–552.
- Doser, D., Keler, G., Harder, S., Miller, K., & Dial, P., 1997. Development of a lithospheric model and geophysical database for North Africa, Final Report PL-TR-97-2136, Department of energy, Office of non-proliferation and National Security Philips Laboratory, Directorate of Geophysics, University of Texas/El Paso.
- Dragašević, T. & Andrić, B., 1968. Deep seismic soundings of the Earth's crust in the area of the Dinarides and the Adriatic Sea, *Geophys. Prospecting*, **16**(1), 54–76.
- Egger, A., 1992. *Lithospheric structure along a transect from the northern Apennines to Tunisia derived from seismic refraction data*, Ph.D. thesis, ETH Zurich, Zurich, Switzerland.
- Fowler, C., 1976. Crustal structure of the Mid-Atlantic ridge crest at 37°N, *Geophys. J.R. astr. Soc.*, **47**, 459–491.
- Fowler, C. & Keen, C., 1979. Oceanic crustal structure - Mid-Atlantic Ridge at 45°N, *Geophys. J.R. astr. Soc.*, **56**, 219–226.
- Gallart, J., Vidal, N., & Dañobeitia, J. J., 1995. Multichannel seismic image of the crustal thinning at the NE Iberian margin combining normal and wide angle reflection data, *Geophys. Res. Lett.*, **22**(4), 489–492.
- Gaudiosi, G., Guerra, I., Luzio, D., Milano, G., Musacchio, G., & Ventura, G., 2001. Towards a Moho map in the southern Tyrrhenian Sea, in *Newsletter, European Geophysical Society*, vol. 78, p. 74, XXVII General Assembly, Nice, France.
- Ginzburg, A. & Ben-Avraham, Z., 1987. The deep structure of the Central and Southern Levant continental margin, *Ann. Tectonicae*, **1**(2), 105–115.
- Ginzburg, A. & Folkman, Y., 1980. The crustal structure between the Dead Sea rift and the Mediterranean Sea, *Earth Planet. Sci. Lett.*, **51**, 181–188.
- Ginzburg, A., Makris, J., Fuchs, K., & Prodehl, C., 1981. The structure of the crust and upper mantle in the Dead Sea Rift, *Tectonophysics*, **80**, 109–119.
- Ginzburg, A., Whitmarsh, R., Roberts, D., Montadert, L., Camus, A., & Avedik, F., 1985. The deep seismic structure of the northern continental margin of the Bay of Biscay, *Ann. Geophys.*, **3**(4), 499–510.

- Hauser, F., Railenau, V., Fielitz, W., Bala, A., Prodehl, C., Polonic, G., & Schulze, A., 2001. VRANCEA 99 - the crustal structure beneath the southeastern Carpathians and the Moesian Platform from a seismic refraction profile in Romania, in *Starkbeben: vom geowissenschaftlichen Grundlagen zu Ingenieurmassnahmen*, pp. 1–4, Universität Karlsruhe.
- Le Douaran, S., Burrus, J., & Avedik, F., 1984. Deep structure of the north-western Mediterranean Basin: results of a two-ship seismic survey, *Mar. Geol.*, **55**, 325–345.
- Makris, J., Ben-Avraham, Z., Behle, A., Ginzburg, A., Giese, P., Steinmetz, L., Whitmarsh, R., & Eleftheriou, S., 1983. Seismic refraction profiles between Cyprus and Israel and their interpretation, *Geophys. J. R. astron. Soc.*, **75**, 575–591.
- Makris, J., Rihm, R., & Allam, A., 1988. Some geophysical aspects of the evolution and the structure of the crust in Egypt, in *The Pan-African belt of Northeast Africa and adjacent area: tectonic evolution and economic aspects of a late proterozoic orogen*, edited by S. El-Gaby & R. Geriling, pp. 345–369, Braunschweig, Vieweg, Wiesbaden, Germany.
- Morelli, C., 1998. Lithospheric structure and geodynamics of the Italian peninsula derived from geophysical data: a review, *Mem. Soc. Geol. It.*, **52**, 113–122.
- Mooney, W., Prodehl, C., & Pavlenkova, N., 2002. Seismic velocity structure of the continental lithosphere from controlled source data, in *International Handbook of Earthquake and Engineering Seismology, V. 81A*, edited by W. Lee, H. Kanamori, P. Jennings, & C. Kisslinger, pp. 887–910, Academic Press, Amsterdam.
- Nercessian, A., Mauffret, A., Reis, A. D., Vidal, R., Gallart, J., & Diaz, J., 2001. Deep reflection seismic images of the crustal thinning in the eastern Pyrenees and western Gulf of Lion, *J. Geodynamics*, **31**, 211–225.
- Nicolich, R., Laigle, M., Hirn, A., Cernobori, L., & Gallart, J., 2000. Crustal structure of the Ionian margin of Sicily: Etna volcano in the frame of regional evolution, *Tectonophysics*, **329**, 121–139.
- Pascal, G., Mauffret, A., & Patriat, P., 1984. The ocean-continent boundary in the Gulf of Lion from analysis of expanding spread profiles and gravity modelling, *Geophys. J. Int.*, **113**, 701–726.
- Potts, C., Calvert, A., & White, R., 1986. Crustal structure of Atlantic fracture zones - III. The Tydeman fracture zone, *Geophys. J.R. astr. Soc.*, **86**, 909–942.

- Sandoval Castaño, S., 1999. *Estudio de la litosfera en el margen noroeste de la península Ibérica: cuenca interior de Galicia-Macizo Ibérico*, Senior thesis, Universidad Complutense de Madrid, Spain.
- Seber, D., Barazangi, M., Chaimov, T., Al Saad, D., & Khaddour, M., 1993. Upper crustal velocity structure and basement morphology beneath the intracontinental Palmyride fold-thrust belt and north Arabian platform in Syria, *Geophys. J. Int.*, **113**(3), 752–766.
- Waldhauser, F., Kissling, E., Ansorge, J., & Mueller, S., 1998. Three-dimensional interface modelling with two-dimensional seismic data: the Alpine crust-mantle boundary, *Geophys. J. Int.*, **135**, 264–278.
- White, R., 1979. Oceanic upper crustal structure from variable angle seismic reflection-refraction profiles, *Geophys. J.R. astr. Soc.*, **57**, 683–726.
- Whitmarsh, R., Ginzburg, A., & Searle, R., 1982. The structure and origin of the Azores-Biscay Rise, North-east Atlantic Ocean, *Geophys. J.R. astr. Soc.*, **70**, 79–107.
- Whitmarsh, R., Miles, P., & Mauffret, A., 1990. The ocean-continent boundary off the western continental margin of Iberia - I. Crustal structure at 40°30'N, *Geophys. J. Int.*, **103**, 509–531.
- Yuval, Z. & Rotstein, Y., 1987. Deep crustal reflection survey in central Israel, *J. Geodynamics*, **8**, 17–31.





# **Additional resolution tests**

---

We present additional results from resolution tests, mentioned in Chapter 4, but not shown there.

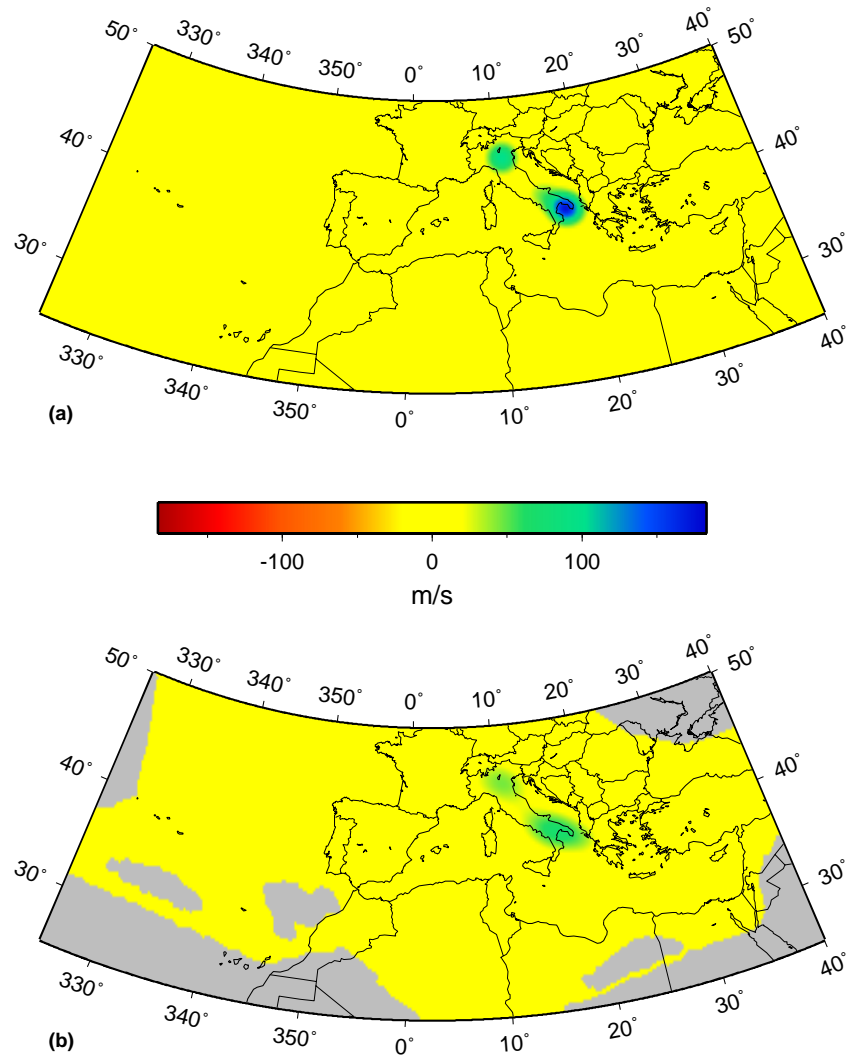


**Figure B.1:** Resolution test showing that vertical tears in the subducted lithosphere beneath the Italian peninsula would be resolved by our dataset - (a) Horizontal slice at 150 km depth through the synthetic input model and (b) through the recovered model.

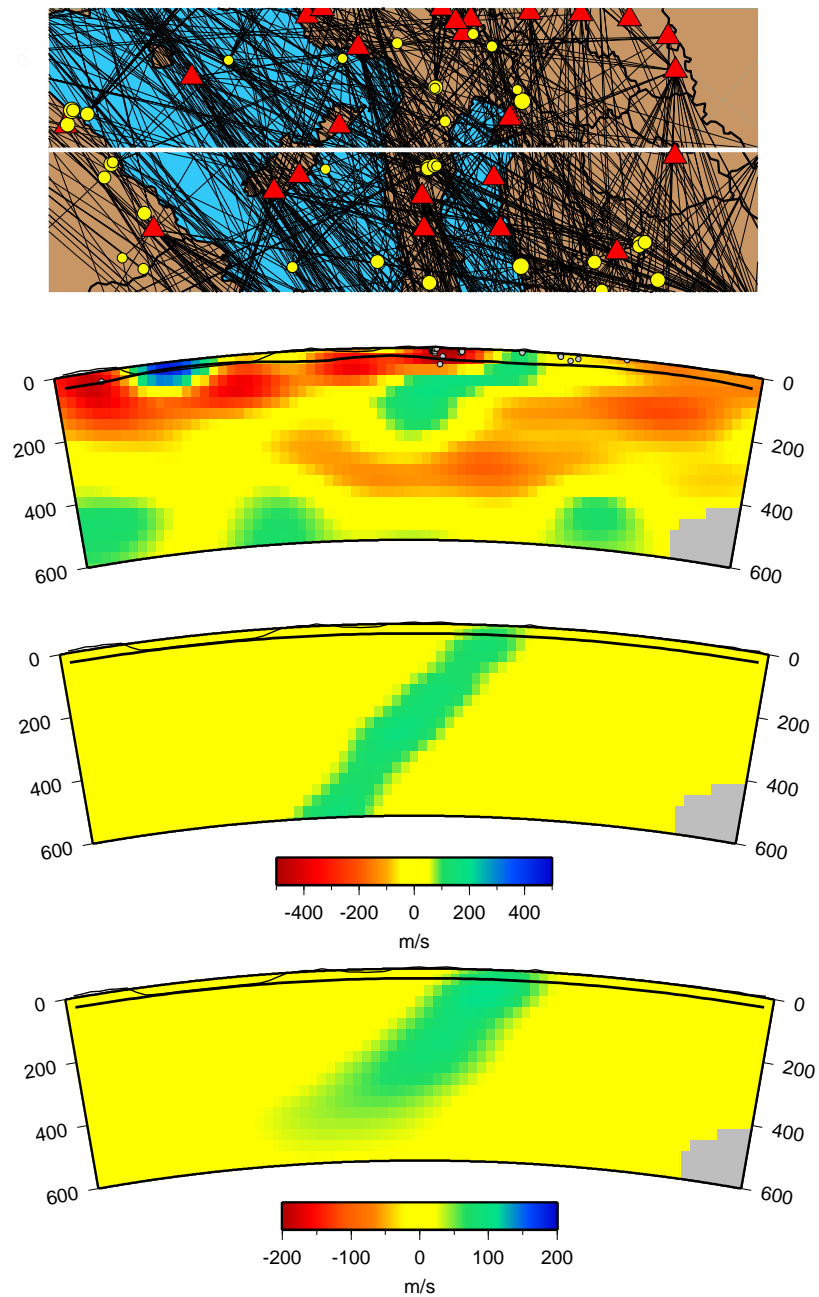


**Figure B.2:** Resolution test showing that a continuous slab under Central Italy would be well recovered down to 500 km. From top to bottom: map illustrating the section location, vertical cross section from northern Algeria to Romania through the obtained S-velocity model (Fig. 4.11), the synthetic input model and the recovered model.

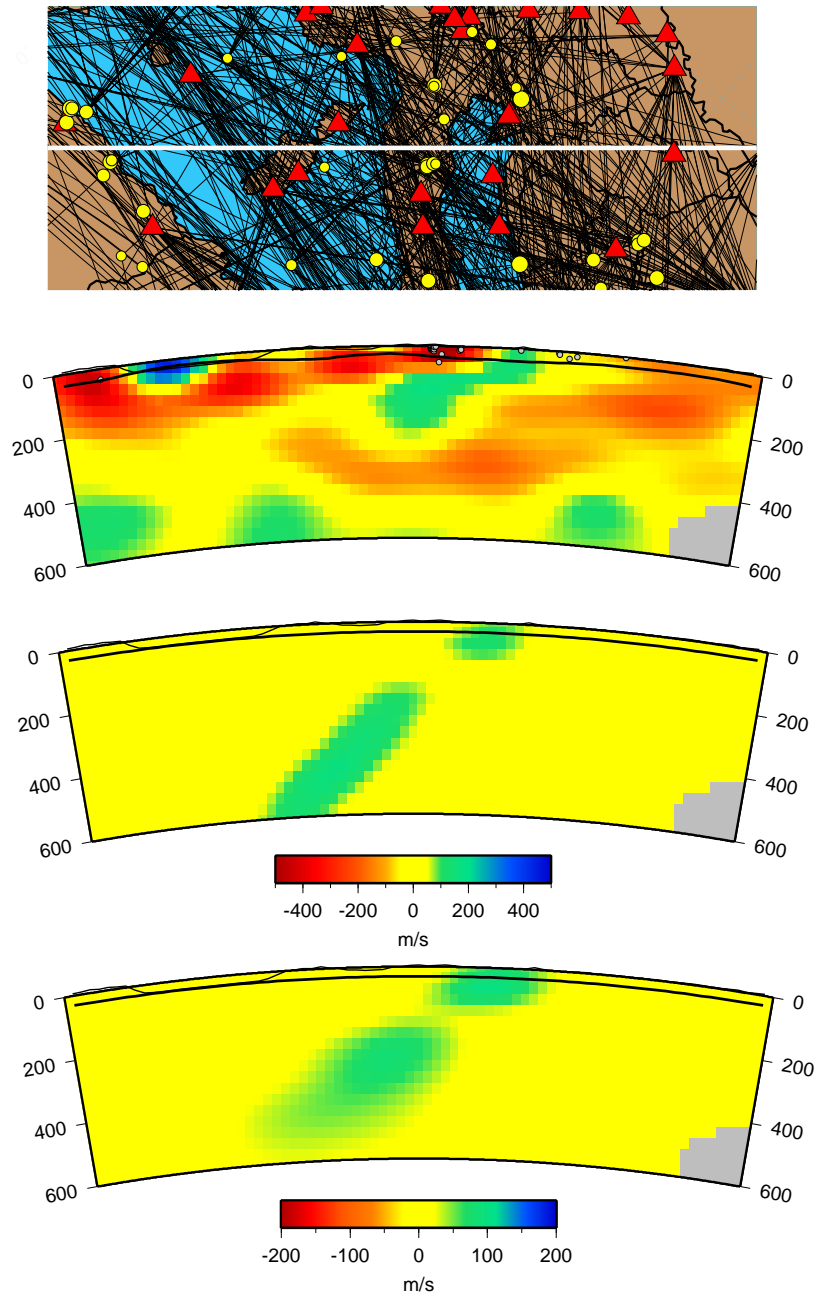


**Figure B.3:** Resolution test showing that a horizontal tear in the slab under Central Italy would be resolved by our dataset. From top to bottom: map illustrating the section location, vertical cross section from northern Algeria to Romania through the obtained S-velocity model (Fig. 4.11), the synthetic input model and the recovered model.

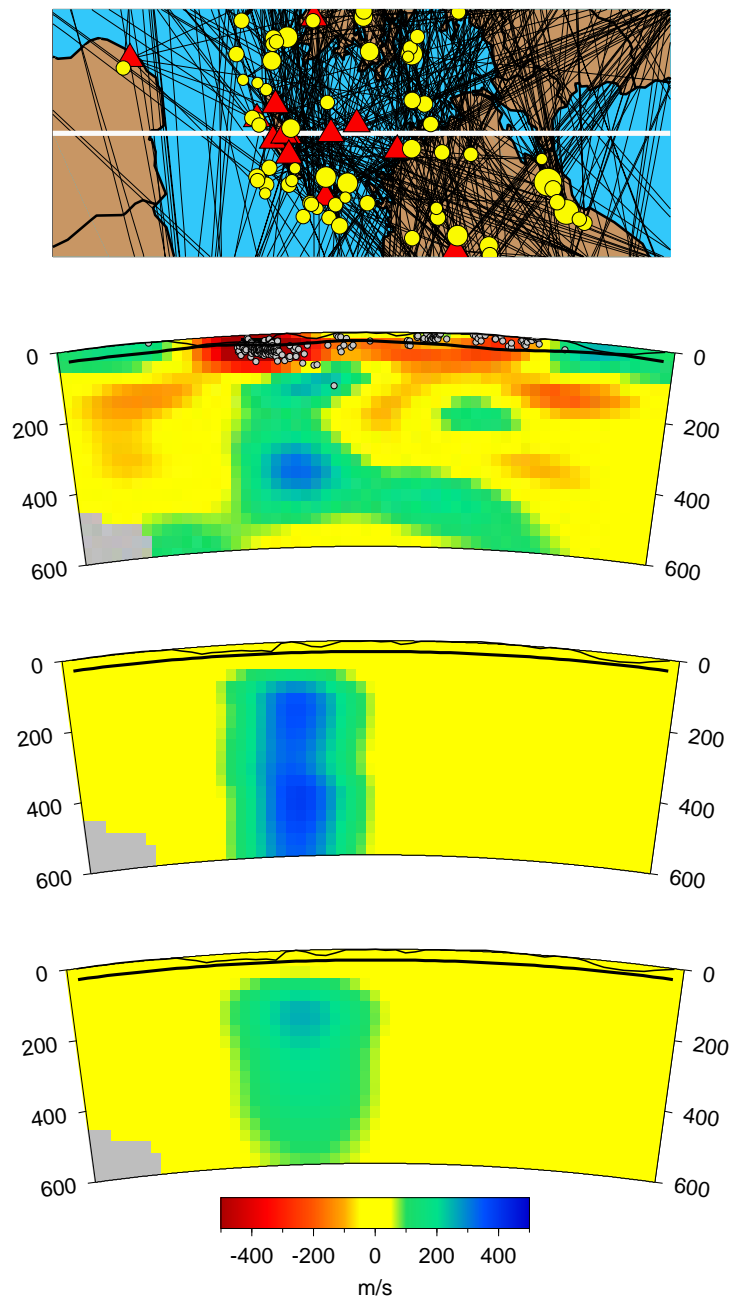


**Figure B.4:** Resolution test showing that the horizontal orientation of the imaged high velocity anomaly in the transition zone beneath Crete is resolved and is not an artefact due to horizontal smearing. From top to bottom: map illustrating the section location, vertical cross section from northern Libya to the Black Sea through the obtained S-velocity model (Fig. 4.11), the synthetic input model and the recovered model.

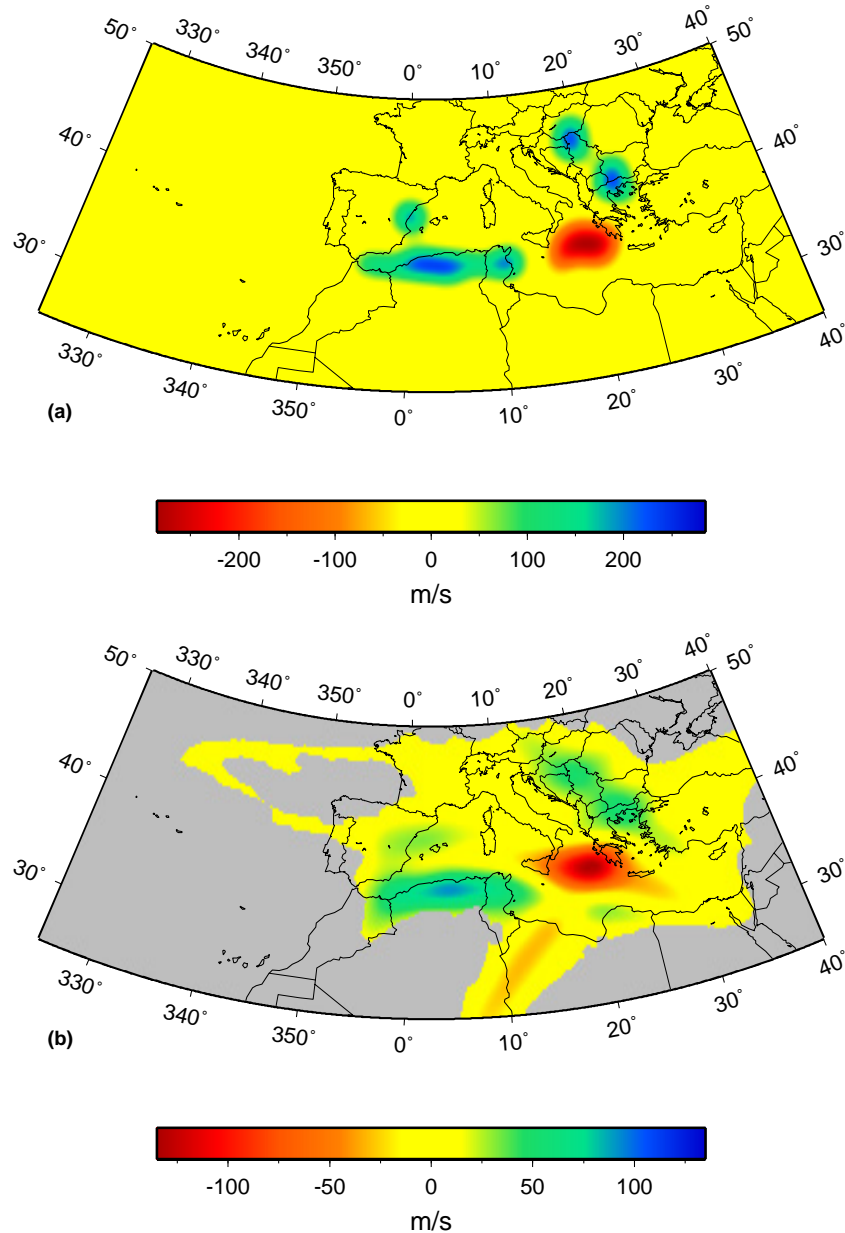


**Figure B.5:** Resolution test showing that the existence of the high velocity anomaly imaged in the transition zone beneath eastern Spain is resolved by our dataset, although its shape is affected by smearing - (a) Horizontal slice at 500 km depth through the synthetic input model, which simulates the structure imaged in the transition zone in the Mediterranean region (Fig. 4.11) and (b) through the recovered model.

# Bibliography

---

- Babuška, V. & Plomerová, J., 1987. Deep structure of the lithosphere beneath the territory of Bulgaria, *Studia geoph. et geod.*, **31**, 266–283.
- Baer, M., 1990. The seismic station network of the Swiss Seismological Service, in *I. Workshop on: MEDNET, the Broad-Band Seismic Network for the Mediterranean*, edited by E. Boschi, D. Giardini, & A. Morelli, pp. 345–350, Istituto Nazionale Geofisica, Roma.
- Banda, E., Dañobeitia, J., Surinach, E., & Ansorge, J., 1981a. Features of crustal structure under the Canary Islands, *Earth planet. Sci. Lett.*, **55**, 11–24.
- Banda, E., Surinach, E., Aparicio, A., Sierra, J., & Ruiz de la Parte, E., 1981b. Crust and upper mantle structure of the central Iberian Meseta (Spain), *Geophys. J. R. Astr. Soc.*, **67**, 779–189.
- Bassin, C., Laske, G., & Masters, G., 2000. The Current Limits of Resolution for Surface Wave Tomography in North America, in *Eos Trans. AGU*, vol. 81, p. F897, Fall Meet. Suppl.
- Ben-Avraham, Z., Ginzburg, A., Makris, J., & Eppelbaum, L., 2002. Crustal structure of the Levant Basin, eastern Mediterranean, *Tectonophysics*, **346**, 23–43.
- Bijwaard, H. & Spakman, W., 2000. Non-linear global *P*-wave tomography by iterated linearized inversion, *Geophys. J. Int.*, **141**, 71–82.
- Blackman, D., Cann, J., Janssen, B., & Smith, D., 1998. Origin of extensional core complexes: Evidence from the Mid-Atlantic Ridge at Atlantis Fracture Zone, *J. Geophys. Res.*, **103**(B9), 21315–21333.

- Blanco, M. & Spakman, W., 1993. The *P*-wave velocity structure of the mantle below the Iberian Peninsula: evidence for subducted lithosphere below southern Spain, *Tectonophysics*, **221**, 13–34.
- Bohnhoff, M., Makris, J., Papanikolaou, D., & Stavrakakis, G., 2001. Crustal investigation of the Hellenic subduction zone using wide aperture seismic data, *Tectonophysics*, **343**, 239–262.
- Boschi, E., Giardini, D., & Morelli, A., 1991. MedNet: the very broad-band seismic network for the Mediterranean, *Il Nuovo Cimento*, **14**, 79–99.
- Boschi, L., 2001. *Applications of Linear Inverse Theory in Modern Global Seismology*, Ph.D. thesis, Harvard University.
- Braunmiller, J., Kradolfer, U., Baer, M., & Giardini, D., 2002. Regional Moment Tensor Determination in the European-Mediterranean Region - Initial Results, *Tectonophysics*, **356**, 5–22.
- Bufo, E., Sanz de Galdeano, C., & Udías, A., 1995. Seismotectonics of the Ibero-Maghrebian region, *Tectonophysics*, **248**, 247–261.
- Burrus, J., 1984. Contribution to a geodynamic synthesis of the Provençal Basin (north-western Mediterranean), *Mar. Geol.*, **55**, 247–269.
- Burrus, J. & Foucher, J., 1986. Contribution to the thermal regime of the Provençal Basin based on FLUMED heat flow surveys and previous investigations, *Tectonophysics*, **128**, 303–334.
- Calcagnile, G. & Panza, G., 1990. Crustal and upper mantle structure of the Mediterranean area derived from surface-wave data, *Phys. Earth Planet. Int.*, **60**, 163–168.
- Calcagnile, G. & Scarpa, R., 1985. Deep structure of the European-Mediterranean area from seismological data, *Tectonophysics*, **118**, 93–111.
- Cammarano, F., Goes, S., Vacher, P., & Giardini, D., 2002. Inferring upper mantle temperatures from seismic velocities, *Phys. Earth Planet. Int.*, submitted.
- Canales, J., Collins, J., Escartín, J., & Detrick, R., 2000. Seismic structure across the rift valley of the Mid-Atlantic Ridge at 23°20' (MARK area): Implications for crustal accretion processes at slow spreading ridges, *J. Geophys. Res.*, **105**(B12), 28411–28425.
- Cermák, V. & Rybach, L., eds., 1979. *Terrestrial Heat Flow in Europe*, Springer, Berlin-Heidelberg.
- Christensen, N., 1966. Elasticity of ultrabasic rocks, *J. Geophys. Res.*, **71**, 5921–5931.



- 
- Dachev, K. & Volvovsky, I., 1985. Deep structure of Bulgaria along the Petrich-Nikopol EMCM-DSS traverse, *Bollettino di Geofisica Teorica ed Applicata*, **27**(108), 263–278.
- Das, T. & Nolet, G., 1995. Crustal thickness estimation using high-frequency Rayleigh-waves, *Geophys. Res. Lett.*, **22**, 539–542.
- De Jonge, M., Wortel, M., & Spakman, W., 1994. Regional scale tectonic evolution and the seismic velocity structure of the lithosphere and upper mantle: The Mediterranean region, *J. Geophys. Res.*, **99**, 12091–12108.
- De Voogd, B., Truffert, C., Chamot-Rooke, N., Huchon, P., Lallemand, S., & Le Pichon, X., 1992. Two-ship deep seismic soundings in the basins of the Eastern Mediterranean Sea (Pasiphae cruise), *Geophys. J. Int.*, **109**, 536–552.
- Dercourt, J., Zonenshain, L., Ricou, L., Kazmin, V., Le Pichon, X., Knipper, A., Grandjacquet, C., Sbertshikov, I., Geyssant, J., Lepvrier, C., Pechersky, D., Boulin, J., Sibuet, J., Savostin, L., Sorokhtin, O., Westphal, M., Bazhenov, M., Lauer, J., & Biju-Duval, B., 1986. Geological evolution of the Tethys Belt from the Atlantic to the Pamirs since the Lias, *Tectonophysics*, **123**, 241–315.
- Dewey, J., Helman, M., Turco, E., Hutton, D., & Knott, S., 1989. Kinematics of the western Mediterranean, in *Alpine tectonics*, edited by M. Coward, D. Dietrich, & R. Park, pp. 265–283, Blackwell Scientific Publications.
- Dick, H., 1989. Abyssal peridotites, very slow spreading ridges and ocean ridge magmatism, in *Magmatism in the Ocean Basins*, edited by A. Saunders & M. Norry, pp. 71–105, Blackwell Scientific Publications.
- Doser, D., Keler, G., Harder, S., Miller, K., & Dial, P., 1997. Development of a lithospheric model and geophysical database for North Africa, Final Report PL-TR-97-2136, Department of energy, Office of non-proliferation and National Security Philips Laboratory, Directorate of Geophysics, University of Texas/El Paso.
- Du, Z., Michelini, A., & Panza, G., 1998. EurID: a regionalized 3-D seismological model of Europe, *Phys. Earth Planet. Inter.*, **105**, 31–62.
- Dziewonski, A. & Anderson, D., 1981. Preliminary reference Earth model, *Phys. Earth Planet. Inter.*, **25**, 297–356.
- Dziewonski, A., Ekström, G., & Salganik, M., 1994. Centroid-moment tensor solutions for January-March 1994, *Phys. Earth Planet. Inter.*, **86**, 253–261.
- Egger, A., 1992. *Lithospheric structure along a transect from the northern Apennines to Tunisia derived from seismic refraction data*, Ph.D. thesis, ETH Zurich, Zurich, Switzerland.

- Engdahl, E., Van der Hilst, R., & Buland, R., 1998. Global teleseismic earthquake relocation with improved traveltimes and procedures for depth determination, *Bull. Seismol. Soc. Am.*, **88**, 722–743.
- Faccenna, C., Funicello, F., Giardini, D., & Lucente, P., 2001. Episodic back-arc extension during restricted mantle convection in the Central Mediterranean, *Earth planet. Sci. Lett.*, **187**, 105–116.
- Fowler, C. & Keen, C., 1979. Oceanic crustal structure - Mid-Atlantic Ridge at 45°N, *Geophys. J.R. astr. Soc.*, **56**, 219–226.
- Früh-Green, G., Connolly, J., Kelley, D., Plas, A., & Grobéty, B., 2001. Serpentinization of oceanic peridotites: Implications for geochemical cycles and biological activity, in *The Subseafloor Biosphere at Mid-Ocean Ridges*, Special Publication, American Geophysical Union, submitted.
- Geiss, E., 1987. A new compilation of crustal thickness data for the Mediterranean area, *Ann. Geophysicae*, **5B**(6), 623–630.
- Ginzburg, A., Whitmarsh, R., Roberts, D., Montadert, L., Camus, A., & Avedik, F., 1985. The deep seismic structure of the northern continental margin of the Bay of Biscay, *Ann. Geophysicae*, **3**(4), 499–510.
- Grand, S., 1994. Mantle shear structure beneath the Americas and surrounding oceans, *J. Geophys. Res.*, **99**, 591–621.
- Guerrot, C., Peucat, J., Capdevila, R., & Dosso, L., 1989. Archean protoliths within Early Proterozoic granulitic crust of the west European Hercynian belt: Possible relics of the west African craton, *Geology*, **17**, 241–244.
- Hanka, W., 1990. The German Regional Broadband Seismic Network (GRN) Project, in *Workshop on MedNet*, edited by E. Boschi, D. Giardini, & A. Morelli, pp. 83–95, Istituto Nazionale di Geofisica, Roma.
- Hanka, W. & Kind, R., 1994. The GEOFON Program, *IRIS Newsletter*, **13**, 1–4.
- Hauser, F., Railenau, V., Fielitz, W., Bala, A., Prodehl, C., Polonic, G., & Schulze, A., 2001. VRANCEA 99 - the crustal structure beneath the southeastern Carpathians and the Moesian Platform from a seismic refraction profile in Romania, in *Starkbeben: vom geowissenschaftlichen Grundlagen zu Ingenieurmassnahmen*, pp. 1–4, Sonderforschungsbereich 461, Universität Karlsruhe.
- Hébert, R., Adamson, A., & Komor, S., 1990. Metamorphic petrology of ODP Leg 109, Hole 670A serpentinized peridotites: serpentinization processes at a slow spreading ridge environment, in *Proceedings of the Ocean Drilling Program, Scientific Results*, edited by R. Detrick, J. Honnorez, W. Bryan, & T. Juteau, pp. 103–115, Vol. 106/109.

- 
- Hirsch, F., Flexer, A., Rosenfeld, A., & Yellin-Dror, A., 1994. Tectonic setting and crustal structure of the Eastern Mediterranean, in *Annual Meeting*, edited by R. Amit, Y. Arkin, & F. Hirsch, p. 40, Israel Geological Society.
- Jacob, A., Shannon, P., Makris, J., Hauser, F., Vogt, U., & O'Reilly, B., 1995. An overview of the results of the RAPIDS seismic project, North Atlantic, in *The Petroleum Geology of Ireland's Offshore Basins*, edited by P. Croker & P. Shannon, pp. 429–431, Geological Society, London.
- Karagianni, E., Panagiotopoulos, D., Panza, G., Suhadolc, P., Papazachos, C., Papazachos, B., Kiratzi, A., Hatzfeld, D., Makropoulos, K., Priestley, K., & Vuan, A., 2002. Rayleigh wave group velocity tomography in the Aegean area, *Tectonophysics*, **358**, 187–209.
- Kennett, B. & Engdahl, E., 1991. Traveltimes for global earthquake location and phase identification, *Geophys. J. Int.*, **105**, 429–465.
- Knipper, A. & Sharaskin, A., 1994. Tectonic evolution of the western part of the Peri-Arabian ophiolite arc, in *Geological Structure of the Northeastern Mediterranean (Cruise 5 of the Research Vessel "Akademik Nikolaj Strakhov")*, edited by V. Krashenninikov & J. Hall, pp. 295–305, Hist. Productions-Hall, Jerusalem, Israel.
- Laske, G. & Masters, G., 1997. A Global Digital Map of Sediment Thickness, in *Eos Trans. AGU*, vol. 78, p. F483, Fall Meet. Suppl.
- Lebedev, S., 2000. *The upper mantle beneath the western Pacific and southeast Asia*, Ph.D. thesis, Princeton University, Princeton, USA.
- Llyod, S., 2003. Effects of observed azimuthal anisotropy on isotropic *S*-velocity models derived from Rayleigh waves, Junior thesis, ETH Zurich, Switzerland.
- Locardi, E. & Nicolich, R., 1988. Geodinamica del Tirreno e dell'Appennino centro-meridionale: la nuova carta della Moho, *Mem. Soc. Geol. Ital.*, **41**, 121–140.
- Lucente, P., Chiarabba, C., Cimini, G., & Giardini, D., 1999. Tomographic constraints on the geodynamic evolution of the Italian region, *J. Geophys. Res.*, **104**(B9), 20307–20327.
- Makris, J., 1985. Geophysics and geodynamic implications for the evolution of the Hellenides, in *Geological evolution of the Mediterranean Basin*, edited by D. Stanley & F. Wezel, pp. 231–248, Springer, Berlin, Germany.
- Makris, J., Ben-Avraham, Z., Behle, A., Ginzburg, A., Giese, P., Steinmetz, L., Whitmarsh, R., & Eleftheriou, S., 1983. Seismic refraction profiles between Cyprus and Israel and their interpretation, *Geophys. J. R. astron. Soc.*, **75**, 575–591.

- Margheriti, L., Lucente, F., & Pondrelli, S., 2003. SKS splitting measurements in the Apenninic-Tyrrhenian domain (Italy) and their relation with lithospheric subduction and mantle convection, *J. Geophys. Res.*, **108**(B4), 2218, doi:10.1029/2002JB0001793.
- Marone, F., Van der Lee, S., & Giardini, D., 2003a. Upper mantle shear-wave velocity structure in the Eurasia-Africa plate boundary region, *J. Geophys. Res.*, submitted.
- Marone, F., Van der Meijde, M., Van der Lee, S., & Giardini, D., 2003b. Joint inversion of local, regional and teleseismic data for crustal thickness in the Eurasia-Africa plate boundary region, *Geophys. J. Int.*, in press.
- Marquering, H. & Snieder, R., 1996. Shear-wave velocity structure beneath Europe, the northeastern Atlantic and western Asia from waveform inversions including surface-wave mode coupling, *Geophys. J. Int.*, **127**, 283–304.
- Martínez, M., Lana, X., Canas, J., Badal, J., & Pujades, L., 2000. Shear-wave velocity tomography of the lithosphere-asthenosphere system beneath the Mediterranean area, *Phys. Earth Planet. Inter.*, **122**, 33–54.
- Meier, T., Dietrich, K., Stöckhert, B., & Harjes, H.-P., 2003. 1-dimensional models of shear-wave velocity for the eastern Mediterranean obtained from the inversion of Rayleigh wave phase velocities and tectonic implications, submitted.
- Meissner, R., Wever, T., & Flüh, E., 1987. The Moho in Europe – Implications for crustal development, *Ann. Geophysicae*, **5B**(4), 357–364.
- Mickus, K. & Jallouli, C., 1999. Crustal structure beneath the Tell and Atlas Mountains (Algeria and Tunisia) through the analysis of gravity data, *Tectonophysics*, **314**, 373–385.
- Miller, D. & Christensen, N., 1995. Velocity behaviour of the lower oceanic crust and upper mantle, in *Eos Trans. AGU*, vol. 76, Fall Meet. Suppl.
- Mocquet, A. & Romanowicz, B., 1990. Three-Dimensional Structure of the Upper Mantle Beneath the Atlantic Ocean Inferred From Long-Period Rayleigh Waves - 2. Inversion, *J. Geophys. Res.*, **95**(B5), 6787–6798.
- Mooney, W., Laske, G., & Masters, T., 1998. CRUST 5.1: a global crustal model at 5° x 5°, *J. Geophys. Res.*, **103**, 727–747.
- Mooney, W., Prodehl, C., & Pavlenkova, N., 2002. Seismic velocity structure of the continental lithosphere from controlled source data, in *International Handbook of Earthquake and Engineering Seismology, V. 81A*, edited by W. Lee, H. Kanamori, P. Jennings, & C. Kisslinger, pp. 887–910, Academic Press, Amsterdam.

- 
- Morelli, C., 1998. Lithospheric structure and geodynamics of the Italian peninsula derived from geophysical data: a review, *Mem. Soc. Geol. It.*, **52**, 113–122.
- National Geophysical Data Center, 1988. ETOPO-5, bathymetry/topography data, Data Announc. 88-MGG-02, Natl. Oceanic and Atmos. Admin., U.S. Dep. of Commer., Washington, D.C.
- Nishimura, C. & Forsyth, D., 1989. The anisotropic structure of the upper mantle in the Pacific, *Geophys. J. R. astr. Soc.*, **96**, 203–229.
- Nolet, G., 1990. Partitioned waveform inversion and 2-dimensional structure under the network of autonomously recording seismographs, *J. Geophys. Res.*, **95**, 8499–8512.
- Nolet, G. & Dahlen, F., 2000. Wave front healing and the evolution of seismic delay times, *J. Geophys. Res.*, **105**(B8), 19043–19054.
- Paige, C. & Saunders, M., 1982. LSQR: An algorithm for sparse linear equations and sparse least squares, *ACM TOMS*, **8**, 195–209.
- Panza, G., Mueller, S., & Calcagnile, G., 1980. The gross features of the lithosphere-asthenosphere system in Europe from seismic surface waves and body waves, *Pure appl. geophys.*, **118**, 1209–1213.
- Papazachos, C. & Nolet, G., 1997. *P* and *S* deep velocity structure of the Hellenic area obtained by robust nonlinear inversion of travel times, *J. Geophys. Res.*, **102**, 8349–8367.
- Pasyanos, M. & Walter, W., 2002. Crust and Upper Mantle Structure of North Africa, Europe, and the Middle East from Inversion of Surface Waves, *Geophys. J. Int.*, **149**(2), 464–482.
- Paulssen, H., 1992. NARS-DEEP: NARS deployed on the East European Platform, *Europrobe News*, **1**, 9.
- Peacock, S., 2001. Are the lower planes of double seismic zones caused by serpentine dehydration in subducting oceanic mantle?, *Geology*, **29**(4), 299–302.
- Peterson, J., 1993. Observation and modeling of seismic background noise, Open-File Rep. 93-322, U.S. Geol. Surv., Albuquerque, New Mexico.
- Pinheiro, L., Whitmarsh, R., & Miles, P., 1992. The ocean-continent boundary off the western continental margin of Iberia - II. Crustal structure in the Tagus Abyssal Plain, *Geophys. J. Int.*, **109**, 106–124.
- Piromallo, C. & Morelli, A., 2003. *P* wave tomography of the mantle under the Alpine-Mediterranean area, *J. Geophys. Res.*, **108**(B2), 2065, doi: 10.1029/2002JB001757.

- Platt, J. & Vissers, R., 1989. Extensional collapse of thickened continental lithosphere: a working hypothesis for the Alboran Sea and Gibraltar Arc, *Geology*, **17**, 540–543.
- Potts, C., Calvert, A., & White, R., 1986. Crustal structure of Atlantic fracture zones - III. The Tydeman fracture zone, *Geophys. J.R. astr. Soc.*, **86**, 909–942.
- Rabinowicz, M. & Briais, A., 2002. Temporal variations of the segmentation of slow to intermediate spreading mid-ocean ridges 2. A three-dimensional model in terms of lithosphere accretion and convection within the partially molten mantle beneath the ridge axis, *J. Geophys. Res.*, **107**(B6), 10.1029/2001JB000343.
- Ritsema, J. & Van Heijst, H., 2000. New seismic model of the upper mantle beneath Africa, *Geology*, **28**(1), 63–66.
- Ritzwoller, M., Shapiro, N., Barmin, M., & Levshin, A., 2002. Global surface wave diffraction tomography, *J. Geophys. Res.*, **107**(B12), 2335, doi: 10.1029/2002JB001777.
- Romanowicz, B., Cara, M., Fels, J.-F., & Rouland, D., 1984. Geoscope; a French initiative in long-period three-component global seismic networks, *Eos Trans. AGU*, **65**(42), 753–754.
- Rommevaux, C., Deplus, C., Patriat, P., & Sempéré, J.-C., 1994. Three-dimensional gravity study of the Mid-Atlantic Ridge: Evolution of the segmentation between 28° and 29°N during the last 10 m.y., *J. Geophys. Res.*, **99**(B2), 3015–3029.
- Sandvol, E., Seber, D., Calvert, A., & Barazangi, M., 1998. Grid search modelling of receiver functions: Implications for crustal structure in the Middle East and North Africa, *J. Geophys. Res.*, **103**(B11), 26899–26917.
- Schmid, C., Van der Lee, S., & Giardini, D., 2003. Teleseismic delay times and shear-wave splitting in the mediterranean region, in *Geophysical Research Abstracts*, vol. 5, p. 10096, European Geophysical Society.
- Seber, D., Barazangi, M., Ibenbrahim, A., & Demnati, A., 1996. Geophysical evidence for lithospheric delamination beneath the Alboran Sea and Rif-Betic mountains, *Nature*, **379**, 785–790.
- Seno, T. & Yamanaka, Y., 1996. Double Seismic Zones, Compressional Deep Trench-Outer Rise Events, and Superplumes, in *Subduction: Top to Bottom*, edited by G. Bebout, D. Scholl, S. Kirby, & J. Platt, Geophysical Monograph 96, American Geophysical Union.

- 
- Shanov, S., Spassov, E., & Georgiev, T., 1992. Evidence for the existence of a paleosubduction zone beneath the Rhodopean massif (Central Balkans), *Tectonophysics*, **206**, 307–314.
- Shapiro, N. & Ritzwoller, M., 2002. Monte-Carlo inversion for a global shear-velocity model of the crust and upper mantle, *Geophys. J. Int.*, **151**, 88–105.
- Shirey, S., Bender, J., & Langmuir, C., 1987. Three-component isotopic heterogeneity near the Oceanographer transform, Mid-Atlantic Ridge, *Nature*, **325**, 217–223.
- Silveira, G. & Stutzmann, E., 2002. Anisotropic tomography of the Atlantic Ocean, *Phys. Earth Planet. Int.*, **132**, 237–248.
- Silveira, G., Van der Lee, S., Stutzmann, E., Matias, L., James, D., Burkett, P., Miranda, M., Mendes Victor, L., Gaspar, J., Senos, L., Solomon, S., Montagner, J.-P., & Giardini, D., 2002. Coordinated seismic experiment in the Azores, *Orfeus Newsletter*, **4**(2), 10.
- Snieder, R., 1988. Large-scale waveform inversions of surface waves for lateral heterogeneity, 2. Application to surface waves in Europe and the Mediterranean, *J. Geophys. Res.*, **93**, 12067–12080.
- Spakman, W., Van der Lee, S., & Van der Hilst, R., 1993. Travel-time tomography of the European-Mediterranean mantle down to 1400 km, *Phys. Earth Planet. Int.*, **79**, 3–74.
- Spetzler, J., Trampert, J., & Snieder, R., 2001. Are we exceeding the limits of the great circle approximation in global surface wave tomography?, *Geophys. Res. Lett.*, **28**(12), 2341–2344.
- Takeuchi, H. & Saito, M., 1972. Seismic surface waves, in *Methods in Computational Physics*, edited by B. Bolt, pp. 217–295, Academic, San Diego, California.
- Tawadros, E., 2001. *Geology of Egypt and Libya*, A.A. Balkema, Brookfield, Rotterdam.
- Thio, H., Song, X., Saikia, C., Helmberger, D., & Woods, B., 1999. Seismic source and structure estimation in the western Mediterranean using a sparse broadband network, *J. Geophys. Res.*, **104**(B1), 845–861.
- Thompson, A., 1992. Water in the Earth's upper mantle, *Nature*, **358**, 295–302.
- Van der Lee, S., 1998. Observations and origin of Rayleigh-wave amplitude anomalies, *Geophys. J. Int.*, **135**, 691–699.
- Van der Lee, S. & Nolet, G., 1997. Upper mantle S-velocity structure of North America, *J. Geophys. Res.*, **102**, 22815–22838.

- Van der Lee, S., Marone, F., Van der Meijde, M., Giardini, D., Deschamps, A., Margheriti, L., Burkett, P., Solomon, S., Alves, P., Chouliaras, M., Eshwehdi, A., Suleiman, A., Gashut, H., Herak, M., Ortiz, R., Davila, J., Ugalde, A., Vila, J., & Yelles, K., 2001. Eurasia-Africa Plate Boundary Region Yields New Seismographic Data, *Eos Trans. AGU*, **82**(51), 637–646.
- Van der Meijde, M., Marone, F., Giardini, D., & Van der Lee, S., 2003a. Seismic evidence for water deep in Earth's upper mantle, *Science*, **300**, 1556–1558.
- Van der Meijde, M., Van der Lee, S., & Giardini, D., 2003b. Crustal structure beneath broad-band seismic stations in the Mediterranean region, *Geophys. J. Int.*, **152**, 729–739.
- Wang, Z. & Dahlen, F., 1995. Validity of surface-wave ray theory on a laterally heterogeneous earth, *Geophys. J. Int.*, **123**(3), 757–773.
- Watts, A. & Torné, M., 1992. Subsidence History, Crustal Structure, and Thermal Evolution of the Valencia Trough: A Young Extensional Basin in the Western Mediterranean, *J. Geophys. Res.*, **97**(B13), 20021–20041.
- White, R., McKenzie, D., & O'Nions, R., 1992. Oceanic Crustal Thickness From Seismic Measurements and Rare Earth Element Inversion, *J. Geophys. Res.*, **97**(B13), 19683–19715.
- Whitmarsh, R., Ginzburg, A., & Searle, R., 1982. The structure and origin of the Azores-Biscay Rise, North-east Atlantic Ocean, *Geophys. J.R. astr. Soc.*, **70**, 79–107.
- Widom, E. & Shirey, S., 1996. Os isotope systematics in the Azores: implications for mantle plume sources, *Earth planet. Sci. Lett.*, **142**, 451–465.
- Woodhouse, J. & Wong, Y., 1986. Amplitude, phase and path anomalies of mantle waves, *Geophys. J. R. astr. Soc.*, **87**(3), 753–773.
- Wortel, M. & Spakman, W., 2000. Subduction and slab detachment in the Mediterranean-Carpathian region, *Science*, **290**, 1910–1917.
- Yegorova, T., Starostenko, V., & Kozlenko, V., 1998. Large-scale 3-D Gravity Analysis of the Inhomogeneities in the European-Mediterranean Upper Mantle, *Pure appl. geophys.*, **151**, 549–561.
- Zeck, H., 1999. Alpine plate kinematics in the western Mediterranean: a westward-directed subduction regime followed by slab roll-back and slab detachment, in *The Mediterranean Basins: Tertiary extension within the Alpine Orogen*, edited by B. Durand, pp. 109–120, Geological Society, London.



Zielhuis, A. & Nolet, G., 1994. Shear-wave velocity variations in the upper mantle beneath central Europe, *Geophys. J. Int.*, **117**, 695–715.



# Curriculum Vitae

---

## Personal

Date of birth	30 April 1975
Place of birth	Bern, Switzerland
Citizen of	Switzerland

## Education

1999-2003	PhD student at the Institute of Geophysics at the Swiss Federal Institute of Technology in Zurich, Switzerland
1994-1999	Study of Earth Sciences with major in Geophysics at the Swiss Federal Institute of Technology in Zurich, Switzerland
1990-1994	High School in Bellinzona, Switzerland